

SOURCE IMAGING IN BRAIN-COMPUTER INTERFACES FOR
COMMUNICATION

SOURCE IMAGING IN BRAIN-COMPUTER INTERFACES FOR
COMMUNICATION

BY
LEILA MOUSAPOUR, B.Sc.

A THESIS
SUBMITTED TO THE DEPARTMENT OF COMPUTATIONAL SCIENCE AND
ENGINEERING
AND THE SCHOOL OF GRADUATE STUDIES
OF MCMASTER UNIVERSITY
IN PARTIAL FULFILMENT OF THE REQUIREMENTS
FOR THE DEGREE OF
MASTER OF SCIENCE

© Copyright by Leila Mousapour, August 2021

All Rights Reserved

Master of Science (2021)
(Computational Science and Engineering)

McMaster University
Hamilton, Ontario, Canada

TITLE: Source Imaging in Brain-Computer Interfaces for Communication

AUTHOR: Leila Mousapour
B.Cs. (Electrical Engineering),
Amirkabir University of Technology, Tehran, Iran

SUPERVISOR: Professor Suzanna Becker and Professor John Connolly

NUMBER OF PAGES: xvii, 145

To every seeker of wisdom and truth

Abstract

Brain-computer interfaces (BCIs) have incredible potential to allow people with limited communication or no ability for speech to be able to communicate. A BCI can acquire brain signals, analyze them, and interpret them into commands or words. A binary set of mental tasks can be mapped into two words, such as Yes and No, to enable a user to answer a binary tree of questions and sufficiently create a communication system. Although motor imagery tasks are the most established control signals used in the context of asynchronous BCI, they are not suitable for a non-negligible percentage of the users. This issue, known as BCI illiteracy, has been shown to improve when individuals are given greater latitude in the choice of mental tasks employed in operating a BCI. However, differentiating the activation pattern of non-conventional mental imageries (MI) is more challenging than motor imagery. Therefore, finding a good feature space in which machine learning and classification methods can be applied to the data is crucial. While the standard in EEG-based BCIs is to directly analyze the electrode space signals, the measurements are greatly contaminated by the volume conduction effect. To address this issue, a novel approach is to map the EEG signals from electrode space into spatial coordinates of the brain to achieve more distinctive features. Hence, this research is intended to

investigate (1) the performance difference of a sensor vs. a source space-based motor-imagery BCI and (2) the effectiveness of source localization using beamforming in non-conventional mental imagery decoding for communication BCI. Firstly, the efficacy of feature extraction in sensor and source space was experimentally compared via using the Linearly Constrained Minimum Variance (LCMV) beamformer and common spatial patterns (CSP) in a two-class motor-imagery paradigm. The analysis suggests that the LCMV beamformer is informing the classifier with meaningful features and state-of-the-art classification accuracies are achieved by the proposed method. Secondly, to make individual optimization of BCI control strategies possible, on a participant by participant basis, the most separable control signals among six MI tasks were identified using spectral and connectivity measures extracted from beamformed sources without prior knowledge on the relevant brain regions/networks. It is demonstrated that beamforming can reveal at least one pair of highly classifiable mental commands specific to the participant which can further be employed in the online setup. Therefore, it is concluded that source space EEG analysis using beamforming, applied to a wide range of mental imagery tasks to select the most separable pair, constitutes a promising framework for further development of BCI systems for communication.

Acknowledgements

I would like to acknowledge the considerable effort my co-supervisors, Dr. Suzanna Becker and Dr. John Connolly, has contributed to this work. They have given freely and patiently of their time and unconditionally supported me through my master's studies. I am grateful for the opportunities you have provided me, your expert guidance, your steadfast support and constant encouragement and your flexibility and understanding.

I had the great fortune of having an exceptional committee, involving Dr. Jim Reilly and Dr. Kiret Dhindsa, who immensely helped me navigate the challenging technical aspects of my project. This project was truly a collaborative effort, and it would not have been possible without the guidance, expertise, resources and most important of all, the motivation you have provided me.

I would like to acknowledge Dr. Saurabh Shaw, who generously dedicated his time to take my questions and make this project achievable despite all the obstacles. I would like to express my sincere gratitude to him as he spent hours walking me through many implementation and coding details. His encouraging words and thoughtful, detailed feedback have been greatly impacted my work.

My greatest supporters throughout this process have been my parents and sister. Mom, Dad, Mina: your constant cheerleading and support gave me the confidence

and resolve to get through the many challenges I encountered along the way. Thank you for your unconditional love and your faith in me.

I also thank my uncle, Mahmoudreza, who had a huge role in my adaptation journey in this new country. I thank my wonderful friends, Mina Wafa, Steve Cygu and Mohammad Chaposhloo for sticking by me during ups and downs of my Master's studies. They have been like a second family to me. A special thanks to Steve, who spent hours discussing machine learning concept with me and greatly helped me improve my skills.

Finally, I would like to acknowledge Dr. Amy Harrison for sharing the EEG-fMRI dataset with me, Chai-Yu Lin, whose apropos suggestions always helped me improve in many ways and lastly, the undergraduate volunteer, Yar Mohammad Aldabagh who helped me with certain segments with my research.

Contents

Abstract	iv
Acknowledgements	vi
Notation, Definitions, and Abbreviations	xvii
1 Introduction	1
2 Background	5
2.1 Brain-Computer Interfacing (BCI)	5
2.2 General Structure of a BCI	10
2.3 BCI for Communication	16
2.4 BCI Challenges	19
2.5 Unmixing Oscillatory Brain Activity by EEG Source Imaging	23
2.6 Source Localization Methods	24
2.7 Source Space BCI	34
3 Methods	41
3.1 Electroencephalography (EEG)	41
3.2 EEG Signal Processing for BCI	43

3.3	Feature Engineering for a Successful BCI	44
3.4	EEG Spectral Feature Extraction	44
3.5	EEG Connectivity Feature Extraction	45
3.6	EEG Spatial Feature Extraction	47
3.7	EEG Source Imaging	50
3.8	Source Features	60
3.9	Machine Learning for BCI	61
4	Motor Imagery-Based BCI in Source Space	71
4.1	Chapter Introduction	71
4.2	Objectives	72
4.3	Dataset	73
4.4	Processing Pipelines	76
4.5	Results	78
4.6	Discussion	84
5	Mental Imagery BCI in Source-Space	88
5.1	Chapter Introduction	88
5.2	Dataset	89
5.3	Processing Pipeline	94
5.4	Results	109
5.5	Discussion	114
5.6	Limitations of the Study	119
6	Discussion, Conclusions and Future Directions	122
6.1	Discussion and Conclusion	122

6.2 Future Directions	125
---------------------------------	-----

List of Figures

2.1	General architecture of a brain-computer interface.	10
2.2	Inverse solution of a simulation containing four source clusters. (A) The ERP at each of the 31 channels containing both signal (central peak) and realistic noise from real recordings. (B) The scalp map at the central ERP peak (vertical red line in A). (C) The dipole moments plotted on the white matter surface of the template brain in lateral view of the left hemisphere. On the left, the ground truth source pattern is depicted with a source cluster in the motor cortex, supplementary motor area, insula and the middle temporal lobe of the left hemisphere. Various inverse solutions that aim to recover this pattern are depicted next to it. Voxels below 25% of the respective maximum are omitted for a clearer representation of the current distribution. (Figure adapted from Hecker et al. [2021])	33
4.1	BCI IV dataset 1 paradigm.	74

4.2	Electrode positions in the layouts are represented as points in 2D Cartesian space together with the outline of the head or other anatomical features, that allows plotting of topographies. The 2D channel layout is not an exact representation of the actual 3D channel positions and is a projection for the purpose of visualization. (a) A standard 10-10 electrode distribution on the head. (b) BCI IV dataset 1 electrode distribution on the head.	75
4.3	Illustration of two of the processing pipelines. (a) PL 2 Classification of motor imagery trials based on Common Spatial Patterns (CSP) of cortical sources. (b) PL 4 : Classification of motor imagery trials based on average power or Neural Activity Index (NAI) of half-Brodmann areas. The LCMV and CSP spatial filters and mRMR feature selection were applied to the training segment of the data and the computed filters were then applied on test data. The same goes for mRMR selected feature indexes.	79
4.4	5-fold cross validation accuracy [%] of binary classification of motor imageries in source and sensor space pipelines for 4 subjects in the BCI IV dataset 1.	80
4.5	BCI IV dataset 1 paradigm.	81
4.6	5-fold cross validation accuracy [%] of binary classification of motor imageries in source and sensor space pipelines for 4 subjects in the BCI IV dataset 1 comparing CSP and source power features.	82

4.7	Distribution of selected features by mRMR algorithm across folds in a 100-fold CV scheme (80% train-20% test split) for pipeline PL 4 where features are the average activity of half-BAs and 50 top features are selected.	83
5.1	Power spectra of subject A, interval 1, mental arithmetic imagery . . .	94
5.2	Illustration of 2 commonly used averaged MRIs to obtain a realistic head model in source localization studies. (a) Colin27 averaged (b) MRI ICBM152 averaged MRI (c) MRI segmentation and gray matter extraction from ICBM152. Since the ICBM152 image is an average MRI across 152 people, it is a smoother image in comparison to Colin27.	96
5.3	Illustration of different steps of head model construction. (a) Three surface meshes obtained from ICBM152 average MRI segmentation. (b) head model geometry; notice that the brain surface is smoothed. (c) 64 Electrode position alignment on the scalp.	99
5.4	Illustration of the head model overlain with the volume grid and source model. The source model consists of the source points inside the brain volume which are specified with red colour.	100
5.5	(a) Lead fields in the XYZ directions for the ICBM152 BEM head model for a superficial source. (b) Magnitude of the lead fields for the ICBM152 BEM head model for a superficial source.	101
5.6	Source activity map obtained by applying a common LCMV beamformer filter for comparing 2 conditions (navigation and subtraction). The source activity patterns for 4 time points during performing mental subtraction imagery for subject D are illustrated.	102

5.7	A parcellation of the cortex superficial grid into 74 Brodmann areas (BA). Each color represents an ROI on the ICBM152 BEM head model. a) Axial view b) Lateral view of the right hemisphere c) Medial view the right hemisphere d) A view from above.	105
5.8	A parcellation of the cortex superficial grid into 26 coarse BAs. Each color represents an ROI on the ICBM152 BEM head model. The grouping of BAs is as follows: 1) BAs 7,39,40 - superior and inferior parietal association areas, 2) BAs 2,3,5 - somatosensory areas, 3) BAs 4,6,8 - motor areas, 4) BAs 20,21,37,38 - inferior temporal areas, 5) BAs 26,27,28,29,30,34 - medial temporal lobe (MTL memory system), 6) BAs 24,25,32,33 - anterior cingulate, 7) BAs 23,31- posterior cingulate, 8) BAs 9,10,44,45,46 - prefrontal area, 9) BAs 17, 18,19 - occipital area, 10) BA 13 - insula, 11) BAs 11,12,47 -orbitofrontal areas, 12) BA 43 - primary gustatory, 13) BAs 22,42,42 - superior temporal gyrus. a) Axial view b) Lateral view of the right hemisphere c) Medial view the right hemisphere d) A view from above.	105

5.9	A parcellation of the brain volume into 16 coarse AAL regions (Chrapka [2018]). Each color represents an ROI on the ICBM152 BEM head model. The gross regions considered are: prefrontal cortex, motor cortex, basal ganglia, insula, parietal cortex, temporal cortex, occipital cortex, limbic regions (Hippocampus, parahippocampal region, Amygdala, Cingulum anterior, medial and posterior), cerebellum as well as an additional medial cerebellum region. a) Axial view b) Lateral view of the right hemisphere c) Medial view the right hemisphere d) A view from above.	106
5.10	Final BCI Pipeline Diagram.	109
5.11	Three best separable pairs of tasks for all participants.	114

List of Tables

4.1	Feature extraction block of all BCI pipelines explored in this chapter.	78
4.2	5-fold cross validation accuracy [%] of binary classification of motor imageries in source and sensor space pipelines for 4 subjects in BCI IV dataset 1.	80
4.3	5-fold cross validation accuracy [%] of binary classification of motor imageries in source and sensor space pipelines for 4 subjects in BCI IV dataset 1 comparing CSP and source power features.	82
5.1	Methods of representative waveform calculation for every ROI compared in this thesis.	107
5.2	Comparison of ROI configuration and regional time-series computation method on subject J, song vs. subtraction.	110
5.3	Pairwise classification of mental imageries for subject A	110
5.4	Pairwise classification of mental imageries for subject B	111
5.5	Pairwise classification of mental imageries for subject C	111
5.6	Pairwise classification of mental imageries for subject D	111
5.7	Pairwise classification of mental imageries for subject E	111
5.8	Pairwise classification of mental imageries for subject F	112
5.9	Pairwise classification of mental imageries for subject G	112

5.10	Pairwise classification of mental imageries for subject H	112
5.11	Pairwise classification of mental imageries for subject I	112
5.12	Pairwise classification of mental imageries for subject J	113
5.13	Pairwise classification of mental imageries for subject K	113
5.14	Pairwise classification of mental imageries for subject L	113
5.15	Pairwise classification of mental imageries for subject M	113

Notation, Definitions, and Abbreviations

Notation

symbol	description
Boldface lower-case	Vector
Boldface upper-case	Matrix
Superscript T	Transpose
Superscript -1	Inverse
$tr()$	Matrix trace

Chapter 1

Introduction

Brain-computer interfaces (BCI) are designed to decode and classify the user's brain activity, usually from scalp-recorded EEG, into a set of mental "actions" to drive an external device. BCIs have immense potential for allowing brain-damaged individuals to gain better control over their environment or even to communicate. Specifically, patients diagnosed with the locked-in syndrome (LIS) who are unable to move or speak while having intact cognition can benefit from BCI-enabled communication solutions ([Vansteensel and Jarosiewicz \[2020\]](#)). However, most of the advancement in this field of speech-less communication has been in the form of invasive BCIs ([Pandarinath et al. \[2017\]](#)). While invasive neuroimaging provides better signal quality owing to direct contact of the electrodes with brain tissue, in most cases, due to reasons such as risk and expense of surgery, invasive techniques are impossible to apply. Consequently, it is of great significance to achieve competitive performance in a non-invasive BCI by investing more on computational techniques and stronger data processing pipelines.

Usable control in the context of BCIs has been defined as having a two-way classification accuracy above 70%. BCI decoding works reasonably well for most healthy

individuals when performing a well-defined, prescribed set of mental actions such as imagining moving the left hand versus the right hand. However, the well-known BCI illiteracy rate is estimated at 15 to 30%, indicating that up to 30% of individuals are never able to achieve a reasonable degree of BCI control ([Vidaurre and Blankertz \[2010\]](#)). The illiteracy rate may be even worse for brain-damaged individuals. A promising solution is to use an open-ended BCI that gives the individual the flexibility to adopt whatever mental commands the BCI is best able to classify ([Dhindsa \[2017\]](#)), even if parts of the brain are impaired. Additionally, it has been suggested in several studies that when participants are presented with an array of mental tasks, it is very likely to detect at least one pair of commands which are highly classifiable and best suited for the user ([Friedrich et al. \[2012\]](#), [Chai et al. \[2012\]](#)).

Classification of non-conventional mental tasks is typically more challenging than motor imagery. One limitation to realizing the full potential of this approach may be related to working in the original signal space at the recorded electrode sites on the scalp surface, making it difficult to classify patterns of activity across a specific network of brain regions. The raw EEG signal suffers from the volume conduction effect, which distorts neurophysiological signals ([Baillet et al. \[2001\]](#)). The term volume conduction refers to the complex effects of measuring electrical potentials at a distance from their source generators which impact the shape of a recorded neuronal potential. Also recorded activity at each site is contaminated by the activity of nearby regions and is a mixture of various sources of activity, resulting in the electrode space signal being a poor indicator of activity in specific brain areas. Here, an alternative is investigated, which is to first project the signal into the brain volume. EEG source imaging (ESI) can counteract the volume conduction effect, and unmix and project

the sensor data into the spatial coordinates of the brain.

EEG source localization aims to reconstruct the current source distribution in the brain from one or more maps of potential differences measured non-invasively from electrodes on the scalp surface (Grech et al. [2008]). Since the 1980s, source localization methods based on advanced signal processing techniques have been proposed to identify the intracerebral generators underlying surface EEG signals. However, due to their high level of sophistication and computational complexity, these advanced techniques have rarely been employed in signal processing pipelines of BCI systems. Thus, this research focuses on assessing the possibility to improve BCI performance utilizing features in source space rather than those in sensor space.

EEG Source localization can potentially provide more informative features to feed into different machine learning algorithms in BCIs as it is expected to increase the signal to noise ratio. Additionally, mapping the activity from 64-channel space to fewer sources reduces data dimensionality immensely, helps avoid overfitting and redundancy, leads to better human interpretations and less computational cost with the simplification of models. Therefore, coming up with sparse features which are able to introduce more separability into the data is of great importance. Moreover, EEG is known for its high temporal resolution while having low spatial precision. Source localization makes use of computational modelling to improve spatial resolution for EEG, overcoming EEG's main limitation.

Due to their superior performance among the wide array of existing ESI methods, The Linearly Constrained Minimum Variance (LCMV) beamformer and standardized low-resolution brain electromagnetic tomography (sLORETA) were applied to reconstruct volume sources (Michel et al. [2004], Grech et al. [2008]). Additionally, to

compare the sensor- and source-based BCIs, common spatial patterns (CSP) as one of the most successful methods in brain activation pattern decoding was utilized ([Saha et al. \[2021\]](#)). Therefore, this research investigated the impact of mapping electrode-space signals to source space as a potential way of improving the performance of a BCI system for communication. The objective of the current project is to explore the following research questions:

1. Does adding the beamforming step before extracting CSP features boost the BCI pipeline performance? In other words, are CSP features extracted from source space more informative than those extracted from sensor space?
2. How do the LCMV beamformer and common spatial patterns compare with each other as two types of spatial filters?
3. Is the LCMV beamformer as a spatial filter more successful in reconstruction of motor imagery activity than sLORETA as a minimum norm-based solution?
4. Is there an optimal pair of tasks for every individual that are very well separable using the LCMV beamformer?

This thesis is organized into 6 Chapters - Chapters 2 present a review of the current literature on Brain Computer Interfaces, BCIs for communication, open challenges in BCI, source localization methods and source space BCIs respectively. Chapter 3 discusses the detailed methods used in chapters 4 and 5. Since two datasets have been analyzed with different pipelines, the results and discussions have be organized in two chapters: chapters 4 and 5. Finally, chapter 6 concludes the thesis by discussing the future possibility of applying the created framework for communication purposes.

Chapter 2

Background

2.1 Brain-Computer Interfacing (BCI)

Brain-computer interfacing is a communication and control technology that aims to provide a reliable translation mechanism of brain signals into comprehensible commands for a machine. The ultimate goal for many BCI researchers is to develop a system that can be used by paralyzed beneficiaries, helping them control wheelchairs or robotic arms. Additionally, applications of this magnificent technology span a broad spectrum, ranging from clinical and rehabilitation to remote controlling of unmanned aerial vehicles, gaming and entertainment applications ([Wolpaw et al. \[2020\]](#)). BCI as an interdisciplinary field of science is a challenging application of signal processing, neuroscience and artificial intelligence (AI).

Similar to any concept or notion in science, *the way* BCI is defined is of great importance. Not only a definition can limit one's imagination of possibilities, more importantly it reflects one's perceptual perspective on the concept. The perceptual perspective of the core ideas subsequently determines the way one would interpret and

tackle the challenges in the field. As an example, if a BCI is merely seen as a neural signal translator, the system might be expected to be fully operational for a certain class of previously-approved inputs for all range of users. In case of malfunction, this solution would be to improve or alter BCI's operating algorithms and the role of the user is insignificant. However, if a BCI system is viewed as an additional instrument serving the user's central nervous system (CNS), just like any other muscle, the user's ability to control the interface would be considered as a factor and the same problem would be viewed as BCI-illiteracy. As a result, possible solutions would be to identify whether a potential user is capable of controlling the interface in the first place and if user training would resolve the issue.

Therefore, as a more precise, yet comprehensive definition, "BCIs quantify CNS activity and translate it into new artificial outputs that *replace, restore, enhance, supplement, or improve* the natural CNS outputs" (Wolpaw et al. [2020]). BCIs thereby modify the interactions between the CNS and the environment. Throughout this thesis, BCIs are discussed and investigated from this standpoint. In the following sections, a brief overview of BCI common categories and applications is provided.

Being extensive in scope, BCIs can be categorized based on various criteria such as dependability, mode of operation, control signal and application (Lotte et al. [2015]). In terms of dependability, the subgroup of BCIs which requires the user to actively control the interface by generating a form of command such as motor imagery-based BCIs are considered to be dependable. On the other hand, independent BCIs such as steady-state visual evoked potential (SSVEP)-based BCIs (explained later) are more suitable for severely impaired individuals. With respect to the mode of operation, BCIs can be recognized as synchronous or asynchronous. In a synchronous BCI the

user and the interface interaction is limited to specific time intervals imposed by a cue. Alternatively, asynchronous BCIs can capture the generated mental command time-independently which makes them more user-friendly but more difficult to implement.

Control signals are signature patterns in a neurophysiological recording that can be decoded and used as commands. There are two major classes of neurophysiological recordings that are used in BCIs and categorize these systems into invasive and non-invasive systems ([Rashid et al. \[2020\]](#)). While Invasive methods such as electrocorticography (ECoG) provide more effective control over the interface due to better signal quality, they require signal acquisition from inside the skull that is not feasible in most cases and applications. Conversely, non-invasive methods available in various modalities including electroencephalography (EEG), magnetoencephalography (MEG), positron emission tomography (PET), functional magnetic resonance imaging (fMRI) and functional near-infrared spectroscopy (fNIRS) can record neural activity from outside the skull avoiding the risks of neurosurgical operations. Each of these modalities allows defining multiple types of control signals which further classify BCI into more specific subtypes.

Due to its ease of use, high temporal resolution and relatively low cost, EEG is the most preferred and prominently used signal in non-invasive BCIs ([Hwang et al. \[2013\]](#)). EEG-based control signals can be either event-related potentials (ERP) such as P300, time-locked visual evoked responses (VEP) and error-related potential (ErrP) or spontaneous activity including slow cortical potential (SCP), sensorimotor rhythms (SMR) and motor/mental imagery (MI). A combination of these can form hybrid control signals.

ERPs are electrophysiological responses to (visual, tactile, auditory, olfactory,

gustatory, etc.) stimuli. In particular VEP signals including steady-state (auditory or visual) evoked potentials (SSAEPs and SSVEPs) are responses to flickering visual stimulation at certain frequencies or amplitude-modulated sound which appear in the EEG signal with the same frequency as the stimuli. Both these responses are very brief in time ($< 500\text{ms}$) which makes them hard to detect from single trials and requires numerous recordings of the repeated response to be recognized. For instance, the P300 response appears almost 300ms after the presentation of a visual stimulus which can be an image or a letter. In an SSVEP-based BCI, the number of visual stimuli indicates the number of commands and each of those is repeating at a certain frequency. While controlling a P300- or SSVEP-based BCI do not require any form of training, operating a SSAEP-based BCI is difficult and requires a high level of auditory attention ([Rashid et al. \[2020\]](#)).

The driving idea behind error-related potential (ErrP) signals is very interesting. As an ERP component, ErrPs arise when the BCI decodes the user's intended signal falsely; thereby these can be exploited to correct for BCI errors in the context of reinforcement learning ([Chavarriaga et al. \[2014\]](#)). ErrPs can be detected from single trials and no longer require averaging over a number of trials which is beneficial in real-time settings. The core idea is that in a closed-loop BCI system the brain can be viewed as the controller ([Abiri et al. \[2019\]](#)). When the controller detects a mismatch between the desired output and resulting output, it generates an ErrP which can be used as a feedback to the intelligent agent to improve the behaviour.

Spontaneous control signals are voluntarily generated by the user in the absence of external stimulation. The most commonly used control signal of this category are sensorimotor rhythms (SMR). It is well established across the literature that

movement or movement intention and preparation give rise to oscillations in the motor cortex referred to as SMR. Since the corresponding cortical regions for right and left hand, tongue and foot movements are sufficiently large and far apart, these signals are detectable and classifiable. Alternatively, non-motor cognitive tasks including mental mathematical computation, mental rotation of figures , visual counting, mental word generation and music imagery are among utilized signals in BCI paradigms ([Rashid et al. \[2020\]](#)).

The essence of a BCI is therefore to detect and decode certain mental conditions; once achieved, it can be used to convert to any operating command for any device. Among popular applications of BCI, cursor control, spelling systems, wheelchair control, mind-wandering, fatigue monitoring and emotion recognition have been explored with varying degrees of success. A novel application of BCI is brain activity-based identification as a biometric system that allows the recognition of an individual based on their brain activity. A study on 15 healthy human participants showed a person’s brain activity remains stable over a long period of time ([Ruiz-Blondet et al. \[2015\]](#)). The same research team proposed an ERP-based BCI which achieved 100% identification accuracy on 50 individuals ([Ruiz-Blondet et al. \[2016\]](#)). Moreover, BCIs have been used to control video games. Using MI control signals acquired by NeuroSky EEG headsets an average accuracy of 70% was obtained in controlling an arcade game among 10 subjects ([Djamal et al. \[2017\]](#)). This thesis focuses on the application of BCI for communication which is elaborated later.

2.2 General Structure of a BCI

A generic BCI system consists of several entities including an acquisition device that collects electrophysiological activity patterns from a human subject, an interfaced computer that performs signal processing for feature extraction and subsequent feature translation, and a computer that generates output in the form of operative device commands for specific BCI applications (Hassanien and Azar [2015]). Figure 2.1 summarizes the six-block architecture of a typical BCI. Each of these blocks is discussed briefly in the following sections, particularly in the case of EEG-based BCIs.

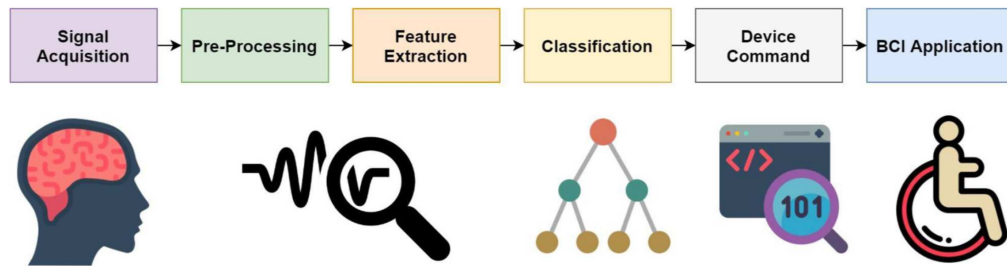


Figure 2.1: General architecture of a brain-computer interface.

The signal acquisition block involves recording of electrophysiological or hemodynamic responses corresponding to the subject’s brain activity. As mentioned in the previous section, the neural signals are recorded using surgical (invasive) or non-surgical (noninvasive) modalities. In this thesis, the EEG signal is the selected neuroimaging modality. EEG measurements are often obtained using a number of electrodes ranging from one to 256 which can be either recorded via wireless or wired EEG signal acquisition. In order to reduce the impedance at the contact point between the electrodes and the scalp, a conductive gel can be used, which is avoided in alternative dry electrode systems. It is worth mentioning that the information transfer rate (ITR) in

such systems is normally 30% lower than that of EEG systems using conductive gel. The acquired brain responses are preamplified to enhance the signal level followed by their conversion to digital format using analog-to-digital converters. Once acquired, the brain signals are amplified, digitized, and transmitted to the interfaced computer for further signal processing.

It should be emphasized that the performance of the BCI depends significantly on the quality of the recorded data. Hence, the experimenter must carefully ensure all the electrodes are recording a clean signal and the participant is following the minimum movement instructions by monitoring the recordings at all time throughout the experiment and adjusting the setup if necessary. Although certain types of noise are inevitable (e.g. eye blinks) and can partly be removed in the preprocessing step, every noise reduction procedure removes a part of the signal as well. Additionally, very noisy channels should be completely removed and replaced by interpolating which leads to a rank deficient signal. This loss of data is expensive in terms of equipment, time and energy and should be avoided as much as possible in the signal acquisition step as no signal processing technique can replace a high-quality, clean signal.

Despite the best effort one can devote in recording a clean EEG signal, unwanted components always contaminate the data which are referred as noise or artifacts. The second step in a BCI system aims to enhance the information content (signal-to-noise ratio (SNR)) by removing the noise in the acquired raw brain data. Good preprocessing contributes to more efficient characterization of input brain patterns in the subsequent steps. External or environmental and physiological sources are the two types of EEG artifacts. AC power lines, lighting and other electrical equipment using the same power source or present in the EEG recording room (e.g. mobile

phones or smart watches) are typical sources of environmental artifacts. Furthermore, any body part movements producing muscle artifacts including electrooculographic activity (EOG), electrocardiographic activity (ECG) and electromyographic activity (EMG) as well as skin resistance are physiological artifacts (Rashid et al. [2020]).

Although a number of these artifacts can be removed, determining the best pre-processing procedure is non-trivial. It is often highly specific to the type of experiment (off-line/online), research question, equipment and the standard procedures available in the laboratory conducting the experiment. Possible preprocessing steps involve baseline removal, high-pass filtering to remove DC-offset or slow drifts, as slow changes in potential are often artifacts, and low-pass filtering, as brain activity oscillates within a certain frequency range. A notch filter can be applied to remove the line noise.

Next, the signals should be re-referenced. This refers to changing the reference after the data acquisition in order to modify the recorded traces and minimize the impact of the reference electrode activity on the original EEG recordings. The new reference is conventionally defined to be the average of the mastoids or average of all scalp channels (common average reference) (Rashid et al. [2020]). A raw data inspection should be performed to reject parts with large muscle artifacts which are spread out in time and/or space. Transient artifacts restricted in time and space (only seen on a few channels) can be neglected. Bad channels should be removed and interpolated. Then, the data is ready for further pre-processing. One of the most widely used pre-processing algorithms is independent components analysis (ICA) which is used to identify and remove muscle-related artifacts. This method essentially decomposes the

multivariate EEG signal into statistically independent components. Thereby eliminating those ICs that have characteristic features of artifacts will allow for a cleaner signal. The potential artifact components can be identified by their waveform and their topography. Any form of re-referencing, especially common averaged reference (CAR) should be performed after these noise removal steps as any residual noise on the reference would be spread out on all electrodes (Cohen [2014]).

The next phase in a BCI signal processing pipeline involves extraction of the most discriminative and non-redundant information bits from the signal. Thus, every segment of the signal (trial) can be described/quantified by a few relevant values termed as “features”. Time-, frequency-, time-frequency, and spatial analysis are the popular types of feature extraction methods in EEG-based BCIs that capture and characterize the major types of variations. Among various time-domain features including the signal’s statistics (such as mean, standard deviation, skewness and kurtosis), energy and log energy entropy (quantifying the amount of randomness and information carried by the signal), autoregressive (AR) coefficients have gained special attention due to their resolution, smooth spectra and applicability to short segments of data. AR models are time-series modeling methods that use observations from previous time steps as input to a regression equation to predict the value at the next time step. However, determining the proper AR modelling order (the number of immediately preceding values in the series that are used to predict the value at the present time) is an open challenge (Rashid et al. [2020]).

Frequency-domain features that have been widely employed across the literature are power spectral density (PSD), band power and spectral centroid. PSD describes

the power present in the signal as a function of frequency and band power is the average power in a specified frequency band. The other measure that can characterize the spectrum of a signal is the spectral centroid which is the median of the spectrum. Periodogram and Welch's methods are commonly used to estimate the signal spectrum in order to obtain these features. Periodogram is simply the squared magnitude of the Fourier transform (FT) of the signal, scaled by a constant. Periodogram is known to be highly variable and to address this issue, Welch's method is usually used. By computing the FT of the overlapping windowed segments of the signal and calculating the average periodogram of all the segments, Welch's method achieves a smoother estimate of the spectrum and is more commonly used in EEG spectrum estimation ([Hu and Zhang \[2019\]](#)). Although temporal and spectral features have shown to be very successful in capturing signature patterns, each neglects some aspects of the signal. Time-frequency analysis, on the other hand, is able to leverage both domains. The most widespread approaches are short-time Fourier transform (STFT), continuous and discrete wavelet transform (CWT/DWT) and wavelet packet decomposition (WPD). The time-frequency maps can be processed as images (e.g. directly fed into neural networks as inputs) or can be used to inspect the data before frequency analysis to focus on interesting time-frequency tiles ([Rashid et al. \[2020\]](#)).

Time, frequency and time-frequency analysis all are based on the principle of temporal filtering in which the output is a weighted summation of surrounding data points such that it highlights features of the data. The fourth category of feature extraction methods is spatial filters which follows a similar concept. Spatial filters are a set of weights applied on all electrodes to isolate spatial features of the data. Common spatial patterns (CSP) and its variants such as common spatio-spectral patterns (CSSP)

and filter back CSP (FBSCP) are extensively utilized methods in EEG-based BCIs with high success which is explained in the method section in detail ([Rashid et al. \[2020\]](#)). Another famous method is surface Laplacian which is a spatial bandpass filter that aims to bypass spatially broad features. Hence, Laplacian-transformed data is an estimation of the potential distribution under the skull (at dura) characterized by improved topographical selectivity ([Cohen \[2014\]](#)). The commonality between all these types of extracted features is their contribution toward the minimization of the intra-class feature variances while maximizing the variances among different class features.

The final step of BCI signal proceeding is decoding the type of cognitive process based on the feature vector characterizing the EEG signal. Since in the context of BCI the array of possible commands typically has countable discrete elements, this is formulated as a classification problem. This stage translates the extracted feature set into operative device control signals. Numerous classification algorithms have been presented in the published EEG-based BCI literature, for instance, the support vector machine (SVM), neural networks (NN), linear discriminant analysis (LDA), Bayesian classifier, k-nearest neighbour (kNN), as well as deep learning and its iterations ([Hwang et al. \[2013\]](#)). Two important points should be considered when selecting a classifier for the BCI. First, the dimensionality of the features set used for estimating the model parameters should be chosen for optimal performance based on the nature of the classifier. Second, the trade-off between bias and variance has to be considered and may involve regularizing the parameter estimation ([Saha et al. \[2019\]](#)). Once the user's intentions are identified through applying the trained classifier on extracted features from a new EEG segment, appropriate control signals

are generated and converted to output device commands.

2.3 BCI for Communication

Locked-in syndrome (LIS) is characterized by a complete or near-complete lack of ability to produce a motor response, including lack of speech, while other aspects of cognition are intact ([Vansteensel and Jarosiewicz \[2020\]](#)). However, it is possible that the person has some remaining motor movement abilities, frequently eye movements. Based on prevalence assessment studies, it is estimated that around 60,000 people around the world are challenged with LIS. Traditional assistive technologies which are employed to restore partial communication and control ability to these patient are known as augmentative and alternative communication (AAC) approaches including three subgroups of no-tech, low-tech and high-tech solutions. No-tech solutions are essentially a protocol between the patient and the caregiver, where the patient's motor responses (e.g. eye blinks) are used to select items on a low-tech AAC (e.g. a letter board); these motor responses are often decoded by an assistive mediator who decides on the direction of the patient's gaze and helps to interpret what they are trying to say. The most advanced AACs also require some residual eye movement to be decodable by eye-tracking devices.

Since AAC solutions essentially depend on some muscle movement, they are not beneficial to LIS patients who have complete loss of motor control. Additionally, due to low autonomy and control difficulty the abandonment rate of these assistive technologies is very high among the users. In such cases where traditional approaches fall short, BCI can theoretically offer a solution. Invasive and non-invasive brain

signals has been exploited for this purpose. In an fMRI study conducted on 16 able-bodied subjects and one minimally-conscious patient, [Monti et al. \[2010\]](#) showed that participants were able to answer Yes/No questions by motor and spatial imagery tasks with high accuracies: 100% and 83% respectively. Hence, not only can fMRI be applied to examine residual awareness and diagnostic purposes, it also can be a communication tool in clinical settings.

In addition to fMRI, other non-invasive brain recording modalities such as fNIRS, MEG and EEG have been explored in the context of communication BCI. A recent study demonstrated the possibility of continuous noisy overt speech recognition from EEG signals ([Krishna et al. \[2019\]](#)). The authors employed an end-to-end automatic speech recognition (ASR) system which directly maps the EEG features to text. Three datasets composed of the recordings from participants while reading or listening to English sentences in presence of noise were analysed. In spite of the fact that such studies have shown the feasibility of *produced* speech recognition from EEG signals, decoding *intended* or *imagined* speech is of interest for BCI communication.

Although in most applications of BCI for communication, conversation-irrelevant mental tasks were utilized, speech-related protocols involving speech imagery of English vowels, syllables, short and long words have been investigated as well ([DaSalla et al. \[2009\]](#), [Brigham and Kumar \[2010\]](#), [Panachakel et al. \[2020\]](#)). For example, one study used EEG signals to directly discriminate between covert speech tasks in 12 healthy individuals who were asked to perform mental repetitions of the words “Yes” and “No” ([Sereshkeh et al. \[2017\]](#)). Unconstrained resting state EEG was also recorded. A multilayer perceptron (MLP) was used to classify all three pairwise combinations of “Yes”, “No” and rest trials based on discrete wavelet transform (DWT)

features. An average accuracy of 75.7% was reached in the classification of covert speech trials versus rest and the classification of “Yes” versus “No” yielded an average accuracy of 63.2%. The above study demonstrates that although classification of imagined words vs. rest can be achieved with a reasonable performance, separation of the words “Yes” and “No” cannot be obtained above the BCI illiteracy rate.

Several open EEG datasets of covert and overt speech are available to interested researchers, such as the Arizona State University (ASU) dataset ([Nguyen et al. \[2017\]](#)). This dataset is comprised of 64-channel EEG recordings of 15 healthy subjects performing 4 types of imagined speech: 1) vowels (/a/, /i/ and /u/), 2) short words (“in” and “out”), 3) long words (“cooperate” and “independent” and 4) a mixture of short and long words (“in” and “cooperate”). The original study published on this dataset used covariance matrix descriptors which lie on a Riemannian manifold as features for a relevance vector machine (RVM). This is the first study to investigate the effect of various conditions including meaning and length of the word in speech imagery-BCI. According to their results, vowels and short words have similar levels of discriminability, suggesting the classification is mostly based on sound rather than meaning. Additionally, classification of long words yielded better results, suggesting that complex words are more easily discriminable from EEG. Finally, the highest classification performance was achieved on short vs. long imagined words.

Similarly, another study applied deep neural networks on DWT features extracted from the ASU dataset, achieving an average accuracy of $71.6 \pm 8.6\%$ in classification of “in” vs. “cooperate” ([Panachakel et al. \[2020\]](#)). A recent comprehensive review has reported advancement in decoding covert speech from EEG ([Panachakel and Ramakrishnan \[2021\]](#)). In conclusion, recent attempts for decoding imagined speech

have proven the feasibility of using EEG as a non-invasive modality in communication BCIs.

2.4 BCI Challenges

In order to identify possible challenges in BCI systems, first an evaluation system must be defined. However, considering the primary targeted users for BCIs are disabled patients, defining such a system is a challenge itself as the majority of research in the field is conducted on healthy populations in controlled conditions. In validating proof of concepts in laboratories as well as real-world settings, performance assessment can be performed through various metrics including success rate, classification accuracy, information transfer rate (ITR), path length, time required, number of operational commands and more ([Rashid et al. \[2020\]](#)). Although the classifier performance reported in accuracy, Kappa value, confusion matrix, sensitivity-specificity pairs etc. seems to determine the performance of the interface, it depends on all previous steps from data acquisition to feature vector calculation as classifier input. Moreover, metrics such as ITR and required time depend on all blocks of the system.

In addition to performance, usability is another important aspect of a BCI which should be assessed based on intuitiveness of the commands, training time, means of the interface (EEG cap etc.) and other quantitative and qualitative criteria. For instance, due to lengthy preparation time, and frequently, the requirement of conductive gel, EEG headsets are often not easy to use. To address this in practical applications, dry EEG headbands with fewer channels have been developed though the signal quality is severely affected resulting in other concerns. Thus, there are a number of crucial issues in every BCI component causing various challenges. The

focus of this study is to ameliorate BCI accuracy through employing source imaging methods and addressing one of the fundamental sources of low accuracy known as BCI illiteracy.

2.4.1 BCI Accuracy

The majority of BCI studies have investigated new approaches in order to build an interface with higher classification accuracy. In fact, the single most important criterion in BCI assessment is the classification accuracy which indicates whether a BCI is useful at all and how accurately it can decode the signal commands; all other criteria come after this factor. Exploration of various brain signal modalities, control signals, signal preprocessing and processing have been explored with the purpose of designing a BCI with the highest accuracy possible.

Despite all the advancements, one of the big open problems in EEG-based BCI is finding a good feature space in which we can apply machine learning and classification methods to the data. As stated in a recent comprehensive review the standard in the field is to start with the electrode space and then extract features such as amplitudes or latencies in the time-domain analyses, power spectral density (PSD) in frequency-domain analysis and common spatial patterns (CSP) in spatial-domain analysis ([Rashid et al. \[2020\]](#)). A much less explored approach is to first map EEG signals from electrode space into spatial coordinates of the brain to achieve more useful features. Electrode space is characterized by a mixture of signals contaminated by volume conduction. Considering various cognitive tasks are characterized by patterns of activity across networks of brain regions, it is plausible that feature extraction from the active regions in the brain volume would improve the BCI performance. Therefore,

this thesis focuses on one of the less explored signal processing approaches for feature extraction: source localization. The details and potential benefits of employing such techniques in BCIs are explained in the following sections.

2.4.2 BCI Illiteracy

Although any interface is ideally expected to work for all users, it is not always possible to obtain a reasonable BCI performance for certain individuals. A non-negligible estimate of 15 to 30% of potential BCI users cannot attain control of a BCI interface (Blankertz et al. [2009]). Substantial effort has been put towards addressing this issue, which is referred to as the BCI illiteracy problem. As a possible approach, the substitution of a subject-optimized classifier using feedback in place of subject-independent classifiers in a BCI has been proposed (Vidaurre and Blankertz [2010]). Other ideas such as instruction alternation, improved signal preprocessing and processing pipelines as well as extensively training the subject and/or the classifier have been proved effective for some subjects. However, some users remain unable to operate any BCI, thus leading to the conclusion of “nonexistence of the universal BCI” (Allison and Neuper [2010]).

Brain structure differences across users are a possible reason for the BCI illiteracy problem. While the human brain, at a coarse level, has a similar structure across people (i.e., the same functional subdivisions), at a finer scale there is tremendous individual variation in localization of functions, which might lead to certain activities not being decodable from EEG or other neuroimaging methods for certain subjects (Allison and Neuper [2010]). These structural differences can be in the form of the key neural populations being located in deeper parts of the brain volume or too close to

other larger and more active groups of neurons in these users which prevent them from generating the brain activity necessary to control a particular BCI. As an example of the structural differences among normal subjects, one can consider the fact that about 10% do not produce a robust P300 response ([Polich \[1986\]](#)). Other plausible reasons underlying BCI illiteracy are producing excessive muscle artifacts by some users or lack of attention in performing the tasks; these challenges are typically surmountable in comparison to individual brain structure variations.

A solution that considers these structural variations across individual brains involves broadening the range of mental commands for controlling a BCI. Rather than asking each user to perform the same pre-specified mental commands, such as imagining moving the left versus the right hand, an alternative approach is to allow the user the flexibility to adopt a range of different mental comments to solve the task ([Dhindsa \[2017\]](#)). Under this approach, not only does the machine adaptively learn to decode the user’s commands, but the user has the freedom to fine-tune their commands so that they are more readily decodable by the machine. Therefore, taking individual differences variations into account and following the ideas proposed by [Dhindsa \[2017\]](#), this thesis investigates a range of mental imagery commands in generating brain signals that are easier to categorize to find the best pairs of commands for an individual.

2.5 Unmixing Oscillatory Brain Activity by EEG Source Imaging

Neuroscience can be abstractly regarded as solving the problem of source separation. Conceptually, a source is a process or an operation of interest that is measured via some equipment. In a complex system such as the brain, multiple sources are active simultaneously which are mixed together in combination with multiple sources of noise contaminating the signal. The majority of the fundamental questions in neuroscience are built upon the idea of source separation in order to study cognitive processes' true constitutive sources or latent constructs which are not directly measurable. There are various approaches to segregate the sources including anatomical, cognitive, temporal (spectral), spatial and statistical source separation.

In anatomical source separation, a certain brain area is focused on based on the anatomy while in cognitive source separation, experiments are designed to isolate a single cognitive process, such as attention, without involving memory, language comprehension or other mental processes. Temporal and spatial approaches are essentially signal decompositions. Statistical source separation uses descriptive statistics to characterize the data, and is based on applying temporal and spatial filters to the data, resulting in every data point in the filtered signal being expressed as a weighted combination of many data points in the original signal (in time or channels domain). EEG brain imaging methods aim to spatially unmix the neural dynamics from regions of interest which is discussed in detail in the following section ([Hansen et al. \[2019\]](#)).

2.6 Source Localization Methods

An EEG recording is a multivariate signal containing information in various dimensions: time, space, frequency, power and phase (Cohen [2014]). Different analysis methods, investigating one or a few of these dimensions simultaneously, capture some but not all of the meaningful variability in the EEG signal. For instance, considering the total amount of information present in the data, time-frequency, spectral and connectivity analysis allow the quantification of much more information compared to what the event-related potential (ERP) method can capture by isolating phase-locked dynamics across numerous trials. While focusing on a subset of the information in the data is advantageous in some applications, such as studying phase-locked responses, having a wider view of the brain processes is preferred in others.

Essentially, most of the conventional EEG analysis methods neglect the information concerning the location of the active sources in the brain (Michel et al. [2004]). Electromagnetic source imaging (ESI) simultaneously details the temporal and spatial dimensions of brain activity which makes it a unique, powerful tool among functional imaging methods that allows one to look inside the human brain (Sekihara and Nagarajan [2008]).

The distribution of source activities can be obtained by solving the so-called inverse problem, which tries to find the one or more sources most likely to have generated the observed pattern of data. However, the problem is ill-posed, because a large number of intracranial source configurations can generate the exact same activity pattern recorded in the EEG. Thus, solving the inverse problem requires introducing a number of a priori assumptions on the generation of the scalp signal and the volume conductor (Michel et al. [2004]) in order to better condition the problem. The

accuracy and reliability of the solution is determined by the appropriateness of these assumptions. As the reality underlying the EEG signal generation is unknown, the researcher must decide whether the assumptions are physiologically reasonable for a given dataset. A wide range of mathematical, statistical, anatomical and functional constraints have been explored to formulate the inverse solution. It cannot be emphasized enough that these assumptions and constraints are pivotal as they determine if the inverse solution is only a possible fit to the data or it actually provides neurophysiological information about the underlying sources. The following sections explain the main categories of source localization methods and their assumptions, preceded by the general formulation of the inverse problem.

Inverse algorithms can be divided into three broad categories: parameter-estimation, imaging and data-driven techniques (Sekihara and Nagarajan [2008]). Parameter estimation approaches presume a few point sources can effectively explain the measurements. Thus, the number of source points is assumed to be known and the location, orientation and strength of these point sources are to be estimated using a linear least-square fit to the data. When Q sources are assumed to exist, a $3Q$ -dimensional nonlinear search is required to obtain the unknown values. Not only is this nonlinear optimization very computationally demanding, but it also has the risk of getting trapped in local minima; thus, it cannot be effectively solved in high-dimensional cases.

The number of sources present in these overdetermined dipolar models can be determined by increasing the number of sources sequentially and investigating the amount of variance every new added source can explain (Scherg et al. [1999]). An alternative approach is to decide the number of current dipoles according to other

functional imaging data including fMRI and PET scans. However, given the fact that the association between hemodynamic and electrophysiological alternations is not yet well understood, this derivation and comparison is risky (Devor et al. [2003]). Furthermore, spatiotemporal decomposition (STD) procedures based on independent and principal component analysis can be used to specify the minimum number of current sources (Koles and Soong [1998]). One of the automatic mathematical approaches that has been developed for this purpose is multiple signal classification (MUSIC), which aims to determine the main signal elements by means of eigenvalue decomposition (Mosher et al. [1992]).

Imaging methods, on the other hand, do not require a priori information on the number of sources and non-linear search in high-dimensional parameter space. Tomographic reconstruction methods and spatial filters are the two major subgroups of imaging techniques (Sekihara and Nagarajan [2008]). Tomographic reconstruction methods are based on amplitude estimation for a grid of fixed sources via least-square fit to the EEG signal, and necessitate voxel discretization over the reconstruction area. As the number of voxels is typically larger than the number of electrodes, the problem is underdetermined and additional constraints are needed to acquire a unique solution to the least-square problem. The minimum norm estimate (MNE) and its variations such as weighted minimum-norm (wMNE) and standardized low resolution brain tomography (sLORETA) are among well-known representatives of this group.

Spatial filters, also known as beamformers in the signal processing domain, are linear operators applied to the surface data in order to estimate the strength of activity of certain locations (the filter's pass band). Being able to discriminate between the signal originating from a point source and all other sources, they can be computed

for all spatial locations in an area of interest to form a 2D or 3D reconstruction of the source distribution. According to the ingredients used to obtain such filters, they can be considered as adaptive or non-adaptive spatial filters. Non-adaptive spatial filters only depend on the geometry of the measurements while adaptive spatial filters also require the measurements covariance matrix (Sekihara and Nagarajan [2008]). It is worth mentioning that most of the topographic reconstruction methods can be reformulated as non-adaptive spatial filters which makes the comparison of methods more convenient. Several common imaging methods are described in the following sections.

The minimum norm estimate solution provides the general primary 3D current distribution by only assuming the activity has the minimum overall intensity, i.e., minimum L2-norm (Hämäläinen and Ilmoniemi [1994]). Although this allows a smooth and unique solution, the lowest intensity restriction is not necessarily physiologically valid. By penalizing solutions with strong activity at a large number of sources, this assumption leads to convergence toward weak, localized activation patterns. Therefore, MNE tends to favour superficially located sources in terms of accuracy (as less activity is required by sources closer to the surface to create the measured scalp voltage) and the current density estimation error increases with depth.

So as to amend the increasing source reconstruction error by depth, weighting strategies were adopted leading to weighted minimum norm estimate (wMNE) procedures. This is achieved by defining a weight matrix W as an a priori constraint. The simplest W is a depth normalization factor: $W = \text{diag}\{\|L\|_2\}$ where L is the gain or leadfield matrix. A weight-normalized minimum-norm filter has been proposed, in which the weights are normalized by the filter norm at each location in

order to ensure a uniform distribution of noise (Dale et al. [2000]). The Focal Underdetermined System Solution (FOCUSS) algorithm employs a recursive weighting procedure providing some focal resolution to a linear estimator of the source distribution (Gorodnitsky et al. [1995]). Although employing these weighting ideas resolves the problem of surface-restricted MNE, it is crucial to realize that the majority of these ideas are entirely mathematical in nature, with no physiological foundation to support the selection of the weights. Additionally, the weight factors can be defined using other source localization methods, as similarly done by Iwaki and Ueno [1998], using a simplified MUSIC prescreening for this purpose. Since conventional wMNE algorithms reconstruct the sources using instantaneous measurements, the sources tend to be distorted if the data are noisy. Using MUSIC to obtain the weights allows integrating more temporal information, and thus, reducing the unwanted distortion.

Laplacian weighted minimum norm solutions including low resolution electromagnetic tomography (LORETA) are among wMNE methods. LORETA minimizes the Laplacian of the weighted sources as a measure of spatial smoothness and selects the smoothest solution. Hence, the solution corresponds to the 3D distribution of neuronal activity that has maximum similarity (i.e., maximum synchronization), in terms of orientation and strength, between neighbouring neuronal populations (represented by adjacent voxels) (Pascual-Marqui et al. [1994]). The physiological basis of this constraint, which assumes a high correlation between neighbouring sources, is basically correct. However, due to the low spatial resolution of EEG, and the distance between source points in the source model, it is argued that this correlation might not be expected and it should be taken with caution. LORETA's assumption of correlation between the activities of large brain areas leads to selection of over-smoothed

and blurred solutions. Several years after the first introduction of LORETA, a review of studies that had successfully used the method and studies that had identified some criticisms was published ([Pascual-Marqui et al. \[2002a\]](#)). The criticisms including the electrophysiological and neuroanatomical constraints being arbitrary and not having physiological meaning and LORETA being incapable of localizing sources on the boundary of the solution space were discussed and clarified.

In contrast to all the linear inverse solutions reported in the mentioned review, which at best can produce images with non-zero localization error, standardized low resolution electromagnetic tomography (sLORETA) yields zero localization error ([Pascual-Marqui et al. \[2002b\]](#)). While sLORETA is a modification of LORETA, it is fundamentally different and does not use the Laplacian operator. The solutions obtained by sLORETA correspond to the standardized values of the estimated current density distribution obtained from MNE. The power of current sources is standardized by their variance which is assumed to be a combination of the source variation and variation due to noisy measurements (assumed to be uncorrelated). This method achieves zero localization error in simulation studies with single sources, and has been shown to provide the lowest error in comparison to MNE and dynamic statistical parametric mapping (dSPM) methods in noisy simulations. In a similar fashion to sLORETA, dSPM standardizes the current sources by their variance; however, the variance of the current density estimate solely depends on the measurement noise, as opposed to sLORETA, which also takes into consideration the actual source variance ([Dale et al. \[2000\]](#)).

In general, spatiotemporal localization accuracy is improved by integrating multiple imaging modalities and incorporating neuroanatomical priors such as cortical

location and orientation restrictions into the MNE solution (Dale and Halgren [2001], Dale and Sereno [1993]). Local autoregressive average (LAURA) (Peralta Menendez et al. [2004]) follows biophysical constraints based upon electromagnetic laws regarding the strength of a source measured at a certain distance. Since the strength of a source decreases with distance from it, this physically derived regularization imposes a spatial structure on the solution which is independent of both the EEG data and the head model. This law is incorporated as the local autoregressive average with coefficients depending upon a power of the distance from every source point. In a visuo-motor ERP task, it was shown the activity maps resulted from LAURA were in concordance with fMRI and other available neurophysiological evidence (Peralta Menendez et al. [2004]).

As mentioned earlier, tomographic reconstruction methods can be formulated as non-adaptive spatial filtering. Thus, the second subset of imaging techniques mostly focuses on adaptive spatial filters including minimum-variance beamformer with various constraints. Depending on the way the weights are chosen, different beamformers can be designed with certain spatial specificity and sensitivity to noise. The goal of beamforming is to estimate the activity originating from one brain site while minimizing the interference of all other simultaneously active sites. The objective can be expressed in terms of optimizing a cost function representing the ratio of activity to noise at a given point. The stop band response of the filter is optimally allocated by minimization of variance to attenuate unwanted activity resulting in minimum-variance beamformers, the best-known spatial filters (Grech et al. [2008]). Additionally, building on the definition of the leadfield matrix (specifying how unit sources project on the scalp), the output of the filter times the leadfield at every location

should be 1, which is the unit-gain constraint.

The unit-gain-constrained minimum variance beamformer suffers from a false intensity increase around the center of the head model. This phenomenon, known as the “leadfield-norm artifact”, is caused by non-uniformity of $\|l(r)\|$ where l is the leadfield vector (3 directions) at location r , with $\|l(r)\|$ being zero at the center (Sekihara and Nagarajan [2008]). Where $\|l(r)\|$ has a spatial dependency, it is more reasonable to constrain the output of the filter for unit sources to $\|l(r)\|$ instead of 1, leading to the minimum-variance beamformer with an array-gain constraint.

Although the adaptive spatial filters described so far are formulated with a single constraint, an adaptive spatial filter can also be formulated with multiple linear constraints. An adaptive spatial filter obtained with such multiple constraints is called a linearly-constrained minimum-variance (LCMV) spatial filter (Van Veen et al. [1997]). Prerequisites for this type of filter are the assumption of uncorrelated source time courses and the signal being low-rank (for the weight vector to exist, it is necessary that the dimension of the noise subspace is greater than one). Despite the fact that most cognitive processes involve activation across multiple different brain regions, leading to correlation between their activity, and thus the idea of brain functional networks, the absence of correlation between sources is an essential assumption of the LCMV method, allowing the formulation of the generalized eigenvalue problem in terms of the observed EEG covariance matrix (Sekihara and Nagarajan [2008]). However, simulations have shown the LCMV beamformer is robust to violation of this assumption and can tolerate partial correlation between the activity of different sources. A comparative study between three types of beamformer, including quiescent beamformer, LCMV beamformer and eigenspace-based beamformer, using

simulated EEG data demonstrated that the eigenspace-based beamformer performs best in extracting the sources and suppressing the noise ([Van Hoey et al. \[1999\]](#)).

The third category of newly-emerged solutions to the inverse problem follows a data-driven approach, in particular, using deep learning methods. Data-driven modelling is based on the analysis of the data characterizing the system under study and focuses on using machine learning and computational intelligence methods to build models that would complement or replace knowledge-driven models([Solomatine and Ostfeld \[2008\]](#)). Artificial neural networks (ANN) have been employed to find the coordination and orientation of one or two dipole source models without any priors ([Awan et al. \[2019\]](#)). A large training dataset is required to successfully train an ANN as well as a long training time to achieve generalizability beyond the training sample. Once trained, the ANN can localize single dipoles with $< 5\%$ error ([Robert et al. \[2002\]](#)).

A novel shallow convolutional neural network (CNN) architecture named ConvDip has been proposed which can be used to estimate the inverse solution for a distributed dipole model ([Hecker et al. \[2021\]](#)). ConvDip is able to operate on single time instances of EEG data and reconstruct the sources in under 40 ms which makes it a good candidate for real-time BCIs. Using 100,000 simulated sample trials with up to 5 source clusters, ConvDip outperforms coherent maximum entropy on the mean (cMEM), eLORETA and LCMV beamformer in almost all cases and it produces fewer ghost sources. An example of this comparison is presented in figure 2.2. Evaluation was performed using mean localization error (MLE) and area under the curve (AUC) metrics to assess the ability to estimate the correct center location and extent of the sources.

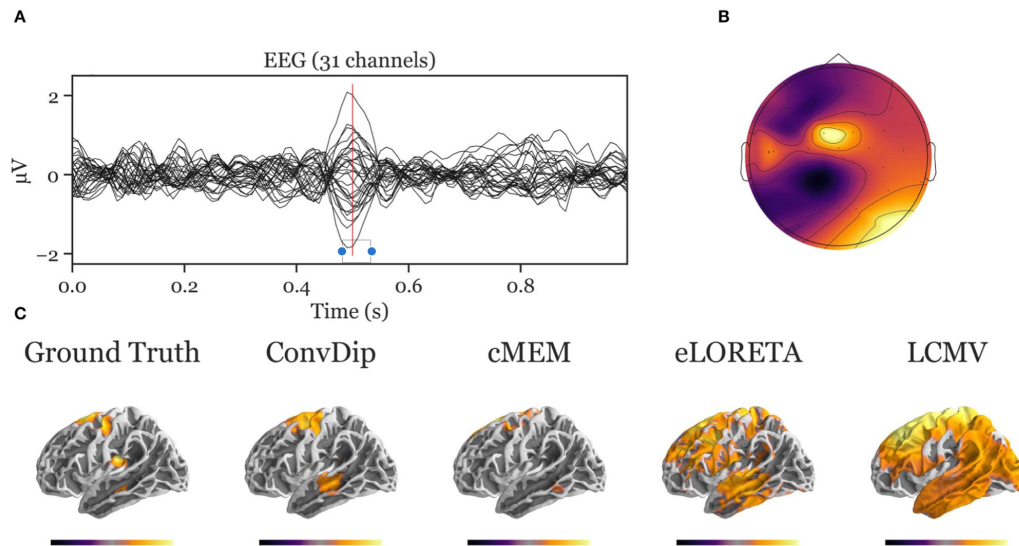


Figure 2.2: Inverse solution of a simulation containing four source clusters. **(A)** The ERP at each of the 31 channels containing both signal (central peak) and realistic noise from real recordings. **(B)** The scalp map at the central ERP peak (vertical red line in A). **(C)** The dipole moments plotted on the white matter surface of the template brain in lateral view of the left hemisphere. On the left, the ground truth source pattern is depicted with a source cluster in the motor cortex, supplementary motor area, insula and the middle temporal lobe of the left hemisphere. Various inverse solutions that aim to recover this pattern are depicted next to it. Voxels below 25% of the respective maximum are omitted for a clearer representation of the current distribution. (Figure adapted from [Hecker et al. \[2021\]](#))

Successful and reliable source localization involves critical analysis considerations and steps which should be attentively selected based on the information of interest to be obtained from the measurements. These critical considerations include the number and positioning of electrodes (including the reference electrode), utilization of MRI for head modelling and determination of relevant time points or periods for source localization; one should judge the validity of the results based on all these factors ([Michel et al. \[2004\]](#)).

2.7 Source Space BCI

As discussed in the previous section, source reconstruction and localization methods mainly aim to invert the effect of volume conduction using physiological knowledge and electromagnetic modelling. Several studies have shown that EEG analysis in source space can potentially manifest a clearer picture of the cortical activity, and thereby facilitate EEG classification. In these studies, the signal is first mapped to the source space and then submitted to frequency, connectivity and other types of analysis. Studies that have taken the source approach differ in their choice of parameters for head modelling as well as the type of inverse solution they apply. A review of these studies, where source localization has been successfully applied to a range of different BCI tasks, is given in the next few paragraphs. It should be noted that additional analysis steps are required to extract useful information from the reconstructed source activity. These include using dimensionality reduction methods, ROI analysis and focusing on certain frequency bands. Thus, this review aims to showcase different processing procedures for employing source analysis techniques and report the effectiveness of source reconstruction methods in mental imagery decoding.

In one study the hypothesis of more accurate motor imagery classification by means of source analysis was tested using a synchronized MI experiment dataset involving 3 subjects (180 trial each) (Qin et al. [2004]). Data were preprocessed using Laplacian spatial filtering in addition to bandpass temporal filtering in the range of [11-12]Hz (this frequency band was selected based on time-frequency analysis). Moreover, using ICA, the data were projected into statistically independent components, and channels on the frontal and occipital areas were omitted due to the interest in

motor areas. Both equivalent dipole model and cortical current density (CCD) imaging approaches were used on only the time point with the largest amplitude from the first ICA components from electrodes placed on the motor cortex (15 time points). The classification was considered correct if the dipole was located on the ipsilateral side with the imaginary hand which was 78.9% and 80.6% for the two methods respectively. Hence, the presented results suggest that the source analysis provides an alternative means of aiding the classification of motor imagery tasks by converting scalp EEG into source signals.

In a subsequent study, using almost the same approach on the same dataset, the results described above were replicated and also improved upon by incorporating some alterations to the algorithm ([Kamoussi et al. \[2007\]](#)). Scalp measurements were preprocessed using surface Laplacian filtering, time-frequency filtering, noise normalization and ICA and then, the CCD method was used to reconstruct 1497 source points distributed across a 2D surface grid of the cortex. For dimensionality reduction purposes, the activity was averaged over 128 cortical locations as regions of interests (ROI), and 84 ROIs with noticeable activity were used. A [8-12] Hz bandpass filter was applied on the ROI time courses again in order to isolate the mu rhythm. Finally, the ROIs' covariance matrix was computed to obtain the signal power at each cortical region (diagonal elements of the covariance matrix). Covariance matrices were classified based on their distance from the averaged covariance of each condition using Von Neumann relative entropy measure and an average classification accuracy of 88% was achieved in three subjects. By comparing this classification rate with the classification rate of the scalp recordings (instead of sources) by the same classifier, an average decrease of 16% was observed. This result suggests the effectiveness of

source analysis and indicates that by compensating the smearing effect of the skull, the performance of motor imagery classification can be substantially enhanced.

A recent study explored a more advanced source localization method for fist and foot MI-based BCIs and compared it with four other SL methods (Li et al. [2019]). By applying overlapping averaging (OA) in the temporal domain and wMNE, this novel method (OA-wMNE) overcomes the shortcomings of ROI-based MNE decoding methods. OA-wMNE preserves the entire effective information of MI in the time domain by overlapping and averaging all trials of the same task, and the ROI selection procedure is replaced by a novel selection of the time of interest (TOI). The SVM classification performance on the dipole features selected using a univariate feature selection (UFS) method was reported. The proposed method was compared against sLORETA, MNE, wMNE, OA-MNE and ICA-wMNE and reached the highest average decoding accuracy of 81.32% across five subjects. Therefore, the proposed method, which integrates OA, has been shown to improve the performance of baseline minimum-norm based solutions and can potentially be useful in future studies.

In addition to classification of coarse imagined movements, EEG source imaging methods have been applied to decode fine intended hand movements as well to expand the control span of real and virtual devices into more dimensions. For example, a system integrating wMNE with ICA was evaluated to decode four MI tasks of the right hand: flexion, extension, supination and pronation (Edelman et al. [2016]). Data were bandpass filtered between 2 and 30Hz and after bad trial rejection through a visual inspection, a surface Laplacian was applied to the data to enhance focal MI-related activity. Using ICA, ROIs were determined by purely data-driven procedures instead of defining certain gyral landmarks. The reported results demonstrate an

improvement of 18.6% for individual task classification over traditional sensor-based methods. Therefore, not only are SL methods useful in classifying coarse intended movements, but also applying the appropriate SL technique has been shown to resolve spatially close sources of activity with high resolution and improve decoding of fine intended movements.

Besides minimum-norm based solutions and the CCD method, beamforming or spatial filtering methods for source reconstruction have been briefly exploited in non-invasive BCIs. For example, a linear spatial filter was designed to effectively surpass the variance of all sources originating from outside the ROI formed on the basis of a priori neurophysiological knowledge ([Grosse-Wentrup et al. \[2009\]](#)). The designed beamformer maximizes the ratio of variance of EEG inside and outside a ROI. This study, which utilized a similar beamforming approach to the MaxSNR beamformer ([Van Veen and Buckley \[1988\]](#)), was the first to employ beamformers in non-invasive BCIs. The spatially filtered EEG trials were converted into feature vectors composed of log-bandpower of 20 frequency bands of 2Hz width covering [1-41] Hz and logistic regression with l_1 regularization was used for classification. Comparing against CSP and Laplacian spatial filtering (LP), this study showed that beamforming outperforms CSP and LP on noisy datasets with few artifactual trials in two-class motor imagery experiments while they perform equally well on datasets with moderate noise contamination.

Moreover, the eigenbased minimum variance beamformer has been utilized in search of better features ([Ahn et al. \[2010\]](#)). Typically, the estimated source activity by minimum-variance beamformers is prone to distortion or noise while performing an eigenspace projection can ameliorate the noise effect. Being incredibly robust to noise

and fast in computation, this type of beamformer is well-suited to BCI applications. After band-pass filtering [10-15] Hz, a beamformer was applied to simultaneously recorded MEG/EEG data in a left and right hand MI paradigm. CSP features were extracted from beamformed signals of the voxels located on motor cortex (area under C3 and C4) distributed at various resolutions and classified with Fisher's linear discriminant analysis (FLDA). Voxel-based CSP was compared to sensor-based CSP and it was reported that in the 37 voxel case, the source space-BCI was significantly more successful than sensor space-BCI across five human subjects. Therefore, by filtering the noise and improving the SNR, the beamformer led to better classification of motor imagery in source space relative to sensor space.

In addition to studying source reconstruction of single and multiple sources of activity, source reconstruction has been used in the study of functional networks of the brain. For example, in a BCI-relevant source-level connectivity analysis of concurrent EEG and MEG recording during voluntary movements, using a DICS beamformer, cortical and sub-cortical networks of coherent sources underlying a finger tapping task were analyzed in 15 participants ([Muthuraman et al. \[2014\]](#)). The network of cortical sources estimated using each of the modalities separately or combined indicated a similar network. However, single sub-cortical sources were only identified for the MEG and the combined approach (MEG+EEG) and the beamformer failed to detect single sub-cortical sources due to the fact that the SNR level in MEG data is significantly higher than that in EEG. Additionally, these same networks of sources underlying voluntary movement have been previously detected from other imaging modalities including fMRI ([Nedelko et al. \[2010\]](#), [Ball et al. \[1999\]](#)). Therefore, EEG source imaging has been shown to be very effective in detection of functional networks,

even more accurately than detection of single sources. These findings indicate that functional networks of the brain and connectivity between regions can be very well quantified by means of ESI methods and can potentially be used as discriminative features between mental states.

Although the bulk of previous studies in EEG source reconstruction are focused on motor imagery (other than SL for ERPs), a recent article reported encouraging results for emotion recognition from reconstructed EEG sources ([Chen et al. \[2020\]](#)). sLORETA was employed for source estimation and 26 Brodmann areas were selected for further analysis. Six types of time- and frequency-domain features, including skewness, kurtosis, power, Hjorth parameters, Fractal dimensions, band differential entropy, Wavelet entropy and functional connectivity in four bands were extracted from significantly active ROIs and frequency bands, and classified using SVM. A comparison of classification performance based on source and sensor space features indicated an average improvement of about 5% when using reconstructed sources. Thus, this study demonstrates the usefulness of SL methods in decoding emotions from EEG data which can potentially be used as mental commands in BCI systems.

The comprehensive literature review provided in this section demonstrated that source localization methods are highly promising in EEG signal analysis, even though they are the least explored category of methods in signal processing pipelines in BCIs. While the majority of previously employed source reconstruction methods have been applied to the problem of decoding motor imagery, other forms of mental imageries that can be used as BCI commands are under-explored. However, as discussed earlier, not everyone is able to attain control of a BCI using these common mental commands which can be due to the differences in their brain structure. It has been shown

that people who have different specialized abilities such as in music, dance/sport or visual arts seem to have correspondingly better ability to use the corresponding type of mental imagery – auditory, motor or visual – (Dhindsa et al. [2015]). This introduces the possibility that exploring a much larger range of different types of imagery can lead to finding individualized mental commands where the user can generate more distinctive brain activity patterns. As complimentary evidence, this study demonstrated taking these individual differences into account can result in better performance of a BCI.

Utilization of a broader range of mental commands in addition to enhancing the signal processing pipeline by integrating state-of-the-art ESI methods leads to an advanced, subject-optimized BCI which can construct a promising solution to the BCI illiteracy problem. The combination of these approaches not only takes into account the individual variations in brain structure, but also benefits from the improved signal quality and projection of the signal into a new space, resulting in potentially better decoding of the mental state. Therefore, this thesis investigates the application of two of the most solid source reconstruction methods, LCMV beamformer and sLORETA in identifying various types of mental commands and conducts a comparison between the *source* approach in contrast to the *surface* approach in classification of EEG signals.

Chapter 3

Methods

3.1 Electroencephalography (EEG)

Electroencephalography (EEG) as a standard method of measuring brain activity is a method of choice for investigating numerous neuroscience research questions and real-time applications such as noninvasive BCIs. EEG signals are recorded with an array of a few up to 256 electrodes fixed on one's head embedded in a headband, an elastic cap or similar. The surface electric potential representing underlying neural activity is thereby measured continuously relative to the potential of a reference electrode placed elsewhere on the head and sampled to generate a signal measured at discrete regular time points. The amplitude of the EEG signal is typically under $75\mu V$ and it can increase to $100\mu V$.

Understanding the neurophysiological basis of EEG is of importance, especially when locating and reconstructing the underlying sources of activity is of interest. It is demonstrated through modelling that the majority of the EEG signal reflects the summation of activity in neurons with their axons aligned in a perpendicular

orientation toward the scalp and which are primarily located in outer cortical layers (Murakami and Okada [2006]). Synchronized polarization and depolarization of apical dendrites of vertically oriented pyramidal cells in layers three, four and five of the cerebral cortex generate the bulk of the voltage sensed on the scalp. As a result of brain tissue having limited conductivity, the electrical fields generated in the extracellular environment have a region of influence of approximately 10 cm^2 (Nunez et al. [2006]). Thus, the recorded signal is not only a mixture of millions of individual neural activities across the brain, but also is spatially blurred.

These measured surface potentials are the result of the spatial averaging of the dendritic field potential resulting in an unintended data reduction process. Although information loss is an inevitable outcome, compared to intracranial recording which has high spatial precision per electrode but only allows very sparse spatial coverage, EEG has the advantage of offering a “big picture” of brain function (Nunez et al. [2006]).

In contrast to the low spatial resolution, the EEG signal’s high temporal resolution allows it to capture the neural dynamics in the time-frame of mental process occurrence. This attribute of EEG makes it an excellent tool for real-time applications in comparison to other neuroimaging methods. Additionally, EEG is a relatively direct (subject to spatial summation and blurring) measure of neural activity which is an advantage over techniques using blood oxygenation level (BOLD) as an indicator of activity in a brain region such as functional magnetic resonance imaging (fMRI). Moreover, the EEG signal is multidimensional, comprising at least four dimensions: time, space, frequency, and power and phase. Voltage changes over time and space, where space is measured through different electrodes, power is the

strength of frequency-band-specific activity and phase is the relative timing of the activity. This multidimensionality provides many possibilities for specifying and testing hypotheses raised from neuroscience and psychology ([Cohen \[2014\]](#)).

3.2 EEG Signal Processing for BCI

Different steps are needed to convert the neural activity recorded as EEG signals to meaningful information that can be translated as commands. BCIs can be operated through utilization of various types of EEG control signals including the P300, error-related potential (ErrP), steady-state evoked potential (SSEVP) and mental imagery (MI) recordings ([Rashid et al. \[2020\]](#)). Processing pipelines vary considerably, as the experimental paradigm and protocols to be followed by the participant depend on the type of control signal. Processing of MI EEG signals, which is of interest in this thesis, is introduced here.

The process begins with collection of raw EEG data, which is typically contaminated with multiple noise sources and suffers a low signal-to-noise ratio (SNR). The signal should be preprocessed to remove artifacts such as eye and muscle movements and filtered to eliminate high and low frequency noise as well as power line noise. The cleaned data is then separated into epochs based on the event markers and becomes ready for data processing. Data processing is commonly comprised of three steps: firstly informative features are computed from the neural activity, secondly the most relevant features are selected and lastly the trials are categorized based on the features extracted from these signals ([Hassanien and Azar \[2015\]](#)), resulting in the final output of the BCI that indicates which class the neural signal belongs to.

3.3 Feature Engineering for a Successful BCI

Different mental processes influence the scalp potentials differently and induce distinct patterns in the brain waves. BCI can be seen as a pattern recognition system that aims at detecting the distinguishable patterns and categorizing these signals ([Hassanien and Azar \[2015\]](#)). These patterns are represented by features which are information computed from the signal to express the data in a new way. A wide array of methods in the time, frequency and spatial domains have been employed by researchers to extract the discriminable aspects of a signal. The classification accuracy and performance of a BCI is greatly dependent on the attributes extracted from the signal. Common spatial patterns, power spectral density, magnitude of coherence and phase lag index have been used to characterize brain signals in this thesis which are introduced in the following section.

3.4 EEG Spectral Feature Extraction

3.4.1 Power Spectral Density

EEG signals are usually characterized by oscillatory patterns at certain frequency bands. Thus, EEG data can be transformed and studied in the frequency domain using spectral analysis. One of the common ways of describing a signal is by quantifying the strength of each of its oscillatory components. The Power Spectral Density (PSD) refers to the distribution of power across the frequency spectrum ([Hu and Zhang \[2019\]](#)), which is a measure of the power content of each oscillatory component

of the signal, and is defined as follows:

$$P_{xx}(\omega) = \lim_{T \rightarrow \infty} f(x) \frac{1}{T} E |\mathcal{F}_x^T(\omega)|^2 \quad (3.4.1)$$

where $E\{\cdot\}$ is the expected value operator and $\mathcal{F}_x^T(\omega)$ is the Fourier transform of the signal x . PSD is remarkably useful in describing the frequency distribution of the EEG signals and is extensively used to study the amount of signal power present in each frequency band. Since various cognitive processes are known to cause modulation in specific frequency bands in EEG signals, PSD values can be used as discriminative features for decoding of different brain states (Hu and Zhang [2019]).

3.5 EEG Connectivity Feature Extraction

Brain connectivity describes the networks of anatomical, functional or effective connections across the brain (Sakkalis [2011]). It is generally believed in neuroscience that when two different brain regions or neural populations are working in coordination, their oscillatory activities can become synchronized and time-locked to each other. This inter-regional synchronization can be interpreted as communication and forms functional connections/networks. Connectivity analysis is performed in order to map out these communication networks in the brain. Specifically, functional connectivity measures, such as coherence and phase lag index, are very useful in characterizing EEG data corresponding to tasks where multiple brain regions work together.

3.5.1 Coherence

Coherence, as a measure of the brain’s functional connectivity, reveals similar neural oscillations or in other words, similarity in frequency content (Sakkalis [2011]). It quantifies frequency correlations of brain activity between two neural signals and mathematically, it is the frequency equivalent of cross-correlation in the time domain. Coherence is computed as follows:

$$C_{xy}(\omega) = \frac{P_{xy}}{\sqrt{P_{xx}P_{yy}}} \quad (3.5.1)$$

where P_{xx} and P_{yy} are the PSD of the two neuronal signals of interest and P_{xy} is the cross-spectral density of the signals (Fourier transform of cross-correlation of signals). The coherence is a complex value where its magnitude represents the amount of variance in one signal that can be explained by the other.

3.5.2 Phase Lag Index

Phase lag index (PLI) is a measure of the asymmetry of the distribution of phase differences between two signals (Stam et al. [2007]). The fundamental idea here is to disregard phase locking that is centered around 0 phase difference as a means of excluding volume conduction effects (at the risk of ignoring true instantaneous interactions). This also applies to phase locking at π and its multiplications. PLI is a volume conduction-robust synchronization measure and is calculated as follows:

$$PLI = |\text{sign}[\Delta\Phi(t_k)]| \quad (3.5.2)$$

where Φ is the instantaneous phase of the signal at time t_k , Δ represents the

difference of phase between the two signals which should be computed in radian and sign is the signum function that discards phase difference of any multiplication of π . The PLI ranges between 0 and 1, with 0 indicating no coupling of instantaneous phase and 1 indicating true, lagged interaction. The Hilbert transform is used to obtain the analytic signal which then is used to extract the instantaneous magnitude and phase information from EEG data.

3.6 EEG Spatial Feature Extraction

Certain mental processes can be best characterized by their alternation across electrodes/space, creating spatial activation patterns on the scalp or in the brain volume, which might not be as recognizable in the time or frequency domains ([Blankertz et al. \[2007b\]](#)). For instance, right and left hand movement result in localized changes in activity for which the most effective decoding approach has shown to be using spatial features ([Ang et al. \[2012\]](#)). The change in the spatial patterns can be further investigated in specific frequency bands or time windows for a more focused analysis ([Sun et al. \[2010\]](#)).

Additionally, simulations have demonstrated that only half of the signal content recorded at each electrode is due to the activity within the $3cm$ radius ([Nunez et al. \[1997\]](#)) and volume conduction blurs the spatial precision of EEG. Spatial filtering methods such as spatial Laplacian or common spatial patterns have proven to mitigate this problem and have a feature-enhancing effect ([Rashid et al. \[2020\]](#)). Source localization techniques can increase the spatial resolution such that complex hand movements including flexion and extension can be decoded from closely-spaced sources on the motor cortex ([Edelman et al. \[2015\]](#)). As explained in the background section,

the focus of this thesis is researching the impact of spatial feature extraction methods on BCI improvement with an emphasis on source localization algorithms which are explained in detail in the following sections.

3.6.1 Common Spatial Patterns

The common spatial patterns method has been widely used in BCIs, especially for distinguishing between motor imagery tasks from EEG signals. This method separates two sets of multivariate signals into their additive subcomponents that have maximum difference in variance and has been very successful in finding spatially localized abnormalities (Koles [1991]). Being a supervised statistical learning approach, CSP forms a spatial filter that maximizes the variance of the signal for one class while minimizing the variance for the other class. This can be mathematically formulated as an optimization problem:

$$W = \max_w \frac{\|WX_1\|^2}{\|WX_2\|^2} \quad (3.6.1)$$

Where X_1 of size $n \times t_1$ and X_2 of size $n \times t_2$ are matrices of all trials of EEG data in class 1 and class 2 recorded with n electrodes. Hence, W which is the spatial filter or the projection matrix is the set of weights that maximizes the variance ratio of the spatially-transformed signals. The solution to the objective function (3.6.1) is acquired by calculating the generalized eigenvector of the ratio of covariance matrices corresponding to the maximal eigenvalue where the normalized spatial covariance

matrix R_l for class l is given as:

$$R_l = \frac{X_l X_l^T}{\text{trace}(X_l X_l^T)}, l = 1, 2 \quad (3.6.2)$$

where X^T is the transpose of the matrix X and $\text{trace}(A)$ is the sum of the diagonal elements. In order to have a meaningful comparison between CSP components, the variance of the signal across all EEG channels of each class of signal should be normalized using a whitening matrix. Eigendecomposition of the composite spatial covariance matrix is used to create the whitening transform:

$$R_c = R_1 + R_2 = V \lambda V^T \quad (3.6.3)$$

where V is the matrix of eigenvectors and λ consists of the eigenvalues. The whitening transform matrix would be:

$$Q = \lambda^{-1/2} V^T \quad (3.6.4)$$

Driving the whitening transform from the composite covariance matrix results in the individual whitened covariance matrices of the two classes to have the same set of eigenvectors V^* :

$$R_l^* = Q R_l Q^T = V^* \lambda_l V^{*T}, l = 1, 2 \quad (3.6.5)$$

The CSP spatial filter is therefore obtained by:

$$W = (V^{*T} Q)^T \quad (3.6.6)$$

The CSP components of an EEG trial X are computed by filtering the signal using the W filter:

$$C = WX \tag{3.6.7}$$

The columns of the matrix W^{-1} are the common spatial patterns. The first and the last columns are the most distinct patterns between the two classes demonstrating the two components which have the highest difference. The CSP features are calculated from the projected EEG signal with W . As the generalized eigenvectors in V^* are sorted according to their eigenvalues λ , the top M and bottom M rows of the projection matrix W would result in the features representing the highest ratio of variance between the two classes. Therefore, the $2M$ most discriminative features between the two classes can be calculated by using the $2M$ components of C in $Z = \{1, \dots, M, n - M + 1, \dots, n\}$:

$$f_j = \log \left[\frac{\text{var}(C_m)}{\sum_{i \in Z} \text{var}(C_i)} \right], j \in \{1, \dots, 2M\}, m \in Z \tag{3.6.8}$$

It is worth mentioning that other feature extraction methods which are applicable to the channel-space signal X are also applicable on the signal in the CSP space C .

3.7 EEG Source Imaging

Although the EEG neuroimaging modality is well known for its high temporal resolution, its lack of sufficient spatial resolution stemming from low signal-to-noise ratio (SNR) and the smearing effect due to the volume conduction has restricted the applications of EEG. As an attempt to address this shortcoming, electrophysiological

source imaging (ESI) techniques have been introduced ([Jatoi and Kamel \[2017\]](#)). Essentially, source imaging methods aim to model brain electrical activity as a series of equivalent current source distributions. The source localization techniques are mainly used for locating abnormal or intense activity from single trial recordings such as epileptic region diagnosis ([Sohrabpour et al. \[2020\]](#)) or ERP signals where the activity of interest is obtained by averaging over more than 100 trials ([Michel and He \[2019\]](#)).

3.7.1 Forward Problem

In order to map the electrode signals into the source space, first a forward model of the system should be obtained by solving a so-called forward problem ([Jatoi and Kamel \[2017\]](#)). The forward model predicts the final electrode potentials recorded at the scalp from known sources in the brain and depends on the geometry of the anatomical model of the head and the electromagnetic properties of different tissues. This is achieved by creating a volume conduction model that approximates the conduction of neural signals through the different tissues of the head. These properties, i.e., the tissue conductivity, are assumed to be uniform and linear thus the surface recording at each site is the superposition of the electric potential of all the active neurons inside the brain. The transfer or gain matrix $\mathbf{H}(\mathbf{q}_i)$ represents the solution to the forward model, which is also known as the lead field matrix,

$$x = \sum_{i=1}^L \mathbf{H}(\mathbf{q}_i) \mathbf{m}(\mathbf{q}_i) + n \quad (3.7.1)$$

where every neuron is modelled as a current dipole with moment $\mathbf{m}(\mathbf{q}_i)$ at location

\mathbf{q}_i . This matrix is a function of head anatomy and how the anatomy is modeled, the source model parameters including the number of sources, their orientation (degrees of freedom per source) and distribution and finally, electrodes and their position.

There are various approaches to numerical head modelling for the forward problem such as the boundary element method (BEM) and finite element method (FEM) (Akalın-Acar and Gençer [2004], Wolters et al. [2007]). The boundary element method (BEM) can be used to generate a realistic head model based on the the subject’s Magnetic Resonance Imaging (MRI) or a generic MRI such as MNI ICBM152, comprised of three separate boundaries: the scalp, outer skull and inner skull. BEM forms a mesh of triangular elements that separate the different components of the head model. These separate compartments have their own conductance values, which are assumed to be constant throughout each region in BEM. Each of these segmentations are also taken to be source current dipoles, which are then used to determine the lead field matrix, predicting the resulting electrode potential based on the contribution of a given source to the scalp potentials.

3.7.2 Inverse Problem

The inverse problem in source imaging methods is the determination of the source activity and locations based on the electrode potentials measured at the scalp which is in fact the problem of interest (Jatoi and Kamel [2017]). This is also deemed an *ill-posed* problem in nature as the number of solutions that could fit the data equally well is infinite, since the number of known values is limited by the number of electrode recordings, which is smaller than the number of unknown parameters. Additionally, the lead field matrix is not a square matrix and as a result, a standard matrix inversion

cannot be used in solving the inverse problem. Therefore, regularization is needed to limit the set of possible solutions and mitigate the above mentioned difficulties. There are many different approaches to solve the inverse problem such as minimum norm estimate (MNE), sLORETA, MUSIC, DICS and LCMV ([Jatoi and Kamel \[2017\]](#)). In this thesis, the application of two of these approaches in BCIs is investigated.

3.7.3 Linearly Constraint Minimum Variance Beamformer (LCMV)

As a general definition, spatial filtering or “beamforming” is a signal processing method utilized in sensor arrays for directional signal transmission or reception ([Van Veen and Buckley \[1988\]](#)). The Linearly Constrained Minimum Variance (LCMV) beamformer is developed based on the principles of spatial filtering, which refers to the discrimination of signals based on their spatial location. The filters are in the form of a weighted sum of signals recorded on the scalp in order to estimate the power of the sources as a function of location ([Van Veen et al. \[1997\]](#)). LCMV spatial filters are designed subject to a linear constraint to minimize the activity of all other sources except for the source at the location of interest. The final output of the method is a map of “neural activity index (NAI)” values, which represent the estimated output power of every source normalized by the estimated noise power of the sources over all locations.

To explain the derivation of the LCMV spatial filters, vectors and matrices are denoted by lower- and upper-case boldface symbols, respectively. Each neural source is modeled as a current dipole. The relationship between source dipoles and the distribution of electric potentials measured on the surface is obtained from (3.7.1),

which was previously introduced as the forward solution.

The electrical activity of a current dipole is described as a random process which can be mathematically modeled with a mean $\bar{\mathbf{m}}_{\mathbf{q}_i} = E\{\mathbf{m}(\mathbf{q}_i)\}$ and covariance matrix $\mathbf{C}(\mathbf{q}_i) = E\{[\mathbf{m}(\mathbf{q}_i) - \bar{\mathbf{m}}_{\mathbf{q}_i}][\mathbf{m}(\mathbf{q}_i) - \bar{\mathbf{m}}_{\mathbf{q}_i}]^T\}$. In this step of the modelling a key assumption is made: It is assumed that the moments associated with different dipoles at different locations are uncorrelated as well as having noise with a mean equal to zero. Considering this assumption, the relationship between the statistics of every current dipole and the statistical features of the electrode signals can be represented as:

$$\bar{\mathbf{m}}_{\mathbf{x}} = E\{x\} = \sum_{i=1}^L \mathbf{H}(\mathbf{q}_i) \bar{\mathbf{m}}(\mathbf{q}_i) \quad (3.7.2)$$

$$\mathbf{C}(\mathbf{x}) = E\{[\mathbf{x} - \bar{\mathbf{m}}_{\mathbf{x}}][\mathbf{x} - \bar{\mathbf{m}}_{\mathbf{x}}]^T\} = \sum_{i=1}^L \mathbf{H}(\mathbf{q}_i) \mathbf{C}(\mathbf{q}_i) \mathbf{H}(\mathbf{q}_i)^T + \mathbf{Q}_n, \quad (3.7.3)$$

where \mathbf{Q}_n is the covariance matrix of the noise. Designing the LCMV filter, the spatial samples are the elements of EEG data (i.e, the signal at each channel location) and the spatial pass band of each filter is essentially the location of interest i.e. the source. The goal is to design a set of beamformers or spatial filters where each passes the signals originating from a specified location, while attenuating activities of other locations. Also, as the signal at each source location has three dipole moment components, three separate beamformers are constructed for each location. Thus, if a spatial filter centred at location \mathbf{q}_0 is denoted by an $N \times 3$ matrix $\mathbf{W}(\mathbf{q}_0)$, the three

component filter output \mathbf{y} is the inner product of $\mathbf{W}(\mathbf{q}_0)$ and \mathbf{x} :

$$\mathbf{y} = \mathbf{W}(\mathbf{q}_0)\mathbf{x}. \quad (3.7.4)$$

Thus, an ideal narrowband spatial filter should satisfy the following, which is to pass the activity of interest and to suppress the activity of other locations:

$$\mathbf{W}^T(\mathbf{q}_0)\mathbf{H}(\mathbf{q}) = \begin{cases} \mathbf{I} & \mathbf{q} = \mathbf{q}_0 \\ \mathbf{0} & \mathbf{q} \neq \mathbf{q}_0. \end{cases} \quad (3.7.5)$$

If the unit response in the pass band (linear response constraint) and zero response in the stop band holds, the output of the filter would be exactly the dipole moment $\mathbf{m}(\mathbf{q}_0)$ at each location in the brain in the absence of noise. However, it is practically impossible to have full attenuation in the stop band of a filter, temporal or spatial. The LCMV approach offers a solution for this problem: designing an optimal filter. The core idea is that instead of aiming for zero response in the stop band, the LCMV finds the filter that minimizes the variance at the filter output while still passing the full signal in the pass band (linear response constraint). This strategy forces the stop band response at any location $\mathbf{m}(\mathbf{q}_s)$ other than $\mathbf{m}(\mathbf{q}_0)$ to be as small as possible.

The LCMV problem can be formulated as:

$$\min_{\mathbf{W}(\mathbf{q}_0)} tr(\mathbf{C}(\mathbf{y})) \text{ subject to } \mathbf{W}^T(\mathbf{q}_0)\mathbf{H}(\mathbf{q}) = \mathbf{I}. \quad (3.7.6)$$

Solving (3.7.6) by using the method of Lagrange multipliers yields the solution to

the LCMV filter:

$$\mathbf{W}(\mathbf{q}_0) = [\mathbf{H}^T(\mathbf{q}_0)\mathbf{C}^{-1}(\mathbf{x})\mathbf{H}(\mathbf{q}_0)]^{-1}\mathbf{H}^T(\mathbf{q}_0)\mathbf{C}^{-1}(\mathbf{x}). \quad (3.7.7)$$

Thus, the beamformer for each location can be obtained by the transfer function (lead field) and the covariance of the sensor level data. Using (3.7.7) in (3.7.4) provides an estimate of the dipole moment at location \mathbf{q}_0 . As mentioned before, the variance of a dipole moment can indicate its strength of activity. The estimated variance of the filter output is the value of the cost function in (3.7.7) at the minimum, which after several algebraic steps is:

$$\widehat{\text{Var}}(\mathbf{q}_0) = [\mathbf{H}^T(\mathbf{q}_0)\mathbf{C}^{-1}(\mathbf{x})\mathbf{H}(\mathbf{q}_0)]^{-1}. \quad (3.7.8)$$

By evaluating (3.7.8), which is the estimate of the activity at each location, the source reconstruction is performed. This can be interpreted by considering a group of dipoles with high variance as a highly active *region* and vice versa. Thus, (3.7.8) is referred to as the estimated “spatial spectrum” of the neural activity.

The detail resolution of the activity’s spatial spectrum is limited by the filter’s pass bandwidth which is basically the resolution of the source grid (the minimum distance between two adjacent dipoles) encoded in the transfer matrix $\mathbf{H}(\mathbf{q})$. This resolution also depends on the number of electrodes, their distribution as well as the signal-to-noise ratio (SNR) associated with the feature of interest which is the source (not the EEG data). It is important to note that SNR in this covariance-based analysis has a different definition compared to the conventional amplitude of the signal to amplitude of the noise ratio. SNR in this context is defined as the ratio of the variance of the

source and variance of the noise. Thus, the more the variance of the source is in proportion to the variance of the noise, the more accurate the activity is going to be estimated. Thus, higher SNR leads to higher resolution. This is a direct outcome of the variance minimization step which determines the spatial filters.

In practice, the SNR of the scalp recorded data is generally small and therefore the noise is a significant component of the estimated neural activity acquired from (3.7.8). The spatial distribution of the noise specifically plays an important role. If the noise is not uniformly distributed in the spatial spectrum or if it is concentrated at a location, it will interfere with localization of the actual neural sources. It can be shown that the noise spatial spectrum relies on the lead field matrix $\mathbf{H}(\mathbf{q})$ by assuming the $\mathbf{C}(\mathbf{x})$ is completely due to uncorrelated noise. It also depends on the covariance matrix of the noise \mathbf{Q} . By substitution of (3.7.3) into (3.7.8), it can be shown that the $\widehat{\mathbf{Var}}(\mathbf{q}_0)$ always has an additive noise component in this form:

$$\mathbf{tr}\{[\mathbf{H}^T(\mathbf{q}_0)\mathbf{Q}^{-1}\mathbf{H}(\mathbf{q}_0)]^{-1}\}. \quad (3.7.9)$$

Thus, (3.7.9) is the noise spatial spectrum. As experimental data usually have a low SNR, this noise component of the source activity can interfere and cover the spatial spectrum of actual active sources. The LCMV beamformer resolves this problem by normalizing the estimated spatial spectrum of the data by the estimated noise spatial spectrum, to obtain the “neural activity index (NAI)”:

$$\widehat{\mathbf{Var}}_N(\mathbf{q}_0) = \frac{\mathbf{tr}\{[\mathbf{H}^T(\mathbf{q}_0)\mathbf{C}^{-1}(\mathbf{x})\mathbf{H}(\mathbf{q}_0)]^{-1}\}}{\mathbf{tr}\{[\mathbf{H}^T(\mathbf{q}_0)\mathbf{Q}^{-1}\mathbf{H}(\mathbf{q}_0)]^{-1}\}}. \quad (3.7.10)$$

In other words, the NAI is an estimate of the source to noise variance as a function

of location. In order to obtain the NAI, the noise covariance matrix \mathbf{Q} is required which can be estimated from a source-free data, such as pre-stimulus data, also known as baseline activity. Alternatively, if the noise is assumed to be uncorrelated between channels, then $\mathbf{Q} = \mathbf{I}$.

It is worth recalling that \mathbf{x} is the vector of electric potentials recorded at all the electrode sites at one instant in time. Therefore, the NAI can be estimated at all time points of the data to finally obtain the estimated activity of the sources in time, which is referred to as source time courses or source time series.

3.7.4 Standardized Low-Resolution Brain Electromagnetic Tomography (sLORETA)

The second source localization method employed in this thesis, standardized Low-Resolution Brain Electromagnetic Tomography (sLORETA), estimates source locations based on standardized values of the current density estimates ([Pascual-Marqui et al. \[2002b\]](#)). The equation that relates the scalp electrode potentials to the current density is:

$$\Phi = \mathbf{KJ} + c\mathbf{1}. \quad (3.7.11)$$

Note that for all equations, terms that are bolded represent matrices and those not bolded are scalar values. Φ represents the electrode potentials, \mathbf{J} is the current density matrix and \mathbf{K} is the lead field matrix that relates the two values ([Pascual-Marqui et al. \[2002b\]](#)). As mentioned earlier, the lead field matrix is determined based on the solution of the forward problem and takes into consideration the conductivity as well as the distance between the source and a given electrode ([Mosher et al. \[1999\]](#)).

Each entry of the lead field matrix computes the resulting electrode potential due to a unit strength dipole at a given voxel, hence, the matrix has dimensions $N_E \times 3N_V$ where N_E represents the number of electrodes and N_V represents the number of voxels or current dipoles in the the x, y, z orientations . Thus, the inverse problem aims to find the value of the \mathbf{J} matrix based on known electrode potentials and the lead field matrix determined by the solution of the forward problem. The equation below indicates the minimization problem that is solved to find the value of \mathbf{J} , the current densities:

$$F = \|\Phi - \mathbf{KJ} + c\mathbf{1}\|^2 + \alpha\|\mathbf{J}\|^2 \quad (3.7.12)$$

The purpose of solving the above equation is to determine the value of \mathbf{J} such that the term $\|\Phi - \mathbf{KJ} + c\mathbf{1}\|^2 = 0$ with a given Φ , \mathbf{K} and α value. α is a regularization parameter that limits the bounds of the minimization solution in order to prevent overfitting (Jatoi, 2019). The solution, \mathbf{J} , can be represented as the projection matrix:

$$\hat{\mathbf{J}} = \mathbf{T}\Phi \quad (3.7.13)$$

where Φ is equal to the electrode potentials and \mathbf{T} is a matrix that signifies the relation between the electrode potentials and current sources calculated by:

$$\mathbf{T} = \mathbf{K}^T\mathbf{H}[\mathbf{H}\mathbf{K}\mathbf{K}^T\mathbf{H} + \alpha\mathbf{H}] \quad (3.7.14)$$

and \mathbf{H} is the average reference operator.

sLORETA determines the activity sources based on the standardization of the current density values, for which their variances are required. sLORETA calculates each of these variances by incorporating the electric potential variance from the EEG,

which is composed of both the variance of the actual sources as well as the variance of the noise. To standardize the current density estimates, the matrix \mathbf{J}_l^T at the l th voxel, is multiplied by the inverse of the estimated current source variations at the l th voxel. Then to regain the amplitude of the sources and yield the standardized current density power, the product is multiplied yet again by the estimated current density at the l th voxel $\hat{\mathbf{J}}_t$. This relation is presented by Pascual-Marqui (2002) in the following equation:

$$\hat{\mathbf{J}}_t \{[\mathbf{S}_j]_l\}^{-1} \hat{\mathbf{J}}_t \quad (3.7.15)$$

sLORETA essentially converts the recorded electrode potentials at the scalp into standardized current densities in the source space, revealing much more valuable information in determining the actual sources of activity portrayed by the recordings.

3.8 Source Features

Both LCMV and sLORETA reconstruct the activity of all source points in the source model which is the discretized brain volume. Source localization is accomplished by obtaining the locations of local maxima in the neural activity index or current density map. One of the challenges in using LCMV occurs when multiple sources are active simultaneously during the time interval of the mental task. As a result, the neural activity index map will likely indicate a broad region of activity and individual sources will not be evident (Van Veen et al. [1997]). Therefore, localization of sources for mental tasks that activate several regions is suboptimal and inspecting the activity of regions of interest (ROI) seems more promising.

The setting of ROIs is generally nontrivial (Lindgren [2017]) as the shape, the

extent and the location of the ROI should be based upon empirical evidence, while this information is not established for all EEG paradigms. Additionally, despite the large number of source points in the source model, the effective resolution of source reconstruction is typically low due to reconstructed sources blending together (Baillet et al. [2001]). This is known as the source leakage effect and consequently forcing a strict ROI risks some information being reconstructed outside the ROI. Moreover, the spatial region of the ROI is not the only concern. Not only can an ROI change temporally and spectrally for a specific mental process, but also they are user-dependent.

Hence, restricting ROIs to pre-specified regions can be risky and may miss the actual active area. Therefore, in this study the ROIs are not limited to certain regions of the brain; instead, all the sources on the cortical surface are reconstructed and divided into regions based on Brodmann’s atlas to obtain the average activity of all Brodmann areas (Brett et al. [2001]). Lastly, data-driven statistical approaches are used to specify the most relevant ROIs for each task.

3.9 Machine Learning for BCI

In general, BCI systems rely on signal processing and machine learning algorithms to decode brain activity. Machine learning is used to learn the assignment of samples to their corresponding classes and predict the class for a new sample based on the learned patterns. This can be mathematically formulated as:

$$\hat{\mathbf{y}} = f(\mathbf{X}, \theta). \tag{3.9.1}$$

Function f takes a measured brain activity \mathbf{X} and produces an output based on a set of model parameters θ which were learned from the training set (Iturrate et al. [2020]). The recorded signals contain a mixture of components, some of which have and some have not directly originated from the brain such as muscular or movement artifacts, as well as electromagnetic noise. Therefore, the signal is typically processed to extract signal components that are correlated to the mental processes of interest. These components are referred to as features.

Depending on the application, the decoded output can be either a continuous value, e.g., hand velocity (Carmena et al. [2003]) or a discrete command, e.g., decoding motor imagery of the left vs right hand. As the target or the dependent variable in this thesis takes values from a discrete set, the research problems of interest are classification problems in which the input space can be divided into subregions. The decision boundary between the classes can have a smooth linear form or non-linear shape requiring investigation of different modelling methods.

In this thesis several linear and non-linear machine learning and statistical methods have been used which are discussed in more detail in the following sections. It is worth mentioning that there are various criteria to measure and report the performance of an ML algorithm such as the precision (number of true positives divided by the number of false positives plus true positives), recall (number of true positives divided by the number of true positives plus false negatives), the F_1 score ($2 * ((\text{precision} * \text{recall}) / (\text{precision} + \text{recall}))$), the accuracy and the confusion matrix. Throughout this thesis the performance is reported in terms of accuracy as misclassification error.

This is known as the empirical error rate:

$$\hat{L}_n = \frac{1}{n} \sum_{i=1}^n I(\hat{y}(\mathbf{x}_i) \neq y_i) \quad (3.9.2)$$

where $I(x)$ is the identity function, \mathbf{x}_i is a data sample in the test set, $\hat{y}(\mathbf{x}_i)$ is the predicted class label for the test sample and y_i is the true class label of the sample.

3.9.1 Feature Selection

Feature selection methods are techniques for downsizing the feature space of high-dimensional data by identifying a subset of the original features according to certain evaluation criteria, which is a common problem in machine learning (Cai et al. [2018]). They reduce the number of features and remove irrelevant, noisy and redundant features. These methods, including best subset selection, forward and backward stepwise selection, recursive feature elimination (RFE) etc. differ from dimension reduction techniques. Dimension reduction refers to the process of reducing the number of features to a set of key features while preserving the information as much as possible by transforming the input feature space onto a lower-dimensional subspace or a different space, and selecting the most important axes. Some well-known examples of feature reduction methods are principal component analysis (PCA) and partial least squares (PLS).

Datasets with a higher number of features than observations ($p > n$) usually have many redundant or irrelevant features which are better to be removed before being analyzed by a classification or regression method. Generally speaking, the number of features determines the number of parameters considered while modelling the data

and the model complexity increases with the number of features. Typically, the more complex the model, the better it fits the data in the training set, however, as more parameters are added to the model, there is a higher chance that the noise is also modeled. This leads to a lack of balance in the classic problem of bias-variance tradeoff and overfitting ([Friedman et al. \[2001\]](#)). Therefore, as a rule of thumb in machine learning, the lower the number of features, the more generalizable the model. Needless to say, feature reduction increases model interpretability by reducing the complexity of the final model. Additionally, the fewer number of features saves computational cost by accelerating the training phase of modelling.

The motivation for feature reduction can be summarized as follows:

- Where the number of features p is considerably larger than the number of observations n , there is a potential for the feature set to provide an extremely sparse representation of the data, with any given feature only capturing a small region of the data distribution. Consequently, models trained on such high-dimensional data are more likely to overfit due to the curse of dimensionality, and hence to have reduced predictive performance on test data.
- For many algorithms, the computational cost and training time both increase as the number of features increases.
- Obtaining a dimensionality-reduced feature space which is predictive of the outcomes can be very important in terms of knowledge discovery, interpretability perspective and model visualization.

Therefore, a good feature selection method can improve model prediction accuracy, reduce computational time and cost, and simplify model results ([Cai et al. \[2018\]](#)).

The Maximum Relevance Minimum Redundancy (mRMR) method, which has proven to be effective in BCI applications, has been utilized in this thesis.

Maximum Relevance Minimum Redundancy (mRMR)

Minimum redundancy maximum relevance (mRMR) is one of the most popular feature selection methods with widespread application. This method is essentially a filter with a forward selection (Peng et al. [2005]). In every step, the set of selected features will be expanded by adding the next one to maximize relevance in relation to the target variable and simultaneously to minimize the redundancy among the already selected features. Assuming the data is represented with a total of m features. For a given feature $x_i, i \in \{1, \dots, m\}$, its importance based on the mRMR criterion can be expressed as:

$$f^{mRMR}(x_i) = I(Y, x_i) - \frac{1}{|S|} \sum_{x_s \in S} I(x_s, x_i) \quad (3.9.3)$$

where Y is the class label, S is the set of selected features, $|S|$ is the size of the feature set (number of features), $x_s \in S$ is one feature out of the feature set S , x_i denotes a feature currently not selected: $x_i \notin S$. The function $I(\Delta, \Delta)$ is the mutual information calculated as:

$$I(X, Y) = \int_{\Omega_Y} \int_{\Omega_X} p(x, y) \log \frac{p(x, y)}{p(x)p(y)} dx dy \quad (3.9.4)$$

where Ω_Y and Ω_X are the sample spaces corresponding to Y and X , $p(x, y)$ is the joint probability density, and $p(\cdot)$ is the marginal density function. In the mRMR feature selection process, at each step, the feature with the highest feature importance score will be added to the selected feature set S .

3.9.2 Classification

In this thesis two different classifiers were explored for binary classification of various mental tasks. Linear discriminant analysis offers a simple yet effective linear approach toward discriminating between different classes of a dataset. The support vector machine, on the other hand, is one of the most widely used classification methods in machine learning that still has a simple implementation. Both of these classifiers are fast and widely used in mental process decoding in the BCI literature and their efficacy has been examined in offline and online setups ([Rashid et al. \[2020\]](#)).

Linear Discriminant Analysis (LDA)

Derived from Bayes theorem, linear discriminant analysis (LDA) attempts to find a decision boundary between every pair of classes in a multi-class classification problem ([Friedman et al. \[2001\]](#)). According to the decision theory for classification, it suffices to calculate the $P(Y|X)$ where X consists of all the samples in the dataset and Y includes the labels of the samples. Given the prior probability π_k of being in class k and the class-conditional distribution $f_k(x)$, $P(Y|X)$ can be calculated by Bayes' theorem as:

$$P(Y = k|X = x) = \frac{f_k(x)\pi_k}{\sum_{l=1}^k f_l(x)\pi_l}. \quad (3.9.5)$$

Although it can be proven that for any given dataset the Bayes rule models the optimal classifier in terms of minimizing the true error rate, the calculation of the class-conditional density and prior is not always feasible. General density estimation and parametric techniques can be used to estimate these unknowns from the data. As a common approach, the class-conditional density $f_k(x)$ can be assumed to have

a multivariate Gaussian distribution:

$$f_k(x) = \frac{1}{(2\pi)^{p/2} |\Sigma_k|^{1/2}} e^{-\frac{1}{2}(x-\mu_k)^T \Sigma_k^{-1} (x-\mu_k)}. \quad (3.9.6)$$

A decision boundary between class l and k can therefore be calculated:

$$\text{Decision Boundary} = (x | P(Y = l | X = x) = P(Y = k | X = x)). \quad (3.9.7)$$

Solving (3.9.7) for x , assuming the covariance of all the classes are equal ($\Sigma_k = \Sigma \forall k$) for simplification, the decision boundary would be:

$$\begin{aligned} \log \frac{Pr(G = k | X = x)}{Pr(G = l | X = x)} &= \log \frac{f_k(x)}{f_l(x)} + \log \frac{\pi_k}{\pi_l} \\ &= \log \frac{\pi_k}{\pi_l} - \frac{1}{2}(\mu_k + \mu_l)^T \Sigma^{-1} (\mu_k - \mu_l) + x^T \Sigma^{-1} (\mu_k - \mu_l). \end{aligned} \quad (3.9.8)$$

This above equation is linear in terms of x which implies the decision boundary between the classes k and l is a hyperplane in p dimensions. Thus, the linear discriminant function is denoted as:

$$\delta_k(x) = x^T \Sigma^{-1} \mu_k - \frac{1}{2} \mu_k^T \Sigma^{-1} \mu_k + \log \pi_k. \quad (3.9.9)$$

For an unseen input vector, LDA computes the discriminant function for all classes and the largest value would be the predicted class label. Hence, the decision rule for any new sample is:

$$Y(x) = \arg \max_k \delta_k(x). \quad (3.9.10)$$

In practice, the parameters of the Gaussian density function are unknown and

should be estimated from the training data as below:

- $\hat{\pi}_k = N_k/N$, N_k is the number of class k observations
- $\hat{\mu}_k = \sum_{g_i=k} (x_i/N_k)$
- $\hat{\Sigma} = \sum_{k=1}^K \sum_{g_i=k} (x_i - \hat{\mu}_k)(x_i - \hat{\mu}_k)^T / (N - K)$

Support Vector Machine(SVM)

While LDA is essentially a statistical method, the support vector machine (SVM) is considered to be a machine learning algorithm. The fundamental difference between these two approaches is that ML approaches explore and learn the data without any prior assumptions regarding the density and distribution of the data while statistical methods are built on assumptions about the data distribution. As mentioned in section (3.9.2), the fundamental assumption of the LDA method is normality of the independent variables.

The SVM was initially introduced for binary classification problems and can be expanded to multi-way classification schemes by solving multiple binary problems. The SVM aims to find a linear decision boundary in feature space by forming a hyperplane which linearly separates the data points belonging to the two classes in the multi-dimensional feature space (Boser et al. [1992]). The working principle of this technique is maximizing the distance between the data samples and the decision boundary. The subset of the training set which constitute the closest data points to the discriminating boundary are known as “support vectors” and the solution is formulated as a linear combination of these supporting patterns.

A hyperplane can be formulated with its normal vector W and its offset from the origin along the normal vector $\frac{b}{\|W\|}$ as a set of points x satisfying $W^T x - b = 0$. The

goal is to find W and b such that the hyperplane is optimally placed the furthest possible from the samples of both classes. A margin is defined to ensure no data point is closer to the hyperplane than the specified margin: $|W^T x_i - b| < 1$ where x_i is the i th member of an n point dataset pairing with its label y_i . However, most datasets are not linearly separable and to accommodate this, the problem is to be reformulated as an optimization problem to minimize a loss function. Consider the distance between a data point and the hyperplane $\max(0, 1 - y_i \times (W^T x_i - b))$ based on the “hinge loss function”. If a data point is on the correct side of the hyperplane and its distance is greater than 1, then the loss would be 0; otherwise, the loss would be proportional to the distance of the data point from the soft margin. Therefore the goal is to minimize the total loss:

$$\min_{W,b} \left[\frac{1}{n} \sum_{i=1}^n \max(0, 1 - y_i \times (W^T x_i - b)) \right] + \lambda \|W\|^2 \quad (3.9.11)$$

where λ controls the trade-off between the size of the margin (soft margin) and the number of data points it is letting in the margin and not penalizing. In the case that the data is not linearly separable, a kernel method ([Friedman et al. \[2001\]](#)) can be used to transfer the data into a new space in which data might be linearly classifiable. Common kernel functions used are Gaussian and polynomial. While performing model selection for a dataset, the soft margin, the type of the kernel and its parameters should be tuned in a cross-validation scheme. This step is known as hyperparameter tuning. It is worth mentioning that a good generalization performance of a classification algorithm lies in the learning capacity of the classifier matching the size of the training set. As a result, if a very complex model containing plenty of parameters is used to model a small amount of data, the generalization will be poor

due to overfitting. However, the SVM uses the size of the margin to automatically adjust the learning capacity of the model and optimizes generalization ([Boser et al. \[1992\]](#)).

Chapter 4

Motor Imagery-Based BCI in Source Space

4.1 Chapter Introduction

As discussed in previous chapters, the aim of this thesis is to assess utilization of two source localization methods, the LCMV beamformer and sLORETA, in BCI pipelines. The bulk of spontaneous BCI research has been built on “motor imagery” commands and numerous algorithms have been tested using this paradigm. According to the large number of review papers in the field, this problem has a favourable solution and the best identified methods for decoding motor imagery from EEG signal are the family of CSP-based methods ([Rashid et al. \[2020\]](#), [Saha et al. \[2021\]](#), [Abiri et al. \[2019\]](#)). This is the very reason which makes this paradigm beneficial to test new algorithms that are hypothesized to perform well or better than existing methods. Analysis of motor imagery data has several benefits:

- Replicating comparable results can be a way of testing the correctness of the new analysis pipeline’s implementation since the expected results are known.
- The availability of benchmark datasets on which plenty of methods have already been applied provides a reliable comparison ground for our proposed pipeline against existing methods and facilitates answering novel research questions.

Therefore in this chapter motor imagery decoding using SL methods has been investigated as a preliminary analysis and a proof-of-concept scheme to build on more sophisticated pipelines and decoding other mental imagery forms. As the benchmark data, the BCI IV competition dataset 1 ([Blankertz et al. \[2007a\]](#)) was analyzed using five BCI pipeline designs to probe three research questions propounded in the next section.

4.2 Objectives

The main research questions (RQ) investigated in this chapter are:

RQ1: Does adding the beamforming step before extracting CSP features boost the BCI pipeline performance? In other words, are CSP features extracted from source space more informative than those extracted from sensor space?

RQ2: How do the LCMV beamformer and CSP compare with each other as two types of spatial filters?

RQ3: Is the LCMV beamformer as a spatial filter more successful in reconstruction of motor imagery activity relative to sLORETA as a minimum norm-based solution?

4.3 Dataset

4.3.1 EEG Paradigm

The BCI IV competition, dataset 1 named “motor imagery, uncued classifier application” provided by the Berlin BCI group was analyzed in this chapter and can be freely accessed ([Blankertz et al. \[2007a\]](#)). The BCI competition IV held in 2008 aimed to validate signal processing and classification methods for brain-computer interfaces posing 4 main challenges on 4 datasets, 2 of which were EEG data. Although the main research question of dataset 1 was classification of continuous EEG without trial structure (uncued) to support the idea of “self-paced BCI”, this dataset was the only one with a reasonable number of channels (59) for source localization purposes and thereby, chosen for analysis here.

The dataset consists of single trials of spontaneous brain activity, one part labeled (calibration or training data) and another part unlabeled (evaluation or test data). 4 healthy individuals were recorded with 59 Ag/AgCl electrode EASYCAP GmbH using BrainAmp MR plus amplifiers. The electrodes were most densely distributed over motor areas and channel labels and location were provided in the 10-05 standard (figure 4.2). Signals were band-pass filtered (Chebyshev Type II filter of order 10 with stop band ripple 50dB down and stop band edge frequency 49 Hz) between 0.05 and 200 Hz and then digitized at 100 Hz with 16 bit ($0.1 \mu V$) accuracy.

Participants were assigned to perform two classes of motor imagery selected from the three classes left hand, right hand, and foot (side chosen by the subject; optionally also both feet). In calibration data, each trial of motor imagery was performed without feedback for 4s periods during which the visual cues were presented on the

screen as arrows pointing right, left, or down. These periods were interleaved with 2s of blank screen and 2s with a fixation cross shown in the center of the screen. The fixation cross was superimposed on the cues, i.e., it was shown for 6s and a break of 15s was given after every 15 trials. The participant was instructed to perform the motor imagery right after the offset of the cue until presented with the black screen. A total of 100 trials per condition was recorded for each subject. Figure 4.1 demonstrates the organization of the experimental paradigm.

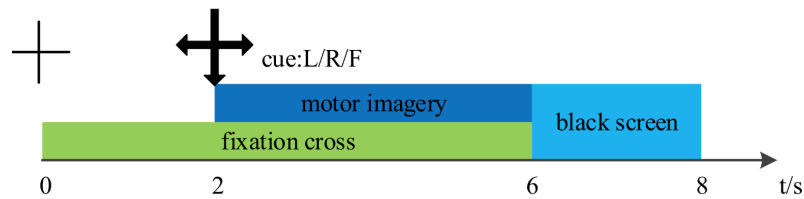


Figure 4.1: BCI IV dataset 1 paradigm.

The evaluation data consist of imagery tasks where the start was cued by soft acoustic stimuli (words left, right, and foot) and the end was cued by the word stop. The imagery and intermediate periods had varying duration between 1.5 and 8 seconds and the number of trials from each condition were not equal. Since the evaluation data were imbalanced and recorded with a different protocol (different cue type and length of the imagery trials) only the calibration data were analyzed here. Also, some of the datasets were artificially generated which were omitted in this analysis (subjects c, d and e).

4.3.2 EEG Cleaning and Preprocessing

An initial data inspection via scrolling through the time-domain EEG signals revealed that the provided data were not cleaned and required preprocessing. The data are

4.4 Processing Pipelines

In order to answer the above mentioned research questions, five variations of a BCI pipeline are proposed and compared here with the main difference being the feature extraction block. Essentially, the pipelines can be divided in two categories: sensor and source space based pipelines. In sensor space based pipelines, common spatial patterns were used as they have been found to generate highly distinctive features in motor imagery classification problems. In terms of source space based pipelines, the sLORETA and the LCMV beamformer were utilized and two types of features, namely CSP and source time-averaged power were extracted and performances were compared. It is worth mentioning that although the CSP spatial filter maps the data from sensor space onto a different space where the patterns are more separable, it is referred to as a “sensor space pipeline” due to the fact that it is applied on sensor data rather than source data.

Regarding the source localization specifics, the Montreal Neurological Institute (MNI) Colin27 template MRI (a stereotaxic average of 27 T1-weighted MRI scans of the same individual named Colin) ([Holmes et al. \[1998\]](#)) was used as the default subject anatomy to compute a three-compartment (scalp, skull, and cortex) head model with the symmetric boundary element method (BEM) using the dipoli method in FieldTrip ([Mosher et al. \[1999\]](#)). FieldTrip default settings were used for the LCMV beamformer and the lambda regularization parameter was set to 10% of the average eigenvalue of the covariance matrix for sLORETA source reconstruction. The source reconstruction was performed for a 3D grid of dipoles with 1cm resolution covering the whole brain volume with more than 1800 source points.

Since the motor imagery activity is known to originate from the motor cortex, the

cortical surface (a total of 369 source points) was of interest in this study in order to reduce the dimensionality of the problem and increase power. WFU PickAtlas (developed based on the Talairach brain atlas and adapted to the MNI coordinate system) provided by Wake Forest University, school of medicine ([Maldjian et al. \[2003\]](#)) was used to select the source points comprising the cortical surface which was further parcelled into Brodmann areas (BA) as the regions of interest (ROI). Due to the resolution of 1cm, 37 BAs were detectable in the generated head model, forming a total of 74 half-Brodmann areas on both brain hemispheres. In terms of extracting CSP features, it should be noted that a total of N features can be computed where N is the number of time series (electrodes or sources) in every trial. Thus, 59 and 396 CSP features can be computed from sensor and source data respectively. However, pairs of top and bottom features, which are ranked based on common eigenvalues, comprise the most distinctive feature sets. This introduces a hyperparameter (the number of CSP features to select) into the problem which should be identified in a cross validation loop. Here, after testing using different numbers of CSP features, four features were used (top 2 and bottom 2) in order to achieve high performance while having a sparse feature space.

Finally, two different classifiers, a linear Support Vector Machine (SVM) and Linear Discriminant Analysis (LDA) were trained and tested in 5-fold cross validation schemes for binary classification of motor imageries. Figure 4.3 illustrates the general pipeline and various features employed in each version of the pipeline. The feature extraction block specifics of pipelines (PL) are listed in table 4.1. In all tests the random number generator seed was set to 0 for reproducibility of the results.

Table 4.1: Feature extraction block of all BCI pipelines explored in this chapter.

Pipeline	Features	Feature No.
PL1	Four most discriminating CSPs of sensor space	4
PL2	Four most discriminating CSPs of reconstructed cortical sources by LCMV beamformer (CSP are extracted from 396 source points)	4
PL3	Four most discriminating CSPs of reconstructed cortical sources by sLORETA (CSP are extracted from 396 source points)	4
PL4	ROI spatial average power of sources reconstructed by LCMV beamformer (mRMR feature selection method was applied)	74
PL5	Power of cortical sources reconstructed by sLORETA (396 source points)	396

4.5 Results

The performance of the five proposed BCI pipelines are reported in 2 pairs of tables and plots, organized in a way to best answer the research questions. The results of the analyses addressing RS1 are presented in table4.2 and plot4.4 while the results of the analyses regarding RS2 and 3 are presented in table4.3 and plot4.6. The baseline of the comparisons is the performance of PL1 where CSP features were extracted from sensor EEG data and classified with a linear SVM.

Table4.2 and plot4.4 (for convenient visual comparison) show the difference in performance when extracting CSP from sensor and source space. Since the performance of the SVM was better than that of the LDA in most cases, the results for the LDA classifier are only reported for the first pipeline (PL1). The results indicate that for all subjects the performance of the SVM classifier on common spatial patterns extracted from source and sensor data are very close and do not differ significantly. In the case of CSP extracted from source space, using the LCMV beamformer

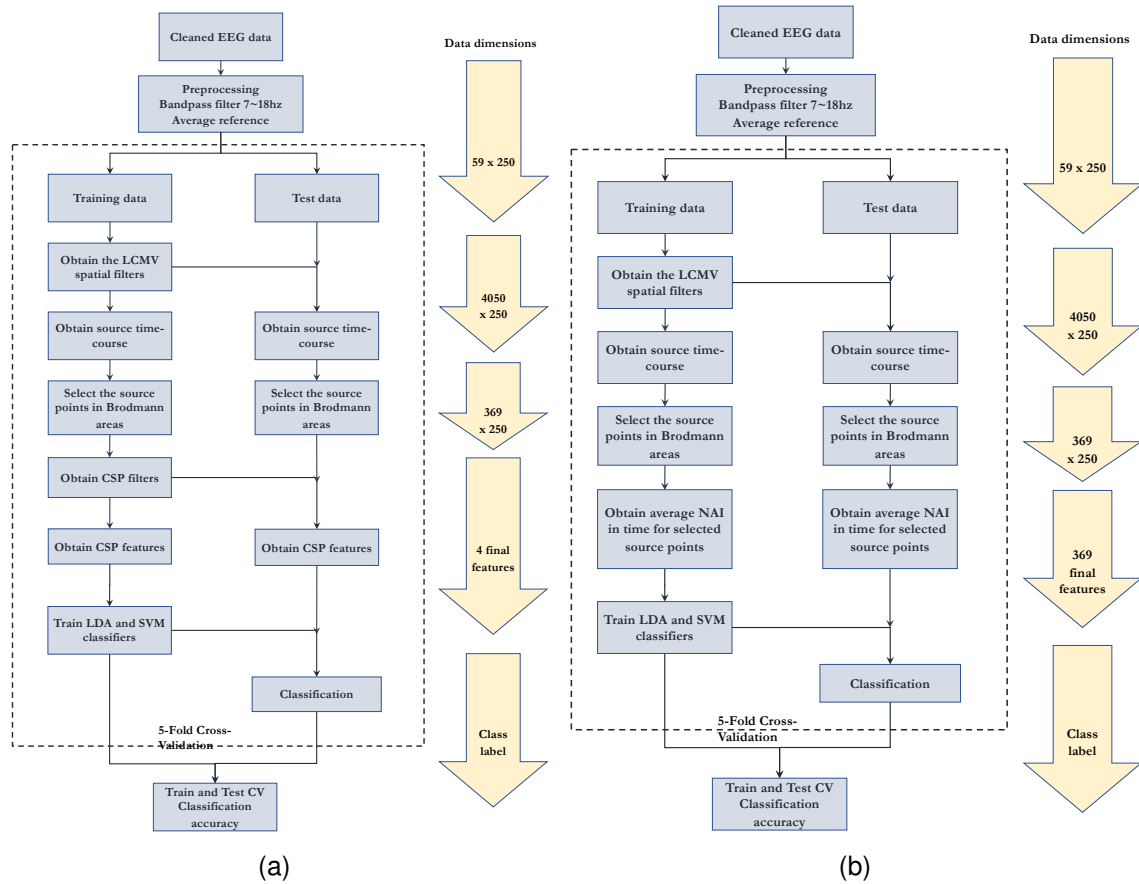


Figure 4.3: Illustration of two of the processing pipelines. (a) PL 2 Classification of motor imagery trials based on Common Spatial Patterns (CSP) of cortical sources. (b) PL 4 : Classification of motor imagery trials based on average power or Neural Activity Index (NAI) of half-Brodmann areas. The LCMV and CSP spatial filters and mRMR feature selection were applied to the training segment of the data and the computed filters were then applied on test data. The same goes for mRMR selected feature indexes.

yields slightly better performance, with a mean accuracy of 81.23%, in comparison to sLORETA with a mean performance of 75.62% while also having lower variation in CV folds' performance (lower standard deviation). In all these 3 pipelines, the four most discriminative CSPs (top two and bottom two) were used for classification.

Regarding PL4 where the features are the average power of half-Brodmann areas, the mRMR feature selection method was applied to find the best subset of features

Table 4.2: 5-fold cross validation accuracy [%] of binary classification of motor imageries in source and sensor space pipelines for 4 subjects in BCI IV dataset 1.

Method	CSP at Sensor Space		CSP at Source Space	
	LDA CV Test Accuracy (PL1)	SVM CV Test Accuracy (PL1)	LCMV, SVM CV Test Accuracy (PL2)	SVM-sLORETA CV Test Accuracy (PL3)
Sbj a	70.85 ± 3.01	69.80 ± 2.90	70.15 ± 1.16	65.00 ± 15.75
Sbj b	79.85 ± 2.46	80.40 ± 0.97	80.15 ± 6.22	67.50 ± 12.0
Sbj f	85.15 ± 1.68	84.80 ± 2.16	85.25 ± 8.59	83.50 ± 4.54
Sbj g	88.70 ± 2.18	91.50 ± 1.68	89.40 ± 8.48	87.23 ± 8.18
AVG ± STD	81.13 ± 2.33	81.62 ± 1.93	81.23 ± 8.74	75.62 ± 10.12

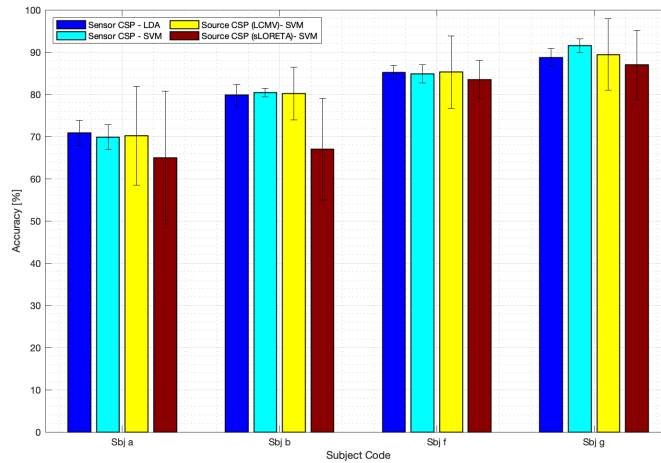


Figure 4.4: 5-fold cross validation accuracy [%] of binary classification of motor imageries in source and sensor space pipelines for 4 subjects in the BCI IV dataset 1.

and lower the dimensionality of the feature space. The computed features were ranked using the mRMR principle. The number of top features to be used for classification, K , was tuned using a cross-validation. Figure 4.5 shows using 50 half-BAs achieves high accuracy, whereas moving toward 60 features decreases the test accuracy.

According to the results presented in table 4.3 and plot 4.6, the average activity of selected ROIs during the course of motor imagery is as discriminative a feature as the

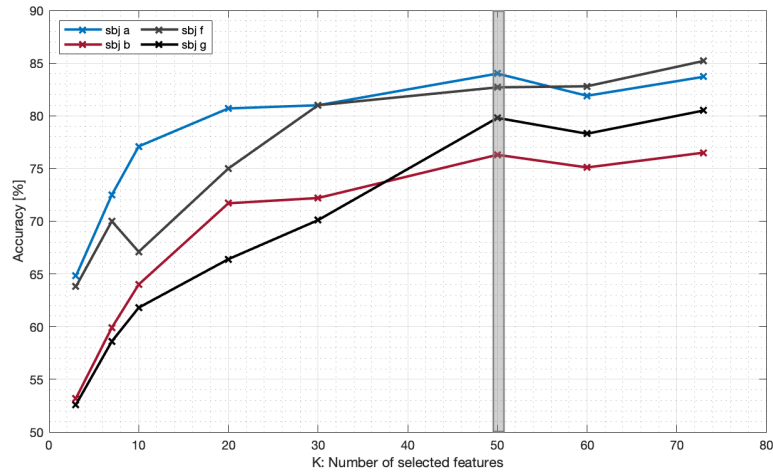


Figure 4.5: BCI IV dataset 1 paradigm.

CSPs obtained from electrode signals. While the average performance of all these four pipelines are very similar, using source activity in place of sensor CSP features, there is an improvement from 69.8% to 84.0% in the motor imagery decoding of subject a. Also, for the other three subjects (b, f and g), applying the CSP algorithm on top of the LCMV beamformer slightly improves the classification results in comparison to only using the sources' power obtained from the LCMV beamformer. However, in the case of subject a, for whom CSP feature extraction does not perform as well as for other subjects, using only the average activity of specific Brodmann areas achieved higher performance.

This observation might be due to the original underlying neural activity and can be an indicator that subject a is performing the motor imagery task differently than other participants. It can be hypothesized that instead of involving one or two large brain areas, this participant was engaging a greater number of smaller brain areas or a larger separable network. Learning a stable differentiable pattern on this kind of brain activity is harder for the CSP method. However, the LCMV beamformer might

Table 4.3: 5-fold cross validation accuracy [%] of binary classification of motor imageries in source and sensor space pipelines for 4 subjects in BCI IV dataset 1 comparing CSP and source power features.

Method	CSP at Sensor and Source Space		Power of Cortical Sources	
	SVM CV Test Accuracy (PL1)	LCMV, SVM CV Test Accuracy (PL2)	Avg half-BA Power LCMV, SVM Test Accuracy (PL4)	Source Power sLORETA SVM CV Test Accuracy (PL5)
Sbj a	69.80 ± 2.90	70.15 ± 1.16	84.00 ± 7.00	74.00 ± 5.18
Sbj b	80.40 ± 0.97	80.15 ± 6.22	76.30 ± 6.94	76.50 ± 5.18
Sbj f	84.80 ± 2.16	85.25 ± 8.59	82.70 ± 8.18	82.50 ± 4.68
Sbj g	91.50 ± 1.68	89.40 ± 8.48	79.80 ± 8.40	87.50 ± 5.18
AVG ± STD	81.62 ± 1.93	81.23 ± 8.74	80.70 ± 7.63	80.12 ± 5.05

have an advantage in these cases as it can reconstruct the activity of each region of the brain separately from other parts. This hypothesis is further investigated by analyzing the selected features for each subject.

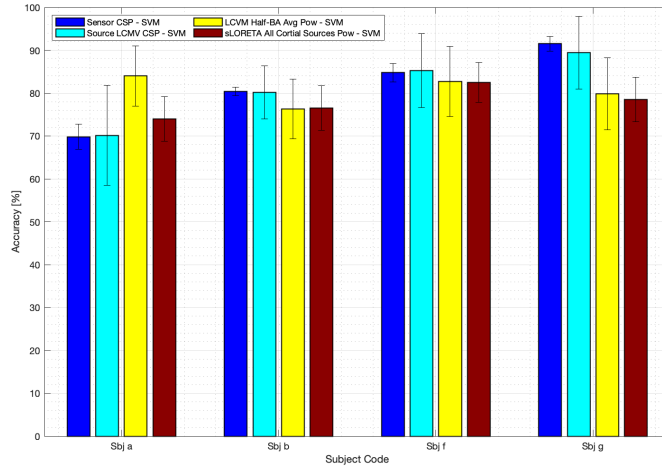


Figure 4.6: 5-fold cross validation accuracy [%] of binary classification of motor imageries in source and sensor space pipelines for 4 subjects in the BCI IV dataset 1 comparing CSP and source power features.

In a 100-fold cross validation loop, the top 50 features selected by the mRMR

algorithm were recorded in order to analyze the distribution of the selected features. The indexes of the selected features were investigated to identify the proportion of the features which were consistently selected in all folds. Figure 4.7 demonstrates the number of the features repeated in more than 70% and 90% of the folds as well as the total number of unique features selected in all 100 folds. For subject a, 49 out of 50 selected features were the same in more than 70% of the folds and 44 out of 50 were the same in more than 90% of the folds. Although the number of unique features selected for subject a is lower than all other subjects, these measures are close for subject b and g which doesn't lead to a conclusion regarding the difference between the actual distribution of sources in subject a versus others. However, based on the results presented in figure 4.7, on average 92.5% of the selected features were the same in more than 70% of the folds and 75.5% of selected features were the same in more than 90% of the folds which is a strong indication of robustness of the method as well as reasonable variation among trials of each motor imagery task.

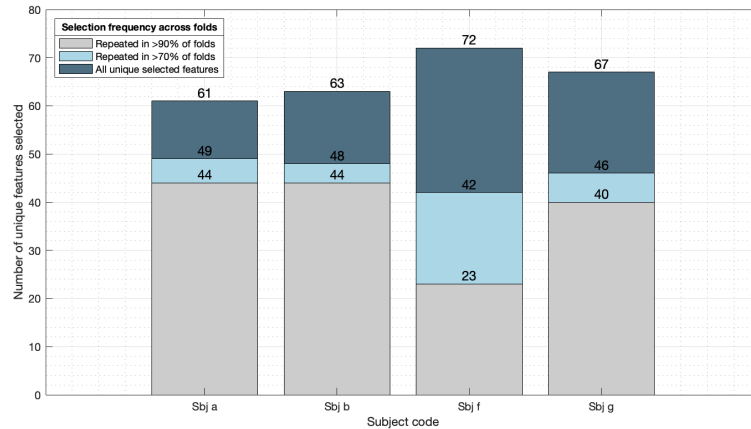


Figure 4.7: Distribution of selected features by mRMR algorithm across folds in a 100-fold CV scheme (80% train-20% test split) for pipeline PL 4 where features are the average activity of half-BAs and 50 top features are selected.

4.6 Discussion

According to the presented results, CSP features extracted from source space are as informative as CSP features extracted from sensor space, whereas adding the beamforming step before extracting CSP features does not significantly change the BCI pipeline performance (RQ 1). This result is in agreement with previous findings in the literature. A very similar study compared classification of FBCSP features extracted from sensor space and reconstructed sources with the wMNE method ([Zaitcev et al. \[2019\]](#)); their 4-class classification results on the BCI competition IV dataset 2a show an average accuracy of $74.4 \pm 8.9\%$ when applying FBCSP to sensor data while $76.8 \pm 9.5\%$ when applying FBCSP on source data which shows a close level of performance.

Another similar study extracted CSP features from 24 selected cortical ROIs covering only the motor areas ([Xygonakis et al. \[2018\]](#)). The CSP features were computed on each ROI separately to form the ROI's feature vector. Classification was performed using an ensemble model comprising 24 LDA classifiers, each of which was defined on an individual ROI. The evaluation was performed on the BCI Competition IV dataset 2a, containing EEG recordings of 9 participants performing 4 motor imagery tasks. A mean accuracy increase of 5.6% was observed using the features extracted from source space with respect to the conventional computation of CSP on sensors (from 54.1% accuracy to 59.7%). The increase in performance could be due to the fact that ROIs were specifically defined on motor areas which can increase the power. However, since the final goal of this thesis is to develop a BCI operating with various type of mental imageries, restricting ROIs to a certain region was avoided. Overall, in both similar studies, the performance of CSP applied at sensor and source space

are very close and consistent with this chapter’s results.

As discussed elaborately in the background section, the reason behind the hypothesis that “applying a beamformer before CSP will improve the performance of CSP” was that a beamformer compensates for the head volume conduction and improves the SNR, and thus, increases the ability of CSP to generate more separable filters. A simple reason for achieving similar performance here could be the distribution of electrodes on the scalp. Source localization methods are very sensitive to the number and distribution of electrodes ([Michel and Brunet \[2019\]](#)) and while the number of sensors was high enough in the BCI IV dataset 1, the electrodes were more densely located on motor areas ([figure 4.2](#)). This can interfere with the accuracy and quality of the reconstructed sources and thus, not improve the SNR as expected. Additionally, when mapping from sensor to source space, 64 EEG signals will form 369 source signals. Thus, CSP filters have to be computed on a matrix with 6X higher dimensionality than before and this additional complexity might adversely affect the performance of CSP.

Regarding RQ 2, when comparing the LCMV beamformer and common spatial patterns as two types of spatial filters, no significant difference in performance was detected. This result matched previous findings in the literature comparing beamforming with CSP and Laplacian spatial filtering (LP) in a two-class motor imagery paradigm ([Grosse-Wentrup et al. \[2009\]](#)). It was demonstrated that beamforming outperforms CSP and LP on noisy datasets, while CSP and beamforming perform almost equally well on datasets with few artifactual trials. In summary, it is not intended to argue that either CSP or beamforming perform superior to one or the other in general. While CSP probably provides theoretically optimal spatial filters

(Grosse-Wentrup and Buss [2008]), beamforming can be particularly useful if CSP fails to compute sensible spatial filters—whether this is due to subjects not being able to induce strong modulations of their μ -rhythm, a strong contamination of the recorded EEG by artifactual components, or too few training trials being available.

Furthermore, there is evidence that CSP and beamforming favour different spectral bands which might indicate that these approaches extract (at least partially) independent information on the subject’s intention (Grosse-Wentrup et al. [2009]). This observation, in addition to better performance by the LCMV beamformer on subject a in the results reported here, suggests other ways of combining CSP and beamforming, such as forming a feature set comprising of obtained features from both methods, might prove to be useful.

Regarding the last research question, RQ 3, since the bulk of EEG studies in source space have utilized a variation of MNE, such as wMNE or sLORETA, here the LCMV beamformer was compared with sLORETA. The results showed that the LCMV beamformer as a spatial filter is more successful in reconstruction of motor imagery activity than sLORETA as a minimum norm-based solution. However, it does not answer this question in general as both methods can be further enhanced by using subject-specific MRI and fine tuning the regularization parameter which might be more compatible with the actual neurophysiological activity of motor imagery mental tasks.

It should be mentioned that since the results of the original competition were reported on the evaluation data and it is a 3-way classification (2 motor imagery and no imagery or rest), the results provided here are not comparable with the original competition results. However, CSP in a narrow frequency band as a simpler form of

the winning algorithm, FBCSP ([Zhang et al. \[2012\]](#)), was applied and compared here with the source localization pipeline.

In conclusion, this study shows source reconstruction using the LCMV beamformer and the application of CSP filters at the source space constitute a robust, promising solution to decoding mental commands in non-invasive BCIs. While the proposed pipelines are still not significantly superior to the state of the art of BCI algorithms for decoding instructed motor imageries, feature extraction in source space can improve performance in cases where CSP might not perform well. Further investigations are required to find out the fundamental differences between the brain activity of subjects for which CSP features are more classifiable and subjects for which the power of Brodmann areas are more separable. Moreover, linear inverse operators, such as the LCMV beamformer, and sparse regions-of-interest are computationally simple enough to be applied in real-time settings. Based on the presented results, the LCMV beamformer was selected to move forward with. Additionally, in place of utilizing CSPs or average power of ROI sources as features, more advanced spectral and connectivity measures of sources' activity were used to decode a variety of mental imageries in the next chapter.

Chapter 5

Mental Imagery BCI in Source-Space

5.1 Chapter Introduction

In the previous chapter, several pipelines were compared in the motor imagery EEG paradigm and the effectiveness of the LCMV beamformer was confirmed. Although motor imagery can successfully be decoded in most individuals, it might not form the optimal set of commands for everyone due to differences in the pattern of brain regions activation while performing motor imagery tasks. On the other hand, if each person could use an individually chosen pair of mental imagery tasks that they are most adept at, or that are optimally separable, it is possible that everyone could achieve equally high BCI control. Therefore, in this chapter we explored peoples' ability to generate a wide range of different types of mental imagery, by mentally performing various mental commands. We then classified these commands using spectral power and connectivity measures extracted from source time-series reconstructed by

a beamformer. The main research question investigated in this chapter is: Is there an optimal pair of tasks for every individual that are very well separable using LCMV beamformer?

5.2 Dataset

5.2.1 EEG Paradigm

The dataset analyzed here was collected by Dr. Amabilis Harrison ([Harrison et al. \[2017\]](#)). This dataset, containing concurrent EEG-fMRI recordings, was initially collected from 17 healthy volunteers 5 of whom were excluded due to excessive artifacts. The remaining 13 subjects (10 female) had a mean age of 27.4 (range 21–48) years. Data were acquired in three runs, and each run consisted of six 16s trials where participants were asked to perform one of the following 7 mental imagery tasks after a single-word auditory cue ([Harrison et al. \[2017\]](#)):

1. Finger tapping imagery. Subjects were asked to imagine pushing a button with each of the fingers of the right hand in succession, repeatedly, focusing on the somatosensory and kinesthetic rather than visual aspects of the imagery.
2. Navigation imagery. Participants were asked to imagine navigating around their home from room to room, paying attention to all aspects of the room (e.g., placement of furniture, decor, objects in the room).
3. Music imagery. Participants were asked to choose a song that was very familiar to them, and were asked to imagine listening to that song through headphones,

concentrating on all aspects of the song, including the melody, the instrumentation, the rhythm, the lyrics, and the vocals (if present).

4. Sport-related motor imagery. Participants were asked to choose the sport or full-body activity (e.g., dancing, jumpingjacks) that is most familiar to them, and to imagine performing that activity intensely, focusing on the kinesthetic and somatosensory aspects of that activity rather than on visual aspects.
5. Running imagery. Similar to the sport imagery condition only in this case subjects were asked to imagine running. This task was chosen as a standard imagery condition of an activity with which all subjects would have some level of familiarity.
6. Mental arithmetic. Participants were asked to choose a different 3-digit number at random for each trial and count backwards by threes.
7. Rest. Participants were asked to clear their mind and think of nothing in particular.

Participants were asked to keep their eyes open and fixate on a central target, in order to avoid excessive eye movements, alpha EEG associated eye closing, and drowsiness. Conditions were presented in pseudo-random order, with no condition occurring more than twice in a row. These conditions were explained in detail before subjects entered the scanner ([Harrison et al. \[2017\]](#)).

5.2.2 EEG Cleaning and Preprocessing

Since the preprocessing steps required for preparation of EEG in order to be used in source localization methods are complex and must be chosen carefully, we closely

followed the steps recommended by [Michel and Brunet \[2019\]](#). Christoph M. Michel was not only one of the proposers of the LORETA and LAURA methods ([Pascual-Marqui et al. \[1994\]](#), [Peralta Menendez et al. \[2004\]](#)), but also one of the developers of the free EEG analysis software: Cartool [Brunet et al. \[2011\]](#) which provides various source analysis methods. Additional artifact removal steps were required, beyond those typical for pure EEG data, because the recorded EEG signals during the concurrent EEG-fMRI are compromised by several scanner-related artifacts, which can overwhelm the actual brain signal ([Huster et al. \[2012\]](#)). The artifact from the time-varying magnetic field gradients used for the MR imaging is the most significant artifact: large gradient artifacts (GA). Also, ballistocardiogram (BCG) artifacts, caused by cardiac-related activities, highly distort the EEG signals in the presence of a magnetic field. These two artifacts should be removed before any other EEG preprocessing take place.

Considering recent endeavours to establish best practice guidelines of reporting EEG/MEG studies ([Pernet et al. \[2018\]](#)), reporting the information regarding various steps taken in different software packages in publications is essential to guarantee reproducibility and replicability. Thus, this report has included all detail incorporated in the signal processing steps and chosen parameters. Blindly applying automatic artifact detection and removal algorithms to the data is problematic and therefore, the data was visually inspected in every cleaning step. The preprocessing steps applied to the EEG data were as follow:

1. MRI scanner gradient artifact correction based on “Scan Start volume” markers (not slice markers) using the average artifact subtraction procedure ([Allen et al. \[2000\]](#)) as implemented in BrainVision Analyzer (BVA) 2.1 software ([Brain](#)

Products, GmbH, Germany)

2. Signal downsampling from 5kHz to 500Hz
3. Temporal filtering: a. [1-100] Hz bandpass filtering using a Butterworth zero-phase IIR filter of 4th order (24 dB/octave roll-off); b. 60 Hz notch filter to remove line noise
4. Cardiac event detection based on the concurrent ECG recorded signal using the BVA software detection algorithm and exported as R-peak markers
5. Ballistocardiogram artifact correction based on detected R-peak markers using the optimal basis set (OBS) procedure with an optimal basis set of 3 principal components ([Niazy et al. \[2005\]](#)) implemented in FMRIB plug-in EEGLAB
6. Raw data inspection and marking any obvious large cable movement or motion artifacts in order not to be included in the ICA procedure
7. Bad channel removal and topographic spline interpolation of order 4
8. Ocular artifact removal using Infomax extended ICA based on Fp1 and Fp2 channels as vertical electrooculogram (VEOG) and horizontal electrooculogram (HEOG) activity respectively. (The independent component waveforms and corresponding topography were carefully inspected before selecting and removing the component. One or two components were rejected in each experiment block.)
9. Temporal filtering: a. 1-70 Hz bandpass filtering using a Butterworth zero-phase IIR filter of 4th order (24 dB/octave roll-off); b. 60 Hz notch filter to remove line noise

10. Re-referencing to common average (CAR)
11. Data segmentation into 14 second non-overlapping imagery epochs based on event markers (removing the first 2 seconds after the cue to avoid any responses related to auditory instructions) and segmentation of each imagery trial into four 3.5-second final epochs
12. Bad trial rejection using the semi-automatic setting in BVA combining automatic bad trial detection based on predefined criteria (a. two adjoining data points differed by more than $50\mu V$, b. a difference of more than $200\mu V$ was observed in a $200mV$ interval, or c. the absolute amplitude exceeded $100\mu V$) and visual inspection of individual trials

It is worth mentioning that temporal filtering can impact the phase, local extreme positions and time-course of the data ([Widmann and Schröger \[2012\]](#)). Since this can affect time-frequency and connectivity measures, the specific IIR Butterworth filter used here is computed linearly which eliminates any phase shifts and preserves the position of local maxima. The cleaned data were then inspected to ensure the correct pre-processing.

Since EEG source imaging methods are built on the precursor of scalp potential maps, investigation of the field topography is as important as waveform inspection ([Michel and Brunet \[2019\]](#)). One should look for irregular transient activity corrupting certain electrodes appearing in the shape of local “islands”. Causing local maxima underneath them, these outlier electrodes have a dramatic impact on the source localization results and should be smoothed out before feeding the data to SL methods. This can be done by spatial smoothing filters.

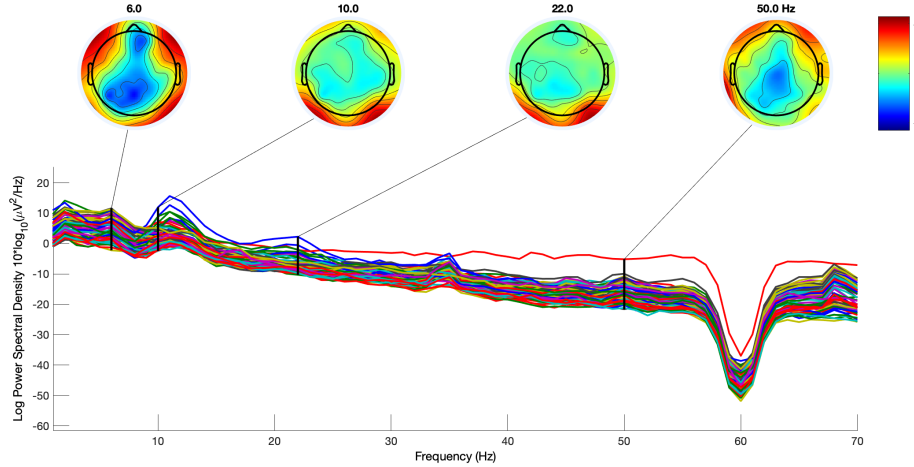


Figure 5.1: Power spectra of subject A, interval 1, mental arithmetic imagery

5.3 Processing Pipeline

Although source localization was used in the previous chapter (motor imagery decoding), the specifications of the processing pipeline are different in this chapter, especially the source localization configurations. Thus, a detailed explanation of solving the inverse problem is given here.

5.3.1 Source Localization Specifications

Forward Solution Specification

As explained previously, the forward problem determines the potential at each scalp electrode generated by a known source in the brain which is represented by a current dipole with unit amplitude at each of (x, y, z) directions (Baillet et al. [2001]). The model for which the forward solution is calculated is referred to as the head model or volume conduction model of the head. The signal attenuation cause by the skull

(variable thickness across the head) and other tissues should be modeled properly when solving the forward problem. Precise information of the head anatomy including the shape of the head and the skull thickness, which determines the local conductivity properties, are of importance and can be obtained from individual structural MRI.

Choice of Structural MRI:

The forward solution: “the leadfield” or gain matrix, which relates the activity of the brain sources to the electric activity at electrodes, is computed using three ingredients: 1- head model (obtained from MRI) describing the head geometry 2- brain tissue conductivity parameters and 3- the exact 3D location of the electrodes. It goes without saying that the preciseness of the inverse solution depends on the preciseness and anatomical correctness of the lead field. Although in most texts on the theory of source localization using an individual MRI has been emphasized, which is of utmost importance in clinical and presurgical applications, most research utilizing various SL methods on real or simulated data have used multiple-shell spherical head models ([Grosse-Wentrup et al. \[2009\]](#), [Seeland et al. \[2018\]](#), [Edelman et al. \[2015\]](#)) as obtaining individual MRI is expensive and not always accessible.

Additionally, a recent study comparing the three SL methods (wMNE, eLORETA and LCMV) using different head models claimed their results were relatively unaffected by the choice of the electrical head model ([Mahjoory et al. \[2017\]](#)). Therefore, to yield an anatomically correct head model, the ICBM152 standard brain template from the Montreal Neurological Institute (MNI), which is a non-linear average of the MR images of 152 individual heads ([Mazziotta et al. \[2001\]](#)), was used in this analysis. Figure 5.2 (a) and (b) demonstrate this MRI in comparison with Colin27 MRI (average of 27 MRIs recorded from one person named Colin) which was used in the

previous chapter. It should be noted that the source model (the solution space) is a separate entity than the head model. While one can use a rather simplistic head model such as the 3-shell spherical model, one can use a more realistic source model in the next step of the inverse solution such as segmented gray matter surface obtained from an averaged brain MRI (Seeland et al. [2018]). While this approach simplifies the calculation of the lead field matrix, it is not very accurate.

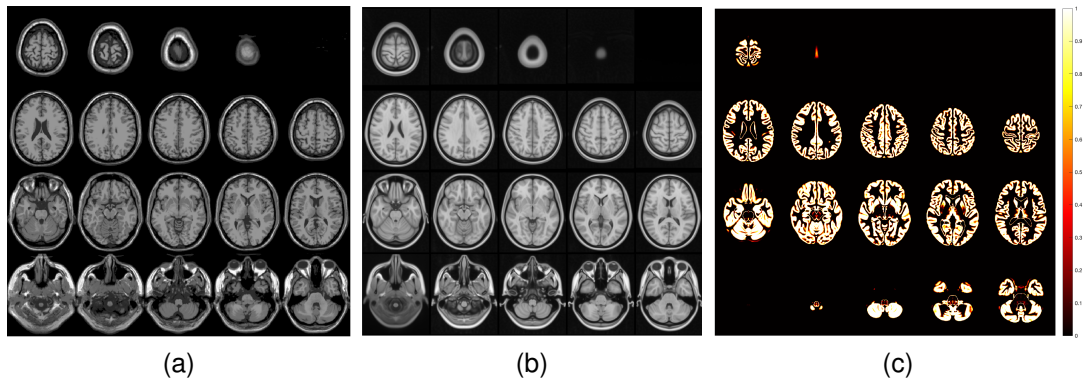


Figure 5.2: Illustration of 2 commonly used averaged MRIs to obtain a realistic head model in source localization studies. (a) Colin27 averaged (b) MRI ICBM152 averaged MRI (c) MRI segmentation and gray matter extraction from ICBM152. Since the ICBM152 image is an average MRI across 152 people, it is a smoother image in comparison to Colin27.

The MRI requires several linear steps of pre-processing in order to obtain proper delineation of various head compartments including the gray matter within which the solution space is usually defined. This includes re-sampling and re-orientation, skull stripping, Bias Field correction, separation of gray and white matter and adjusting the central sagittal plane to ensure the symmetry between the hemispheres. All these steps are performed in SPM12 using a 4×4 affine transform matrix which stacks all these successive steps. The structural MRI is initially segmented into 3 surface layers: Brain, skull and scalp. This can also be performed into 5 layers (white matter, gray matter, cerebral spinal fluid, skull, and scalp (Edelman et al. [2015]) figure 5.2

(c)) which is mostly used for FEM head modeling. Afterwards, three surfaces were created at the borders of each tissue type, represented by points (vertices) connected in a triangular way. 3000, 2000 and 1000 vertices were used to construct brain, skull and scalp surface tissues respectively.

Choice of Head Model and Tissue Conductivity Values:

Regarding the choice of head modeling procedure, two of the often-used realistic electrical models to generate a head model are the boundary element method (BEM) and finite element method (FEM) (Mosher et al. [1999]). The BEM models are composed of overlapping, two-dimensional, triangulated mesh layers (or boundaries), each layer having been computer generated from segmented MRI surfaces. Different compartments are given certain conductivity values and conductivity within each compartment is assumed to be isotropic and homogenous. On the other hand, the FEM models are composed of multiple, three-dimensional, solid tetrahedra, a property that allows conductivity values to vary within each compartment. This means that tissue anisotropy can be factored into algorithms that solve the forward problem. Thus, BEM models can represent major tissue compartments but cannot encode detailed anatomical information within them. In contrast, FEM models can capture more tissue types and the shape of the brain with greater precision than BEM.

While the two types of head models discussed so far are superior to 3-shell spherical models, they are more computationally demanding, and more sensitive to any misshape happening while separating various head compartments. A new standard head model named “ICBM-NY” or “New York Head” has been proposed (Huang et al. [2016]), which is a high precision FEM head model based on ICBM 152 MRI. Due to the comparisons conducted in this study, the EEG source localization error

for ICBM BEM and ICBM FEM head models are very close. Thus, here, the volume conduction model was constructed using the dipoli method (an implementation of BEM by Thom Oostendorp) in FieldTrip with conductivities of the scalp, skull and brain set to 0.33, 0.33/30 and 0.33, respectively. It was previously assumed that the resistivity ratio between the brain and the skull is 1:80 and thereby, the default conductivity parameter for skull is 0.33/80 in FieldTrip toolbox. However, it has been shown that the skull resistivity is much lower (around 1:10 to 1:30 depending on age) ([Michel and Brunet \[2019\]](#)). Thus, as the age range of participants in this study was between 20-30, the ratio was set to 1:30.

Electrode 3D Positions:

The 3D electrode positions should correspond to the actual positions of the sensors on the head during the recording. As the electrodes were positioned at standard 10-20 sites, the standard 10-20 electrode locations file by [Oostenveld and Praamstra \[2001\]](#) represented in mm in the MNI coordinate system was used here. The 3D electrode array should be co-registered on the MRI head model which can be done interactively or only by relying on fiducial positions. All geometrical descriptions of all elements (channel positions, head model and source model) should be registered in the same coordinate system with the same units. This might be challenging since the head and source model are based on MRI and are initially expressed in the scanner's coordinate system whereas the sensor descriptions are based on another. All these objects were mapped to MNI coordinates and co-registered. [Figure 5.3](#) illustrates the above mentioned steps in generating the head model.

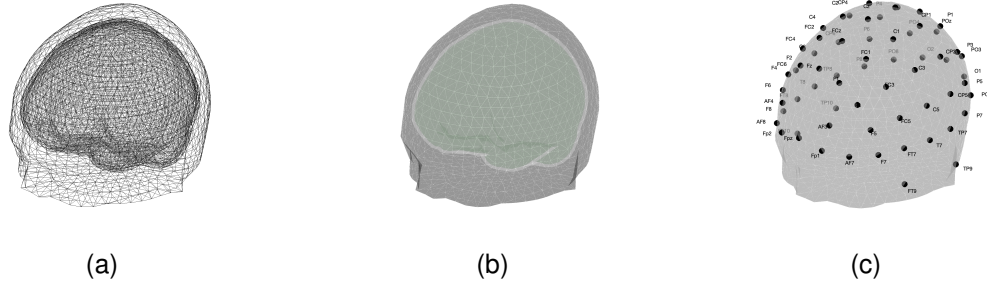


Figure 5.3: Illustration of different steps of head model construction. (a) Three surface meshes obtained from ICBM152 average MRI segmentation. (b) head model geometry; notice that the brain surface is smoothed. (c) 64 Electrode position alignment on the scalp.

Source Model Definition:

The source model describes a set of positions (and possibly orientations) of equivalent current dipoles that are taken into consideration when doing the source reconstruction. In FieldTrip, distributed source modeling and scanning methods require pre-specification of a source model while other methods like dipole fitting do not. A source model can be defined on a 3-dimensional grid which is referred to as a volumetric source model (can be restricted to the gray matter) or on a 2-dimensional surface (typically the cortical sheet). Here, a 3D grid with the resolution of 1cm was constructed as depicted in figure 5.4. Essentially, this grid is a cubic grid (of dimensions $[14 \times 18 \times 14]$ including 3528 total points) where the points inside the brain volume specified by the head model were used as source points (1819 source points). An inward shift of 5mm was applied on the sources as BEM models can be unstable close to the border.

Leadfield Computation:

For every source in the source model, the leadfield is obtained by computing the electric potential measured at all electrodes given the relevant source has an activation of 1 Am. Lead field normalization is necessary in order to rectify the depth bias. The

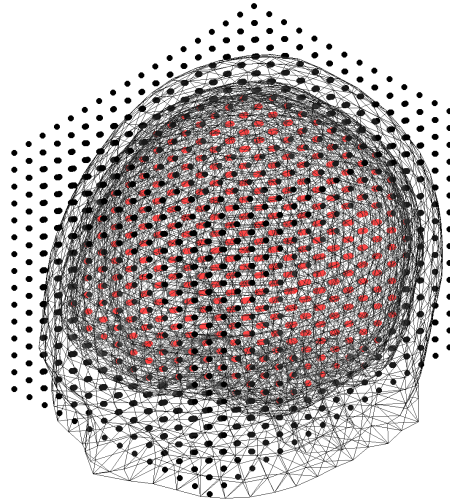


Figure 5.4: Illustration of the head model overlain with the volume grid and source model. The source model consists of the source points inside the brain volume which are specified with red colour.

lead field matrix was normalized by the sum of squares of the elements of the matrix to the power of the depth normalization parameter which was set to 1 here after inspecting the leadfield. In order to inspect the lead field, a realistic source current of 100 nAm was projected onto the scalp through the lead field and plotted on the scalp mesh alongside the electrode. Figure 5.5 shows that the topography of the scalp field is reasonable and smooth and the electric potentials are in the expected range (microvolts).

Inverse Solution: LCMV Beamformer Specification

The LCMV beamformer as an adaptive spatial filter depends on the estimation of the data covariance matrix and its inverse. An inverse may not exist if its computation can be numerically unstable, which occurs if the covariance matrix is close to singular (has a very large condition number comparable to $(machineepsilon)^{-1}$). When dealing with such under-determined systems of equations for inversion, Tikhonov

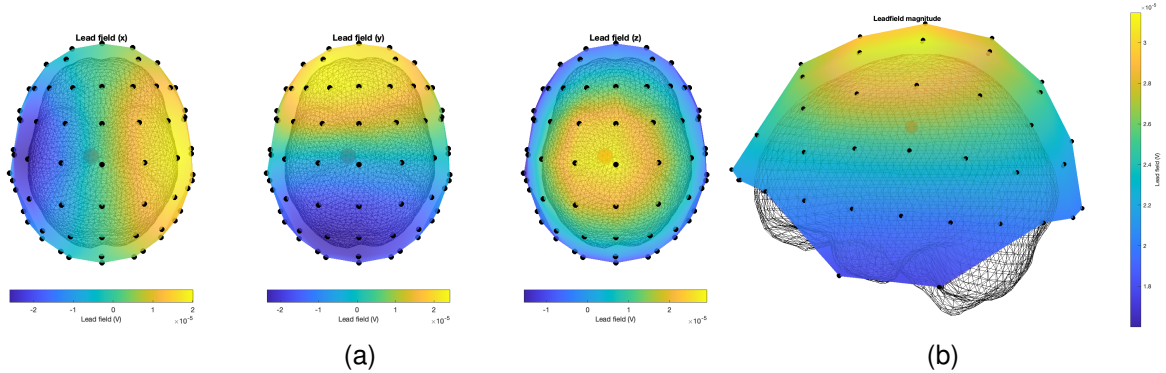


Figure 5.5: (a) Lead fields in the XYZ directions for the ICBM152 BEM head model for a superficial source. (b) Magnitude of the lead fields for the ICBM152 BEM head model for a superficial source.

regularization is often employed which introduces a degree of EEG noise into the calculations and ensures smoothness in the inverted result. Tikhonov regularization follows the idea of diagonal loading via increasing the diagonals of the covariance matrix by a pre-specified amount. This is done by replacing C^{-1} with $(C + \lambda I)^{-1}$. The higher the regularization, the smoother the outcomes and the lower the noise sensitivity. The goal is to avoid over-smoothing to obtain the most accurate results.

The noise level is not known and it is difficult to give a quantitative estimate of lambda, therefore a relative measure based on the maximum or average eigenvalue of the covariance matrix can be defined. After testing different values of λ including 0.001, 0.01, 1 and 10% on the present data, the regularization parameter was set to 0.001% of the average eigenvalue of the covariance matrix. Additionally, the source orientations are not predetermined and the optimal source orientation is estimated so that the spatial filter output is maximized. The orientations were assumed to be fixed throughout the course of the trial. Figure 5.6 demonstrates an example of the source activity map for 4 time points during performance of mental subtraction imagery for subject D.

to represent the time and frequency content carried by hundreds of dipoles with diverging orientations in each ROI with one unique representative time-series ([Rubega et al. \[2019\]](#)). In the following section, we discuss these two issues in more detail and lay out the various setups investigated in this study.

ROI Configuration:

To define ROIs, many anatomical and/or functional atlases are available. Here, to cover both volumetric and superficial source clusters separately, two widely-used atlases were used to define 3 configurations of ROIs: 1) 74 Brodmann ROIs, 2) 26 coarse cortical ROIs and 3) 16 coarse volume ROIs that included both cortical and deeper brain structures. Firstly, Brodmann areas were used to create 74 contralateral ROI pairs (figure 5.7). Second, these regions were further combined together to form 26 coarse ROIs (figure 5.8) covering the surface of the brain. Brodmann areas (BAs) are essentially defined in term of the atlas of Talairach and Tournoux ([Brodmann \[1909\]](#)). This can be problematic, as the brains in the Talairach atlas and MNI template differ significantly in shape and size. As a result the MNI brains are slightly larger (in particular higher, deeper and longer) than the Talairach brain. The differences are larger as you get further from the middle of the brain, towards the outside, and are at maximum in the order of 10mm ([Brett et al. \[2001\]](#)). Thus, when choosing the atlas it is very important to note this difference and use already transformed atlases to MNI space.

BA-based ROIs were obtained by WFU PickAtlas provided by Wake Forest University, school of medicine ([Maldjian et al. \[2003\]](#)). WFU PickAtlas provides a method for generating ROI masks based on the Talairach Daemon database in MNI space.

Third, the Automated Anatomical Labelling (AAL) atlas ([Tzourio-Mazoyer et al. \[2002\]](#)) was utilized to produce another set of 16 coarse anatomically labelled ROIs (figure 5.9). This atlas contains 116 anatomical regions and is specified in the MNI coordinate space. Similar to BAs, in order to reduce the dimensionality, regions of the atlas were grouped into coarse regions for both left and right hemispheres. The gross regions considered are: prefrontal cortex, motor cortex, basal ganglia, insula, parietal cortex, temporal cortex, occipital cortex, limbic regions, cerebellum as well as an additional medial cerebellum region. While the cortical ROI configuration was defined based on our knowledge of cognitive neuroscience, the volumetric ROI configuration is adapted from ([Chrapka \[2018\]](#)).

ROI Representative Time-Series:

Additionally, the activity of all the source points in an ROI should be summed up into one representative waveform for further analysis. The main aim is to compute a signal that explains most of the variability of the data contained in each ROI before computing features. Various methods have been explored in previous studies, mostly inspired from fMRI analysis methods and they depend on whether the dipoles' orientations were assumed to be fixed during the trial interval ([Rubega et al. \[2019\]](#)). Some of these methods are introduced and utilized in the following sections.

For example, averaging the activity in each ROI is a simple and popular way to obtain a single time-series representative of the activity of a given extended brain source (ROI) ([Astolfi et al. \[2007\]](#), [Hassan et al. \[2017\]](#)). Since the cortex is folded, in order to avoid activity cancellation due to the opposite direction of the dipole sources, the averaging can be performed on the absolute value of the dipole moments which is a bit anecdotal ([Hassan and Wendling \[2018\]](#)).

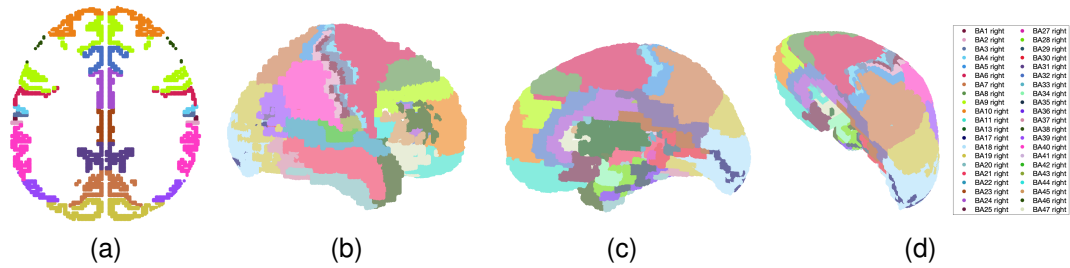


Figure 5.7: A parcellation of the cortex superficial grid into 74 Brodmann areas (BA). Each color represents an ROI on the ICBM152 BEM head model. a) Axial view b) Lateral view of the right hemisphere c) Medial view the right hemisphere d) A view from above.

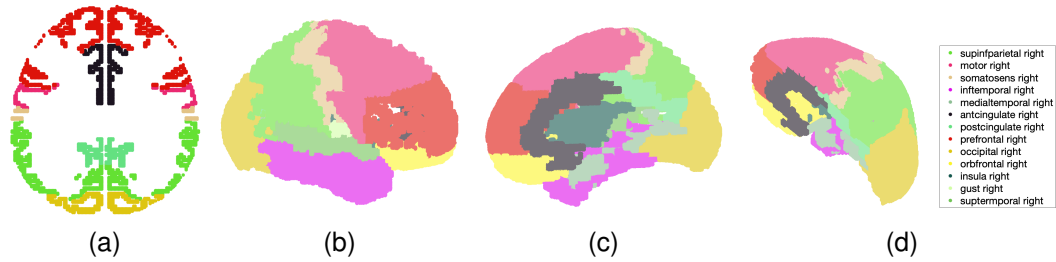


Figure 5.8: A parcellation of the cortex superficial grid into 26 coarse BAs. Each color represents an ROI on the ICBM152 BEM head model. The grouping of BAs is as follows: 1) BAs 7,39,40 - superior and inferior parietal association areas, 2) BAs 2,3,5 - somatosensory areas, 3) BAs 4,6,8 - motor areas, 4) BAs 20,21,37,38 - inferior temporal areas, 5) BAs 26,27,28,29,30,34 - medial temporal lobe (MTL memory system), 6) BAs 24,25,32,33 - anterior cingulate, 7) BAs 23,31 - posterior cingulate, 8) BAs 9,10,44,45,46 - prefrontal area, 9) BAs 17, 18,19 - occipital area, 10) BA 13 - insula, 11) BAs 11,12,47 - orbitofrontal areas, 12) BA 43 - primary gustatory, 13) BAs 22,42,42 - superior temporal gyrus. a) Axial view b) Lateral view of the right hemisphere c) Medial view the right hemisphere d) A view from above.

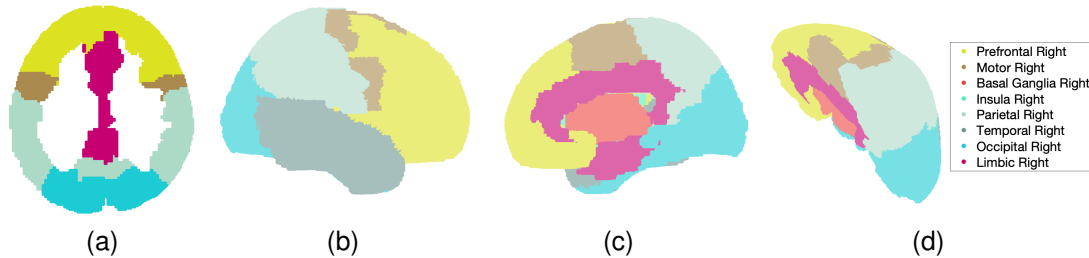


Figure 5.9: A parcellation of the brain volume into 16 coarse AAL regions (Chrapka [2018]). Each color represents an ROI on the ICBM152 BEM head model. The gross regions considered are: prefrontal cortex, motor cortex, basal ganglia, insula, parietal cortex, temporal cortex, occipital cortex, limbic regions (Hippocampus, parahippocampal region, Amygdala, Cingulum anterior, medial and posterior), cerebellum as well as an additional medial cerebellum region. a) Axial view b) Lateral view of the right hemisphere c) Medial view the right hemisphere d) A view from above.

As a result of activity cancellation in the case of simple averaging, a drastic amplitude reduction will be inevitable which might affect the subsequent analysis steps.

Nevertheless, this is the most widely used approach in regional source reconstruction. As another approach, the solution point closest to the geometric center (centroid) of the ROI can be used as the representation of the region’s activity (Coito et al. [2015]). Additionally, the peak of activity within an anatomical ROI, the dipole with the highest power (i.e. the mean squared amplitude) can be selected. It should be noted that selection of one single source point does not necessarily adequately represent the ROI activity as a whole.

For example, averaging the activity in each ROI is a simple and popular way to obtain a single time-series representative of the activity of a given extended brain source (ROI) (Astolfi et al. [2007], Hassan et al. [2017]). Since the cortex is folded, in order to avoid activity cancellation due to the opposite direction of the dipole sources, the averaging can be performed on the absolute value of the dipole moments which is a bit anecdotal (Hassan and Wendling [2018]). As a result of activity cancelation in the case of simple averaging, a drastic amplitude reduction will be inevitable which might affect the subsequent analysis steps. Nevertheless, this is the most widely used approach in regional source reconstruction. As another approach, the solution point closest to the geometric center (centroid) of the ROI can be used as the representation of the region’s activity (Coito et al. [2015]). Additionally, the peak of activity within an anatomical ROI, the dipole with the highest power (i.e. the mean squared amplitude) can be selected. It should be noted that selection of one single source point does not necessarily adequately represent the ROI activity as a whole.

More advanced statistical approaches have been proposed and used in a limited number of studies. In one study, a dimensionality reduction technique, principal component analysis (PCA), was utilized on all the sources in a region and selected

the dominant principal component as the ROI waveform (Dimitriadis et al. [2018]). Another study proposed to use the first singular vector computed by a singular-value decomposition (SVD) of all dipoles belonging to the same ROI to extract the dominant signal reflecting the main pattern of variation of all solution points (Rubega et al. [2019]).

Unfortunately, to the author’s knowledge, there is no study in the literature which compares and reports the effect of representative ROI time series on further analysis steps, even in functional brain networks analysis in source space in which this issue has been attended to (Dimitriadis et al. [2018])). Thus, a number of strategies were investigated and compared in this study which are summarized in table 5.1.

Table 5.1: Methods of representative waveform calculation for every ROI compared in this thesis.

ROI Representative	Description
Average	Instantaneous average of the signed magnitude of all dipoles within an ROI during the entire imagery interval (Astolfi et al. [2007]).
Absolute Average	Instantaneous average of the absolute magnitude of all dipoles within an ROI during the entire imagery interval (Hassan and Wendling [2018]).
Source with Maximum Power	The activity of the dipole with the highest power (i.e. the mean squared amplitude).
First Principal Component	PCA of all solution points and select the first one (Dimitriadis et al. [2018]).
First Singular Vector	SVD of all dipoles belonging to the same ROI and select the first singular vector (Rubega et al. [2019]).

5.3.2 Feature Extraction

Once the regional time-series were obtained, a set of candidate features were extracted including power spectral density (PSD) of every ROI time-course and magnitude coherence and phase lag index (PLI) between all pairs of ROI time-courses. PSD was calculated using `cpsd` and magnitude-squared coherence was estimated using `mscoher` MATLAB built-in functions. The spectrum estimation in these functions is based on the modified Welch periodogram method (Welch [1967]). These values were computed over the frequency band of [1-30] Hz with 1 Hz increments. The length of the Hamming window and the number of overlapping samples were set to F_s and $F_s/2$ respectively (where F_s is 500 Hz) to avoid spectral over-smoothing. A total of $30 \times ROI_n + 30 \times \binom{ROI_n}{2} + \binom{ROI_n}{2}$ features was computed for each trial where ROI_n is the number of ROIs.

5.3.3 Feature Selection and Classification

Features were standardized and feature selection was performed using the mRMR method before SVM classification. A grid search procedure was exploited to find the optimal number of features selected by mRMR ([1:50]) as well as the kernel type (linear or RBF), margin ([1:10]) and kernel scale ([1:10]) for the SVM classifier. The performance of the binary classification of EEG data generated during each pair of mental imagery tasks was evaluated using a 100-fold cross-validation with 95% train and 5% test split per subject and the best accuracy is reported in the results section. The random number generator seed was set to 0 for reproducibility of the results. Figure 5.10 summarizes the final BCI pipeline used for data processing.

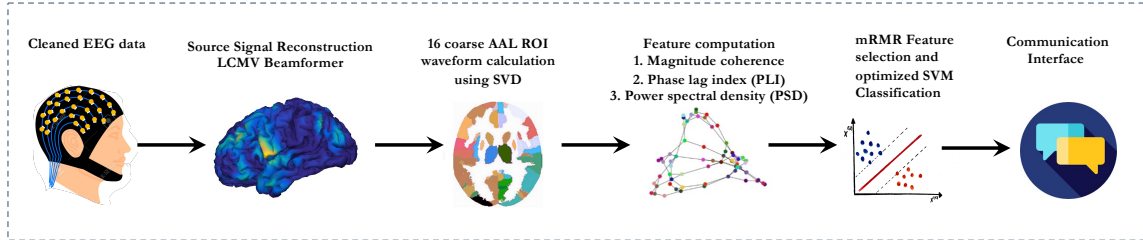


Figure 5.10: Final BCI Pipeline Diagram.

5.4 Results

The results are presented in three sections. Firstly, comparisons of various ROI configurations and regional time-series computation methods were assessed on one subject, on one pair of tasks. Additionally, all pairwise classifications between mental imagery tasks are reported for 13 subjects. Finally, the performances of the top pairs are reported for all subjects in a bar plot for visual comparison.

5.4.1 Various ROI Configurations Comparison

In order to identify the most effective ROI configuration and regional time-series computation methods, all the mentioned approaches were compared in one case of mental imagery classification in one subject. 3 ROI setups and 5 ROI waveform extraction procedures were utilized in classification of song and subtraction imagery tasks. The results presented in table 5.2 indicate the best performance of 84.07% is achieved when using 16 coarse AAL areas as the ROI configuration, and using the first singular vector as the ROI representative time-series.

Table 5.2: Comparison of ROI configuration and regional time-series computation method on subject J, song vs. subtraction.

ROI Configuration	73 Brodmann Areas	26 Coarse Cortical Areas	16 Coarse AAL Areas
Average	68.70	79.16	69.37
Absolute Average	62.05	63.21	65.98
Source with Maximum Power	65.50	71.10	57.23
1st Principal Component	59.92	68.33	76.85
1st Singular Vector	72.23	70.25	84.07
Total Feature No.	83658	10855	4200

5.4.2 Mental Imageries Pairwise Classification

All pairwise classification performances between the 7 mental imagery tasks (including 6 active tasks and rest) for all 13 participants are reported in tables 5.3 through 5.15. The most distinctive combination of tasks are highlighted in green for each subject. While several subjects, including B, H and M had fewer task combinations which were classifiable (tables 5.4, 5.10, 5.15), others had more combinations of separable tasks. The best pair of tasks were decodable with an average of 82.86% accuracy across all 13 participants, and all 13 participants had at least one pair of tasks that could be decoded with at least 70% accuracy.

Table 5.3: Pairwise classification of mental imageries for subject A

MI	Sport	Nav	Song	Sub	Fing	Run
Relax	71.50	72.33	60.00	68.25	64.00	59.62
Sport	-	62.43	73.50	72.33	66.20	68.00
Nav	-	-	75.50	79.20	65.33	67.00
Song	-	-	-	73.00	66.87	74.20
Sub	-	-	-	-	60.40	68.17
Fing	-	-	-	-	-	65.25

Table 5.4: Pairwise classification of mental imageries for subject B

MI	Sport	Nav	Song	Sub	Fing	Run
Relax	70.44	63.12	50.42	56.66	71.00	61.62
Sport	-	65.66	56.85	60.11	63.35	55.87
Nav	-	-	61.00	61.44	61.77	52.87
Song	-	-	-	86.12	73.14	68.03
Sub	-	-	-	-	62.27	52.75
Fing	-	-	-	-	-	59.00

Table 5.5: Pairwise classification of mental imageries for subject C

MI	Sport	Nav	Song	Sub	Fing	Run
Relax	56.67	65.28	54.00	62.4	65.50	53.38
Sport	-	60.50	56.12	64.49	80.40	61.33
Nav	-	-	61.03	70.33	83.34	63.00
Song	-	-	-	60.66	74.50	56.37
Sub	-	-	-	-	79.25	74.00
Fing	-	-	-	-	-	76.87

Table 5.6: Pairwise classification of mental imageries for subject D

MI	Sport	Nav	Song	Sub	Fing	Run
Relax	69.33	79.50	62.66	71.27	70.25	67.50
Sport	-	57.83	63.71	61.50	53.33	54.33
Nav	-	-	79.50	85.10	63.82	61.00
Song	-	-	-	56.00	56.34	63.83
Sub	-	-	-	-	65.28	63.60
Fing	-	-	-	-	-	55.60

Table 5.7: Pairwise classification of mental imageries for subject E

MI	Sport	Nav	Song	Sub	Fing	Run
Relax	83.50	76.27	72.44	75.50	81.00	70.33
Sport	-	85.25	91.07	87.66	85.28	87.50
Nav	-	-	60.87	65.71	62.55	54.83
Song	-	-	-	69.00	48.60	49.82
Sub	-	-	-	-	66.28	51.25
Fing	-	-	-	-	-	46.83

Table 5.8: Pairwise classification of mental imageries for subject F

MI	Sport	Nav	Song	Sub	Fing	Run
Relax	82.25	79.20	75.60	87.00	79.43	72.03
Sport	-	70.50	86.75	73.66	53.87	70.50
Nav	-	-	88.44	78.71	73.11	80.89
Song	-	-	-	83.42	79.56	68.00
Sub	-	-	-	-	69.57	78.14
Fing	-	-	-	-	-	70.00

Table 5.9: Pairwise classification of mental imageries for subject G

MI	Sport	Nav	Song	Sub	Fing	Run
Relax	72.28	72.00	53.56	53.74	56.85	60.25
Sport	-	58.33	64.60	52.62	53.77	54.85
Nav	-	-	66.00	63.25	73.11	87.90
Song	-	-	-	82.75	51.80	60.00
Sub	-	-	-	-	65.37	63.50
Fing	-	-	-	-	-	63.14

Table 5.10: Pairwise classification of mental imageries for subject H

MI	Sport	Nav	Song	Sub	Fing	Run
Relax	65.20	58.66	63.67	65.00	66.25	62.80
Sport	-	55.71	69.50	69.28	60.37	54.00
Nav	-	-	77.04	58.25	58.33	53.87
Song	-	-	-	83.50	61.25	56.50
Sub	-	-	-	-	60.16	69.71
Fing	-	-	-	-	-	52.12

Table 5.11: Pairwise classification of mental imageries for subject I

MI	Sport	Nav	Song	Sub	Fing	Run
Relax	52.33	70.50	69.83	55.20	61.83	51.20
Sport	-	60.28	52.22	56.00	59.34	51.87
Nav	-	-	61.14	67.42	51.57	58.66
Song	-	-	-	50.88	65.77	59.87
Sub	-	-	-	-	55.34	55.12
Fing	-	-	-	-	-	56.25

Table 5.12: Pairwise classification of mental imageries for subject J

MI	Sport	Nav	Song	Sub	Fing	Run
Relax	65.66	69.01	71.50	90.00	56.50	56.25
Sport	-	58.34	77.52	77.40	75.54	63.50
Nav	-	-	68.23	78.76	69.04	70.37
Song	-	-	-	76.51	84.07	67.43
Sub	-	-	-	-	80.76	67.00
Fing	-	-	-	-	-	64.66

Table 5.13: Pairwise classification of mental imageries for subject K

MI	Sport	Nav	Song	Sub	Fing	Run
Relax	69.55	67.14	66.66	71.56	56.22	56.89
Sport	-	55.42	56.00	77.50	59.55	53.33
Nav	-	-	62.42	67.59	62.42	78.14
Song	-	-	-	64.66	60.77	62.22
Sub	-	-	-	-	66.87	56.66
Fing	-	-	-	-	-	60.75

Table 5.14: Pairwise classification of mental imageries for subject L

MI	Sport	Nav	Song	Sub	Fing	Run
Relax	63.33	74.25	69.66	60.00	58.60	62.50
Sport	-	73.25	65.87	65.66	61.53	61.47
Nav	-	-	54.95	56.05	80.33	70.73
Song	-	-	-	58.25	59.66	63.25
Sub	-	-	-	-	65.75	65.40
Fing	-	-	-	-	-	67.50

Table 5.15: Pairwise classification of mental imageries for subject M

MI	Sport	Nav	Song	Sub	Fing	Run
Relax	56.62	59.37	64.44	50.50	58.77	65.87
Sport	-	62.00	50.12	73.28	53.50	57.83
Nav	-	-	56.62	43.80	49.08	83.95
Song	-	-	-	63.16	58.22	57.42
Sub	-	-	-	-	57.50	58.75
Fing	-	-	-	-	-	62.42

5.4.3 Best Separable Pairs of Task for Each Subject

In order to summarize the results across participants, the three most separable pairs of tasks for every subject are identified and the performances are ranked and illustrated in figure 5.11. These pairs were previously highlighted in green in tables 5.3 to 5.15. All subjects, expect for subject I, had a pair of tasks that were classifiable with almost or over 80% accuracy, while for subject I, the classification of the best pair of tasks achieved 70.5% accuracy, as can be seen in Figure 5.11.

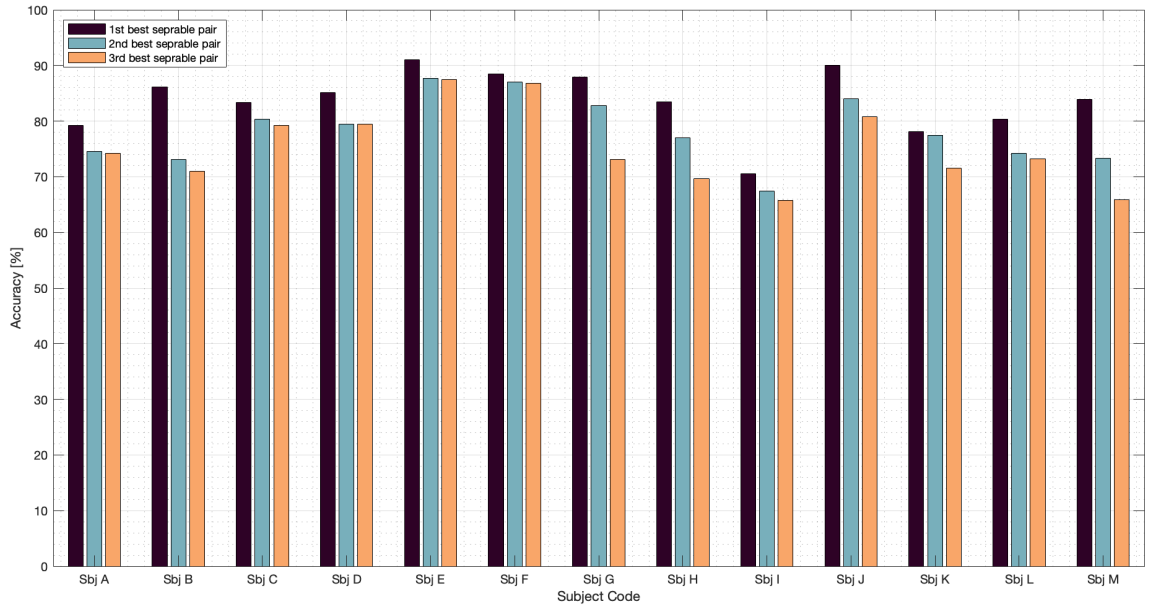


Figure 5.11: Three best separable pairs of tasks for all participants.

5.5 Discussion

The present study investigated an expanded set of mental imagery tasks in healthy individuals, for the purpose of determining whether a subject-specific combination of highly classifiable tasks are detectable using beamforming. Additionally, several ROI

configurations as well as multiple methods for ROI representative time-series calculation were explored. It has been shown, using spectral and connectivity features at source level, that at least two pairs of mental commands can be discerned which are significantly more classifiable than other tasks for the subject. The best separable mental tasks achieved accuracies comparable to the accuracies of the standard tasks, left versus right hand motor imagery (Saha et al. [2019]), and thus can be considered well-suited for BCI control. Furthermore, in most BCI studies, around 30% of participants fail to achieve a binary classification accuracy above 70% (the so-called BCI illiteracy problem) whereas here we have shown that if participants are permitted to use their most separable pair of tasks, 12 out of 13 (7%) participants can achieve a high separation accuracy of greater than 80%, while the remaining participant's highest accuracy was still above 70%. Thus, employing a wide range of imagery tasks and choosing the two most separable for each individual participant is shown to be a promising way of solving the BCI illiteracy problem. The high variability between the best task combination across participants suggested that an individually tuning BCI control signals could enhance BCI user-friendliness and performance.

The BCI performance is influenced by the choice of the algorithm for estimating the source waveforms and the brain parcellation setup. According to the results reported in table 5.2, using 16 coarse AAL ROIs yields the best performance among all ROI setups, at least for this one participant. (However, it would be important to explore whether this same choice of AAL ROIs is best for all other participants). This could be due to the location and extent of defined regions of activity. As demonstrated in figures 5.7, 5.8 and 5.9, subfigures (a), Brodmann areas only cover the cortex while the AAL patches include both cortical and sub-cortical regions, thereby providing

greater coverage of the brain volume. In the case of motor imagery, as repeatedly shown by previous studies, the activity is expected at the primary motor cortex (Zaitcev et al. [2019]), which is located along a strip just anterior to the central sulcus on the cerebral cortex. Hence, using BA ROIs was reasonable and sufficient in decoding motor imagery as shown in the last chapter. However, the origins of other mental imagery activity could go deeper into the gray matter and deeper brain regions beneath the cerebral cortex, and restricting the ROIs to the cortex is not adequately enclosing the active areas. As evidence for deeper activation patterns, an fMRI study showed the brain activation of the supplementary motor area (SMA) during tennis imagery, and the parahippocampal gyrus (PPA), posterior parietal lobe (PPC), and lateral premotor cortex (PMC) during imagery of spatial navigation (Sinai et al. [2017]). An additional reason for AAL ROIs to be a more suitable configuration could be the inevitable localization error due to the intrinsic limitation of inverse solutions as well as using a generic head model which would require considering wider ROIs. Therefore, coarse AAL ROIS were used in obtaining the final results for all participants.

In terms of the method of regional waveform calculation, our results indicate that using the first singular vector results in the best performance. Despite previous findings (Hassan et al. [2017]), in our analyses the absolute average of the ROI time-series had the worst performance followed by the source with maximum power. Instead of choosing one single source time series (maximum power), the method based on singular value decomposition sums up the information carried by time-series in a unique 1-D signal representing most of the variability of the sources in each region of interest.

Due to the orthogonality constraints (U and V are orthogonal matrices and S is a diagonal matrix), the solution of SVD is unique and can be considered a reliable method for dimensionality reduction. The amplitude of the representative signal computed as the first orthonormal vector of the unitary matrix U is by definition independent of the original signal amplitudes. Thus, this solution overcomes a major drawback of the common procedure of averaging the dipoles, namely drastically reduced amplitudes after averaging all the dipoles in the same region of interest. Dealing with smaller amplitudes may distort the results of the connectivity estimation because it involves computing of the inverse of the matrix containing the data ([Rubega et al. \[2019\]](#)).

Additionally, both SVD and PCA methods exploit the information of the overall population of dipoles in each ROI instead of considering only one time-series as representative of the complex activity pattern in a given brain region. However, in the present data, SVD appears to provide a more informative regional time-series than PCA. This could be due to the fundamental difference between these two procedures. Essentially, SVD untangles the data into independent components in the directions with the highest variances respectively. Additionally, PCA is a statistical procedure that uses an orthogonal transformation to convert a set of observations of possibly correlated variables into a set of values of linearly uncorrelated variables called principal components ([Friedman et al. \[2001\]](#)). While PCA can be performed using SVD by truncating the less important basis vectors in the original SVD matrix, it ignores the least significant components in reconstructing the data by only using the principal directions with the highest variances. Therefore, by taking into account all the components, SVD yields a more promising way of obtaining regional time-series.

Furthermore, the presented results should be compared with other studies to situate the findings in the field. In a similar study, the most separable mental states based on functional network measures at the cortical level has been identified ([Besserve et al. \[2011\]](#)). 10000 sources from single trial EEG signals were reconstructed using MNE. The spectral power of every current dipole in 5 frequency bands in addition to coherence features calculated between pairs of 82 Brodmann areas in the same 5 frequency bands comprised the feature vectors of size 70000. The list of mental tasks used included three motor imagery tasks (imagination of grasping an object with the right hand, right index finger movement imagination, tongue movement imagination) and three non-motor tasks (visuospatial navigation, auditory music imagination and mental calculation). An average best accuracy of 86.79% was achieved across 5 healthy subjects. These results show that reconstructing the underlying cortical network dynamics significantly outperforms a usual electrode level approach in terms of information transfer and also reduces redundancy between coherence and power features. However, the proposed BCI pipeline in this thesis follows a more sparse feature space calculation (4,200 compared to 70,000) yet achieves a similar level of performance, meaning significantly lower computational complexity. This indicates that beamforming might be a better source reconstruction approach compared to MNE in quantification of functional networks and decoding mental states.

Another study investigated EEG patterns that were induced by seven different mental tasks (i.e. mental rotation, word association, auditory imagery, mental subtraction, spatial navigation, imagery of familiar faces and motor imagery) and evaluated the performance of a binary LDA classifier on CSP features computed on band-passed [8-30]Hz EEG data ([Friedrich et al. \[2012\]](#)). The evaluation on 1s long trials

with 0.5s overlap indicated eight out of nine users reached classification accuracies more than 95%. However, using overlapped trials essentially causes leakage of information from the training set to the test set, meaning that there is information in the test data that has already been seen by the train model. This results in overestimated accuracies. In this thesis, trials had no overlap and lower accuracies are expected.

In conclusion, this study confirms that using beamforming provides a computationally efficient and interpretable strategy to extract distinctive information from functional networks at the cortical and sub-cortical level in single trials supporting a decrease of volume conduction effects. Moreover, this sets a general framework to evaluate the performance of EEG source reconstruction methods by their decoding abilities. The aim was to provide a broad range of reliable and user-appropriate tasks to make individual optimization of BCI control strategies possible. The results indicate the best separable tasks, with an average accuracy of 82.86% across all participants, are identifiable with as low as 70 trials per condition. By collecting more trials, a more tuned model is possible to train for each subject leading to better performance. Therefore, using a combination of connectivity and spectral measures of active sources underlying EEG data represents a promising choice for future online BCI implementations.

5.6 Limitations of the Study

Two concerns should be discussed in relation to the presented results. The first concern is that, since in this dataset each imagery trial was split into 4 segments, the non-independence of these segments should be controlled for during cross-validation. This way of partitioning train/test data was based on the conventional approaches in

previous studies on mental imagery classification, including the ones which were compared with the results in this chapter ([Besserve et al. \[2011\]](#), [Friedrich et al. \[2012\]](#)), as well as the main paper published on the analyses dataset ([Harrison et al. \[2017\]](#), [Harrison \[2014\]](#)). However, lack of independence between the trials in the test set and train set leads to a leakage of information. Typically intra-trial correlation is quite high compared to inter-trial correlation, so having each trial partially represented in both the training and test sets, even though they are non-overlapping segments of a trial, could inflate classification performance. It is not expected that correcting this would completely change the classification performance. This correction has been implemented and tested for one subject. The LOOCV results indicate that for subject F, where the best pair of tasks (song and navigation MI) were previously separable with 88.44% accuracy, are classifiable with 90.28%. The inflation of accuracy is due to using only one sample for test. However, this indicates that controlling for within-trial correlations by selecting training and segments from separate trials will likely not substantially deteriorate the results.

The second concern is that, when using grid search for model selection prior to classification, we should have a nested cross-validation loop with training sets, validation sets, and test sets. However, in the analyses reported here, a single cross-validation loop was used both to select hyper-parameters and assess generalization performance. Thus, we were evaluating the model selection process (hyperparameter turning) on the test set simultaneously with model performance (training the selected model). This could lead to overfitting by model selection (or hyperparameter tuning). This applies to feature selection as well. Basically the machine learning pipeline

does not need to select for model hyperparameters or the feature subset that maximizes generalizability to unseen data. Instead, it can just choose the configuration that maximizes test set performance, which is somewhat analogous to p-hacking in multivariate statistics. This limitation should be addressed in future works.

Chapter 6

Discussion, Conclusions and Future Directions

6.1 Discussion and Conclusion

BCIs have been previously used for the control of neuroprostheses, speller systems, and systems for motor impairments ([Hwang et al. \[2013\]](#), [Bansal and Mahajan \[2019\]](#)). As a long-coveted application of BCI, decoding covert speech by means of EEG, MEG and a combination of both modalities has been explored by researchers in the past decades. Although using speech imagery is more intuitive and better matches the intention of the device, it has been shown to be very challenging to decode various words from EEG ([Vansteensel and Jarosiewicz \[2020\]](#)). Therefore, in this study, a framework for a communication BCI based on mental imagery decoding was proposed using 1) a beamforming source localization method in EEG signal processing, and 2) a wide range of different imagery tasks, so that the two most separable tasks can be selected for each individual, allowing personalization of the BCI. Conventional

BCI studies typically prescribe the use of only two different tasks and the signal analysis and classification is performed at the sensor level. The present study was performed to investigate the effectiveness of beamforming as a source localization method, in combination with multiple imagery tasks, to assess the performance of mental imagery based-BCIs for communication. The novelty of this BCI study is in employment of source imaging methods as well as the diversity of mental imagery tasks. Thus, the impact of task freedom on BCI illiteracy, by selecting the two most separable imagery tasks from a list of 6 unique tasks, has been investigated here.

The effectiveness of using a beamformer as a source localization method has been shown on two different datasets in this thesis. As stated by [Michel and Brunet \[2019\]](#), p.1, “High-density EEG systems combined with precise information of the head anatomy and sophisticated source localization algorithms now exist that convert the EEG to a true neuroimaging modality”. These methods improve SNR by compensating for the volume conduction effect, increasing interpretability of the underlying activity by localizing the origins of activity, and they can be a useful dimension reduction method, mapping numerous electrode signals into less than 20 source time-series. Despite all these desirable attributes, the shortcomings of the ESI methods should be discussed and considered. Firstly, EEG captures a mixture of activity from millions of neurons spatially oriented in various directions and the majority of the activity is therefore canceled while received at the scalp. Hence, the EEG measurements are already a vague representation of the underlying activity. Secondly, as the inverse problem is an ill-posed problem in nature, various assumptions and constraints must be applied to obtain a unique solution and there is no systematic way to select the most appropriate ESI method for a certain recording. “It must be made very clear

that no matter how sophisticated these assumptions and constraints are, the provided source solution remains an estimation that depends on how well genuine sources conform to these assumptions” (Michel and Brunet [2019], p.2). The judgment call is for the researcher to make and therefore, investigating the suitability of the ESI method’s constraints and assumption in the context of the specific experimental paradigm is crucial.

Moreover, it cannot be emphasized enough that source imaging involves numerous analysis steps with plenty of detail in every step, while ignoring any one of them can immensely and adversely impact the results. Every computational mistake in any of the steps will propagate and intensify throughout the succeeding steps. Thus, every step should be done with caution to obtain reliable results. Additionally, it has to be kept in mind that there are numerous simplifications in every step of this type of modeling. For instance, in the forward problem, despite all the advancements in generating a realistic head model, all these sophisticated methods are still a naïve simplification of the complex brain and head organization. Therefore, these methods should be applied with caution and the results should be interpreted with the above mentioned facts in mind.

While the proposed BCI pipeline can improve BCI illiteracy and has promising performance, it relies on certain ad hoc assumptions and constraints that can influence the accuracy of the results. The first assumptions are embedded in the beamforming source localization method used to solve the inverse problem and the second constraint lies in the definition of the regions of interest in the parcellation of the brain and the calculation of regional ROIs. In conclusion, the current study showed the possibility of using a source space BCI based framework based on active mental imagery tasks

and increased options for more diverse, personalized, mental imagery BCIs. There is a pronounced need for non-motor imagery based BCIs for individuals suffering from stroke, spinal cord injury, and congenital motor disorders, for whom motor imagery can be exceptionally difficult (Scherer et al. [2015]). Thus, this study designed and assessed a personalized source spaced non-invasive BCI pipeline which can be of great value for patients who have limited communication.

6.2 Future Directions

Future work may firstly focus on computationally tuning the proposed personalized BCI. In the presented pipeline, source reconstruction was performed for all source points and ROIs were covering the whole brain surface and/or brain volume since various examined tasks employed various brain regions and limiting the ROIs was not appropriate. However, after identifying the best separable commands, only the most relevant ROIs could be beamformed and feature calculation can be optimized to be less computationally demanding and ultimately enhance the real-time pace. Additionally, as recommended in literature, individual MRI scans can be used to obtain a more precise subject-specific head model and lead field which might improve the performance of the BCI as a result of more accurate source reconstruction. Also, to confirm the efficacy of the task combinations, conducting real-time experiments is a high priority for future research.

Furthermore, the analyzed mental tasks were recorded in experimental conditions where not only were the volunteers instructed to focus on the tasks and avoid mind wandering, but also the study paradigm and performing mental imagery was a new

experience for them. These factors lead to maximal concentration while in a real-world setting, this is not necessarily going to be the case. By repetition and getting accustomed to the mental commands over time, the user might not engage fully while performing the command. In addition to that, considering the changes of brain networks over time due to neuroplasticity, it should be investigated if over time, the selected pair of tasks sustain the same level of distinction. To maintain the performance of the BCI, reassessing the array of commands and changing the control signals to engage back the attention of the user might be required: a dynamic personalized BCI.

Finally, since the actual target group of users are disabled individuals, it is of utmost importance that the proposed framework is evaluated on a population of patients with various impairments. Depending on the specific impairment, disabled individuals are expected to show differences in their task classification. This could confirm whether using mental commands incorporating the patient's healthy brain regions could offer a superior means of communication. However, this study was an important step toward demonstrating that there are promising alternatives to motor imagery identifiable in source space, which might be especially beneficial for severely motor impaired individuals.

Bibliography

Reza Abiri, Soheil Borhani, Eric W Sellers, Yang Jiang, and Xiaopeng Zhao. A comprehensive review of eeg-based brain–computer interface paradigms. *Journal of neural engineering*, 16(1):011001, 2019.

Minkyu Ahn, Jun Hee Hong, and Sung Chan Jun. Source space based brain computer interface. In *17th International Conference on Biomagnetism Advances in Biomagnetism–Biomag2010*, pages 366–369. Springer, 2010.

Zeynep Akalin-Acar and Nevzat G Gençer. An advanced boundary element method (bem) implementation for the forward problem of electromagnetic source imaging. *Physics in medicine & biology*, 49(21):5011, 2004.

Philip J Allen, Oliver Josephs, and Robert Turner. A method for removing imaging artifact from continuous eeg recorded during functional mri. *Neuroimage*, 12(2):230–239, 2000.

Brendan Z Allison and Christa Neuper. Could anyone use a bci? In *Brain-computer interfaces*, pages 35–54. Springer, 2010.

Kai Keng Ang, Zheng Yang Chin, Chuanchu Wang, Cuntai Guan, and Haihong

- Zhang. Filter bank common spatial pattern algorithm on bci competition iv datasets 2a and 2b. *Frontiers in neuroscience*, 6:39, 2012.
- Laura Astolfi, Febo Cincotti, Donatella Mattia, M Grazia Marciani, Luiz A Baccala, Fabrizio de Vico Fallani, Serenella Salinari, Mauro Ursino, Melissa Zavaglia, Lei Ding, et al. Comparison of different cortical connectivity estimators for high-resolution eeg recordings. *Human brain mapping*, 28(2):143–157, 2007.
- Fahim Gohar Awan, Omer Saleem, and Asima Kiran. Recent trends and advances in solving the inverse problem for eeg source localization. *Inverse Problems in Science and Engineering*, 27(11):1521–1536, 2019.
- Sylvain Baillet, John C Mosher, and Richard M Leahy. Electromagnetic brain mapping. *IEEE Signal processing magazine*, 18(6):14–30, 2001.
- Tonio Ball, Axel Schreiber, Bernd Feige, Michael Wagner, Carl Hermann Lücking, and Rumyana Kristeva-Feige. The role of higher-order motor areas in voluntary movement as revealed by high-resolution eeg and fmri. *Neuroimage*, 10(6):682–694, 1999.
- Dipali Bansal and Rashima Mahajan. *EEG-Based Brain-Computer Interfaces: Cognitive Analysis and Control Applications*. Academic Press, 2019.
- Michel Besserve, Jacques Martinerie, and Line Garnero. Improving quantification of functional networks with eeg inverse problem: Evidence from a decoding point of view. *NeuroImage*, 55(4):1536–1547, 2011.
- Benjamin Blankertz, Guido Dornhege, Matthias Krauledat, Klaus-Robert Müller, and

- Gabriel Curio. The non-invasive berlin brain–computer interface: fast acquisition of effective performance in untrained subjects. *NeuroImage*, 37(2):539–550, 2007a.
- Benjamin Blankertz, Ryota Tomioka, Steven Lemm, Motoaki Kawanabe, and Klaus-Robert Müller. Optimizing spatial filters for robust eeg single-trial analysis. *IEEE Signal processing magazine*, 25(1):41–56, 2007b.
- Benjamin Blankertz, Claudia Sanelli, Sebastian Halder, E Hammer, Andrea Kübler, Klaus-Robert Müller, Gabriel Curio, and Thorsten Dickhaus. Predicting bci performance to study bci illiteracy. *BMC Neurosci*, 10(Suppl 1):P84, 2009.
- Bernhard E Boser, Isabelle M Guyon, and Vladimir N Vapnik. A training algorithm for optimal margin classifiers. In *Proceedings of the fifth annual workshop on Computational learning theory*, pages 144–152, 1992.
- Brain Products, GmbH, Germany. BrainVision Analyzer, (Version 2.2.0) [Software]. (2019).
- Matthew Brett, Kalina Christoff, Rhodri Cusack, Jack Lancaster, et al. Using the talairach atlas with the mni template. *Neuroimage*, 13(6):85–85, 2001.
- Katharine Brigham and BVK Vijaya Kumar. Imagined speech classification with eeg signals for silent communication: a preliminary investigation into synthetic telepathy. In *2010 4th International Conference on Bioinformatics and Biomedical Engineering*, pages 1–4. IEEE, 2010.
- Korbinian Brodmann. *Vergleichende Lokalisationslehre der Grosshirnrinde in ihren Prinzipien dargestellt auf Grund des Zellenbaues*. Barth, 1909.

Denis Brunet, Micah M Murray, and Christoph M Michel. Spatiotemporal analysis of multichannel eeg: Cartool. *Computational intelligence and neuroscience*, 2011, 2011.

Jie Cai, Jiawei Luo, Shulin Wang, and Sheng Yang. Feature selection in machine learning: A new perspective. *Neurocomputing*, 300:70–79, 2018.

Jose M Carmena, Mikhail A Lebedev, Roy E Crist, Joseph E O’Doherty, David M Santucci, Dragan F Dimitrov, Parag G Patil, Craig S Henriquez, and Miguel AL Nicolelis. Learning to control a brain–machine interface for reaching and grasping by primates. *PLoS biol*, 1(2):e42, 2003.

Rifai Chai, Sai Ho Ling, Gregory P Hunter, and Hung T Nguyen. Mental non-motor imagery tasks classifications of brain computer interface for wheelchair commands using genetic algorithm-based neural network. In *The 2012 International Joint Conference on Neural Networks (IJCNN)*, pages 1–7. IEEE, 2012.

Ricardo Chavarriaga, Aleksander Sobolewski, and José del R Millán. Errare machinale est: the use of error-related potentials in brain-machine interfaces. *Frontiers in neuroscience*, 8:208, 2014.

Guijun Chen, Xueying Zhang, Ying Sun, and Jing Zhang. Emotion feature analysis and recognition based on reconstructed eeg sources. *IEEE Access*, 8:11907–11916, 2020.

Philip Chrapka. *Advances in EP and ERP signal processing*. PhD thesis, 2018.

Mike X Cohen. *Analyzing neural time series data: theory and practice*. MIT press, 2014.

Ana Coito, Gijs Plomp, Mélanie Genetti, Eugenio Abela, Roland Wiest, Margitta Seeck, Christoph M Michel, and Serge Vulliemoz. Dynamic directed interictal connectivity in left and right temporal lobe epilepsy. *Epilepsia*, 56(2):207–217, 2015.

Anders M Dale and Eric Halgren. Spatiotemporal mapping of brain activity by integration of multiple imaging modalities. *Current opinion in neurobiology*, 11(2):202–208, 2001.

Anders M Dale and Martin I Sereno. Improved localizadon of cortical activity by combining eeg and meg with mri cortical surface reconstruction: a linear approach. *Journal of cognitive neuroscience*, 5(2):162–176, 1993.

Anders M Dale, Arthur K Liu, Bruce R Fischl, Randy L Buckner, John W Belliveau, Jeffrey D Lewine, and Eric Halgren. Dynamic statistical parametric mapping: combining fmri and meg for high-resolution imaging of cortical activity. *neuron*, 26(1):55–67, 2000.

Charles S DaSalla, Hiroyuki Kambara, Makoto Sato, and Yasuharu Koike. Single-trial classification of vowel speech imagery using common spatial patterns. *Neural networks*, 22(9):1334–1339, 2009.

Anna Devor, Andrew K Dunn, Mark L Andermann, Istvan Ulbert, David A Boas, and Anders M Dale. Coupling of total hemoglobin concentration, oxygenation, and neural activity in rat somatosensory cortex. *Neuron*, 39(2):353–359, 2003.

Jaskiret Dhindsa. *Generalized Methods for User-Centered Brain-Computer Interfacing*. PhD thesis, 2017.

Kiret Dhindsa, Dean Carcone, and Suzanna Becker. An open-ended approach to bci: Embracing individual differences by allowing for user-defined mental commands. *Frontiers Comput. Neurosci.*, 9, 2015.

Stavros I Dimitriadis, María E López, Ricardo Bruña, Pablo Cuesta, Alberto Marcos, Fernando Maestú, and Ernesto Pereda. How to build a functional connectomic biomarker for mild cognitive impairment from source reconstructed meg resting-state activity: the combination of roi representation and connectivity estimator matters. *Frontiers in neuroscience*, 12:306, 2018.

Esmeralda C Djamal, Maulana Y Abdullah, and Faiza Renaldi. Brain computer interface game controlling using fast fourier transform and learning vector quantization. *Journal of Telecommunication, Electronic and Computer Engineering (JTEC)*, 9 (2-5):71–74, 2017.

Bradley J Edelman, Bryan Baxter, and Bin He. Eeg source imaging enhances the decoding of complex right-hand motor imagery tasks. *IEEE Transactions on Biomedical Engineering*, 63(1):4–14, 2015.

Bradley J Edelman, Bryan Baxter, and Bin He. Eeg source imaging enhances the decoding of complex right-hand motor imagery tasks. *IEEE Transactions on Biomedical Engineering*, 63(1):4–14, 2016.

Jerome Friedman, Trevor Hastie, Robert Tibshirani, et al. *The elements of statistical learning*, volume 1. Springer series in statistics New York, 2001.

Elisabeth VC Friedrich, Reinhold Scherer, and Christa Neuper. The effect of distinct mental strategies on classification performance for brain–computer interfaces. *International Journal of Psychophysiology*, 84(1):86–94, 2012.

Irina F Gorodnitsky, John S George, and Bhaskar D Rao. Neuromagnetic source imaging with focuss: a recursive weighted minimum norm algorithm. *Electroencephalography and clinical Neurophysiology*, 95(4):231–251, 1995.

Roberta Grech, Tracey Cassar, Joseph Muscat, Kenneth P Camilleri, Simon G Fabri, Michalis Zervakis, Petros Xanthopoulos, Vangelis Sakkalis, and Bart Vanrumste. Review on solving the inverse problem in eeg source analysis. *Journal of neuro-engineering and rehabilitation*, 5(1):1–33, 2008.

Moritz Grosse-Wentrup and Martin Buss. Multiclass common spatial patterns and information theoretic feature extraction. *IEEE transactions on Biomedical Engineering*, 55(8):1991–2000, 2008.

Moritz Grosse-Wentrup, Christian Liefhold, Klaus Gramann, and Martin Buss. Beamforming in noninvasive brain–computer interfaces. *IEEE Transactions on Biomedical Engineering*, 56(4):1209–1219, 2009.

Matti S Hämäläinen and Risto J Ilmoniemi. Interpreting magnetic fields of the brain: minimum norm estimates. *Medical & biological engineering & computing*, 32(1):35–42, 1994.

Sofie Therese Hansen, Apit Hemakom, Mads Gylling Safeldt, Lærke Karen Krohne, Kristoffer Hougaard Madsen, Hartwig R Siebner, Danilo P Mandic, and Lars Kai

- Hansen. Unmixing oscillatory brain activity by eeg source localization and empirical mode decomposition. *Computational intelligence and neuroscience*, 2019, 2019.
- Amabilis H Harrison. *Mental Imagery for the Detection of Awareness: Evaluating the Convergence of Functional Magnetic Resonance Imaging and Electroencephalographic Assessments*. PhD thesis, 2014.
- Amabilis H Harrison, Michael D Noseworthy, James P Reilly, Weiguang Guan, and John F Connolly. Eeg and fmri agree: Mental arithmetic is the easiest form of imagery to detect. *Consciousness and cognition*, 48:104–116, 2017.
- Mahmoud Hassan and Fabrice Wendling. Electroencephalography source connectivity: aiming for high resolution of brain networks in time and space. *IEEE Signal Processing Magazine*, 35(3):81–96, 2018.
- Mahmoud Hassan, Isabelle Merlet, Ahmad Mheich, Aya Kabbara, Arnaud Biraben, Anca Nica, and Fabrice Wendling. Identification of interictal epileptic networks from dense-eeg. *Brain topography*, 30(1):60–76, 2017.
- About Ella Hassanien and AA Azar. Brain-computer interfaces. *Switzerland: Springer*, 2015.
- Lukas Hecker, Rebekka Rupprecht, Ludger Tebartz van Elst, and Juergen Kornmeier. Convdip: A convolutional neural network for better eeg source imaging. *Frontiers in Neuroscience*, 15:533, 2021.
- Colin J Holmes, Rick Hoge, Louis Collins, Roger Woods, Arthur W Toga, and Alan C Evans. Enhancement of mr images using registration for signal averaging. *Journal of computer assisted tomography*, 22(2):324–333, 1998.

Li Hu and Zhiguo Zhang. *EEG signal processing and feature extraction*. Springer, 2019.

Yu Huang, Lucas C Parra, and Stefan Haufe. The new york head—a precise standardized volume conductor model for eeg source localization and tes targeting. *NeuroImage*, 140:150–162, 2016.

René J Huster, Stefan Debener, Tom Eichele, and Christoph S Herrmann. Methods for simultaneous eeg-fmri: an introductory review. *Journal of Neuroscience*, 32(18):6053–6060, 2012.

Han-Jeong Hwang, Soyoun Kim, Soobeom Choi, and Chang-Hwan Im. Eeg-based brain-computer interfaces: a thorough literature survey. *International Journal of Human-Computer Interaction*, 29(12):814–826, 2013.

Iñaki Iturrate, Ricardo Chavarriaga, and José del R Millán. General principles of machine learning for brain-computer interfacing. *Handbook of clinical neurology*, 168:311–328, 2020.

Sunao Iwaki and Shoogo Ueno. Weighted minimum-norm source estimation of magnetoencephalography utilizing the temporal information of the measured data. *Journal of Applied physics*, 83(11):6441–6443, 1998.

Munsif Ali Jatoi and Nidal Kamel. *Brain source localization using EEG signal analysis*. CRC Press, 2017.

Baharan Kamousi, Ali Nasiri Amini, and Bin He. Classification of motor imagery by means of cortical current density estimation and von neumann entropy. *Journal of Neural Engineering*, 4(2):17, 2007.

Zoltan J Koles and Anthony CK Soong. Eeg source localization: implementing the spatio-temporal decomposition approach. *Electroencephalography and clinical Neurophysiology*, 107(5):343–352, 1998.

Zoltan Joseph Koles. The quantitative extraction and topographic mapping of the abnormal components in the clinical eeg. *Electroencephalography and clinical Neurophysiology*, 79(6):440–447, 1991.

Gautam Krishna, Yan Han, Co Tran, Mason Carnahan, and Ahmed H Tewfik. State-of-the-art speech recognition using eeg and towards decoding of speech spectrum from eeg. *arXiv preprint arXiv:1908.05743*, 2019.

Ming-Ai Li, Yi-Fan Wang, Song-Min Jia, Yan-Jun Sun, and Jin-Fu Yang. Decoding of motor imagery eeg based on brain source estimation. *Neurocomputing*, 339:182–193, 2019.

Jussi T Lindgren. As above, so below? towards understanding inverse models in bci. *Journal of neural engineering*, 15(1):012001, 2017.

Fabien Lotte, Laurent Bougrain, and Maureen Clerc. Electroencephalography (eeg)-based brain–computer interfaces. *Wiley Encyclopedia of Electrical and Electronics Engineering*, pages 1–20, 2015.

Keyvan Mahjoory, Vadim V Nikulin, Loïc Botrel, Klaus Linkenkaer-Hansen, Marco M Fato, and Stefan Haufe. Consistency of eeg source localization and connectivity estimates. *Neuroimage*, 152:590–601, 2017.

Joseph A Maldjian, Paul J Laurienti, Robert A Kraft, and Jonathan H Burdette. An

- automated method for neuroanatomic and cytoarchitectonic atlas-based interrogation of fmri data sets. *Neuroimage*, 19(3):1233–1239, 2003.
- John Mazziotta, Arthur Toga, Alan Evans, Peter Fox, Jack Lancaster, Karl Zilles, Roger Woods, Tomas Paus, Gregory Simpson, Bruce Pike, et al. A probabilistic atlas and reference system for the human brain: International consortium for brain mapping (icbm). *Philosophical Transactions of the Royal Society of London. Series B: Biological Sciences*, 356(1412):1293–1322, 2001.
- Christoph M Michel and Denis Brunet. Eeg source imaging: a practical review of the analysis steps. *Frontiers in neurology*, 10:325, 2019.
- Christoph M. Michel and Bin He. EEG source localization. In *Handbook of Clinical Neurology*, volume 160, pages 85–101. Elsevier, 2019. ISBN 9780444640321.
- Christoph M Michel, Micah M Murray, Göran Lantz, Sara Gonzalez, Laurent Spinelli, and Rolando Grave de Peralta. Eeg source imaging. *Clinical neurophysiology*, 115(10):2195–2222, 2004.
- Martin M Monti, Audrey Vanhaudenhuyse, Martin R Coleman, Melanie Boly, John D Pickard, Luaba Tshibanda, Adrian M Owen, and Steven Laureys. Willful modulation of brain activity in disorders of consciousness. *New England journal of medicine*, 362(7):579–589, 2010.
- John C Mosher, Paul S Lewis, and Richard M Leahy. Multiple dipole modeling and localization from spatio-temporal meg data. *IEEE transactions on biomedical engineering*, 39(6):541–557, 1992.

John C Mosher, Richard M Leahy, and Paul S Lewis. Eeg and meg: forward solutions for inverse methods. *IEEE Transactions on Biomedical Engineering*, 46(3):245–259, 1999.

Shingo Murakami and Yoshio Okada. Contributions of principal neocortical neurons to magnetoencephalography and electroencephalography signals. *The Journal of Physiology*, 575(3):925–936, 2006. doi: 10.1113/jphysiol.2006.105379.

Muthuraman Muthuraman, Helge Hellriegel, Nienke Hoogenboom, Abdul Rauf Anwar, Kidist Gebremariam Mideksa, Holger Krause, Alfons Schnitzler, Günther Deuschl, and Jan Raethjen. Beamformer source analysis and connectivity on concurrent eeg and meg data during voluntary movements. *PloS one*, 9(3):e91441, 2014.

Violetta Nedelko, Thomas Hassa, Farsin Hamzei, Cornelius Weiller, Ferdinand Binkofski, Mircea Ariel Schoenfeld, Oliver Tüscher, and Christian Dettmers. Age-independent activation in areas of the mirror neuron system during action observation and action imagery. a fmri study. *Restorative neurology and neuroscience*, 28(6):737–747, 2010.

Chuong H Nguyen, George K Karavas, and Panagiotis Artemiadis. Inferring imagined speech using eeg signals: a new approach using riemannian manifold features. *Journal of neural engineering*, 15(1):016002, 2017.

Rami K Niazy, Christian F Beckmann, Gian Domenico Iannetti, J Michael Brady, and Stephen M Smith. Removal of fmri environment artifacts from eeg data using optimal basis sets. *Neuroimage*, 28(3):720–737, 2005.

Paul L Nunez, Ramesh Srinivasan, Andrew F Westdorp, Ranjith S Wijesinghe, Don M Tucker, Richard B Silberstein, and Peter J Cadusch. Eeg coherency: I: statistics, reference electrode, volume conduction, laplacians, cortical imaging, and interpretation at multiple scales. *Electroencephalography and clinical neurophysiology*, 103(5):499–515, 1997.

Paul L Nunez, Ramesh Srinivasan, et al. *Electric fields of the brain: the neurophysics of EEG*. Oxford University Press, USA, 2006.

Robert Oostenveld and Peter Praamstra. The five percent electrode system for high-resolution eeg and erp measurements. *Clinical neurophysiology*, 112(4):713–719, 2001.

Jerrin Thomas Panachakel and Angarai Ganesan Ramakrishnan. Decoding covert speech from eeg—a comprehensive review. *Frontiers in Neuroscience*, 15:392, 2021.

Jerrin Thomas Panachakel, AG Ramakrishnan, and TV Ananthapadmanabha. A novel deep learning architecture for decoding imagined speech from eeg. *arXiv preprint arXiv:2003.09374*, 2020.

Chethan Pandarinath, Paul Nuyujukian, Christine H Blabe, Brittany L Sorice, Jad Saab, Francis R Willett, Leigh R Hochberg, Krishna V Shenoy, and Jaimie M Henderson. High performance communication by people with paralysis using an intracortical brain-computer interface. *Elife*, 6:e18554, 2017.

Roberto D Pascual-Marqui, Christoph M Michel, and Dietrich Lehmann. Low resolution electromagnetic tomography: a new method for localizing electrical activity in the brain. *International Journal of psychophysiology*, 18(1):49–65, 1994.

Roberto D Pascual-Marqui, Michaela Esslen, Kieko Kochi, Dietrich Lehmann, et al. Functional imaging with low-resolution brain electromagnetic tomography (loreta): a review. *Methods and findings in experimental and clinical pharmacology*, 24(Suppl C):91–95, 2002a.

Roberto Domingo Pascual-Marqui et al. Standardized low-resolution brain electromagnetic tomography (sloreta): technical details. *Methods Find Exp Clin Pharmacol*, 24(Suppl D):5–12, 2002b.

Hanchuan Peng, Fuhui Long, and Chris Ding. Feature selection based on mutual information criteria of max-dependency, max-relevance, and min-redundancy. *IEEE Transactions on pattern analysis and machine intelligence*, 27(8):1226–1238, 2005.

Rolando Grave Peralta Menendez, Micah M Murray, Christoph M Michel, Roberto Martuzzi, and Sara L Gonzalez Andino. Electrical neuroimaging based on biophysical constraints. *Neuroimage*, 21(2):527–539, 2004.

Cyril Pernet, Marta Garrido, Alexandre Gramfort, Natasha Maurits, Christoph Michel, Elizabeth Pang, Riitta Salmelin, Jan Mathijs Schoffelen, Pedro A Valdes-Sosa, and Aina Puce. Best practices in data analysis and sharing in neuroimaging using meeg. 2018.

John Polich. Normal variation of p300 from auditory stimuli. *Electroencephalography and Clinical Neurophysiology/Evoked Potentials Section*, 65(3):236–240, 1986.

Lei Qin, Lei Ding, and Bin He. Motor imagery classification by means of source analysis for brain–computer interface applications. *Journal of neural engineering*, 1(3):135, 2004.

Mamunur Rashid, Norizam Sulaiman, Anwar PP Abdul Majeed, Rabiul Muazu Musa, Ahmad Fakhri Ab Nasir, Bifta Sama Bari, and Sabira Khatun. Current status, challenges, and possible solutions of eeg-based brain-computer interface: A comprehensive review. *Frontiers in neurorobotics*, 14, 2020.

Claude Robert, Jean-François Gaudy, and Aimé Limoge. Electroencephalogram processing using neural networks. *Clinical Neurophysiology*, 113(5):694–701, 2002.

Maria Rubega, Margherita Carboni, Martin Seeber, D Pascucci, S Tourbier, Giacomo Toscano, Pieter Van Mierlo, P Haggmann, G Plomp, Serge Vulliemoz, et al. Estimating eeg source dipole orientation based on singular-value decomposition for connectivity analysis. *Brain topography*, 32(4):704–719, 2019.

Maria V Ruiz-Blondet, Zhanpeng Jin, and Sarah Laszlo. Cerebre: A novel method for very high accuracy event-related potential biometric identification. *IEEE Transactions on Information Forensics and Security*, 11(7):1618–1629, 2016.

Maria V Ruiz Ruiz-Blondet, Sarah Laszlo, and Zhanpeng Jin. Assessment of permanence of non-volitional eeg brainwaves as a biometric. In *IEEE International Conference on Identity, Security and Behavior Analysis (ISBA 2015)*, pages 1–6. IEEE, 2015.

Simanto Saha, Khondaker A Mamun, Khawza Ahmed, Raqibul Mostafa, Ganesh R Naik, Ahsan Khandoker, Sam Darvishi, and Mathias Baumert. Progress in brain computer interfaces: challenges and trends. *arXiv preprint arXiv:1901.03442*, 2019.

Simanto Saha, Khondaker A Mamun, Khawza Iftexhar Uddin Ahmed, Raqibul Mostafa, Ganesh R Naik, Sam Darvishi, Ahsan H Khandoker, and Mathias

- Baumert. Progress in brain computer interface: Challenges and potentials. *Frontiers in Systems Neuroscience*, 15:4, 2021.
- Vangelis Sakkalis. Review of advanced techniques for the estimation of brain connectivity measured with eeg/meg. *Computers in biology and medicine*, 41(12): 1110–1117, 2011.
- Reinhold Scherer, Josef Faller, Elisabeth VC Friedrich, Eloy Opisso, Ursula Costa, Andrea Kübler, and Gernot R Müller-Putz. Individually adapted imagery improves brain-computer interface performance in end-users with disability. *PLoS one*, 10(5): e0123727, 2015.
- Michael Scherg, Thomas Bast, and Patrick Berg. Multiple source analysis of interictal spikes: goals, requirements, and clinical value. *Journal of Clinical Neurophysiology*, 16(3):214–224, 1999.
- Anett Seeland, Mario M Krell, Sirko Straube, and Elsa A Kirchner. Empirical comparison of distributed source localization methods for single-trial detection of movement preparation. *Frontiers in human neuroscience*, 12:340, 2018.
- Kensuke Sekihara and Srikatan S Nagarajan. *Adaptive spatial filters for electromagnetic brain imaging*. Springer Science & Business Media, 2008.
- Alborz Rezazadeh Sereshkeh, Robert Trott, Aurélien Bricout, and Tom Chau. Eeg classification of covert speech using regularized neural networks. *IEEE/ACM Transactions on Audio, Speech, and Language Processing*, 25(12):2292–2300, 2017.
- Leah Sinai, Adrian M Owen, and Lorina Naci. Mapping preserved real-world cognition in severely brain-injured patients. *Front Biosci (Landmark Ed)*, 22:815–823, 2017.

- Abbas Sohrabpour, Zhengxiang Cai, Shuai Ye, Benjamin Brinkmann, Gregory Worrell, and Bin He. Noninvasive electromagnetic source imaging of spatiotemporally distributed epileptogenic brain sources. *Nature communications*, 11(1):1–15, 2020.
- Dimitri P Solomatine and Avi Ostfeld. Data-driven modelling: some past experiences and new approaches. *Journal of hydroinformatics*, 10(1):3–22, 2008.
- Cornelis J Stam, Guido Nolte, and Andreas Daffertshofer. Phase lag index: assessment of functional connectivity from multi channel eeg and meg with diminished bias from common sources. *Human brain mapping*, 28(11):1178–1193, 2007.
- Gufei Sun, Jinglu Hu, and Gengfeng Wu. A novel frequency band selection method for common spatial pattern in motor imagery based brain computer interface. In *The 2010 International Joint Conference on Neural Networks (IJCNN)*, pages 1–6. IEEE, 2010.
- Nathalie Tzourio-Mazoyer, Brigitte Landeau, Dimitri Papathanassiou, Fabrice Crivello, Olivier Etard, Nicolas Delcroix, Bernard Mazoyer, and Marc Joliot. Automated anatomical labeling of activations in spm using a macroscopic anatomical parcellation of the mni mri single-subject brain. *Neuroimage*, 15(1):273–289, 2002.
- G Van Hoey, R Van de Walle, Bart Vanrumste, M D’Havse, I Lemahieu, and P Boon. Beamforming techniques applied in eeg source analysis. *Proc. ProRISC99*, 10:545–549, 1999.
- Barry D Van Veen and Kevin M Buckley. Beamforming: A versatile approach to spatial filtering. *IEEE assp magazine*, 5(2):4–24, 1988.

- Barry D Van Veen, Wim Van Drongelen, Moshe Yuchtman, and Akifumi Suzuki. Localization of brain electrical activity via linearly constrained minimum variance spatial filtering. *IEEE Transactions on biomedical engineering*, 44(9):867–880, 1997.
- Mariska J Vansteensel and Beata Jarosiewicz. Brain-computer interfaces for communication. In *Handbook of clinical neurology*, volume 168, pages 67–85. Elsevier, 2020.
- Carmen Vidaurre and Benjamin Blankertz. Towards a cure for bci illiteracy. *Brain topography*, 23(2):194–198, 2010.
- Peter Welch. The use of fast fourier transform for the estimation of power spectra: a method based on time averaging over short, modified periodograms. *IEEE Transactions on audio and electroacoustics*, 15(2):70–73, 1967.
- Andreas Widmann and Erich Schröger. Filter effects and filter artifacts in the analysis of electrophysiological data. *Frontiers in psychology*, 3:233, 2012.
- Jonathan R Wolpaw, José del R Millán, and Nick F Ramsey. Brain-computer interfaces: Definitions and principles. In *Handbook of clinical neurology*, volume 168, pages 15–23. Elsevier, 2020.
- Carsten Hermann Wolters, H Köstler, C Möller, J Härdtlein, and A Anwander. Numerical approaches for dipole modeling in finite element method based source analysis. In *International Congress Series*, volume 1300, pages 189–192. Elsevier, 2007.
- Ioannis Xygonakis, Alkinoos Athanasiou, Niki Pandria, Dimitris Kugiumtzis, and Panagiotis D Bamidis. Decoding motor imagery through common spatial pattern

filters at the eeg source space. *Computational intelligence and neuroscience*, 2018, 2018.

Aleksandr Zaitcev, Wei Liu, Greg Cook, Martyn Paley, and Elizabeth Milne. Source analysis in motor imagery eeg bci applications. 2019.

Haihong Zhang, Cuntai Guan, Kai Keng Ang, and Zheng Yang Chin. Bci competition iv–data set i: learning discriminative patterns for self-paced eeg-based motor imagery detection. *Frontiers in neuroscience*, 6:7, 2012.